Two-Phase Flow and Heat Transfer in Reflux Thermosyphons

KATE SMITH

Supervised by Prof. Anthony Robinson & Dr. Roger Kempers

Department of Mechanical & Manufacturing Engineering
University of Dublin, Trinity College

April 2016

A thesis submitted to the University of Dublin in partial
fulfilment of the requirements of the degree of
Doctor in Philosophy

Declaration

I, Kate Smith, have read and I understand the plagiarism provisions in the General Regulations of the University Calendar for the current year, found at http://www.tcd.ie/calendar.

I have also completed the Online Tutorial on avoiding plagiarism, 'Ready Steady Write', located at http://tcd-ie.libguides.com/plagiarism/ready-steady-write.

I declare that this thesis has not been submitted as an exercise for a degree at this or any other university and it is entirely my own work.

I agree to deposit this thesis in the University's open access institutional repository or allow the library to do so on my behalf, subject to Irish Copyright Legislation and Trinity College Library conditions of use and acknowledgement.

Kate Smith, April 2016

Summary

Improved cooling technologies are becoming necessary in electronic applications, specifically Radio Frequency Power Amplifiers (RFPA) installed in tower-top Remote Radioheads (RRH). Current methods of cooling are becoming inadequate as heightened service demands increase heat generation. The hardware is also subject to thermal cycling which can impact long-term reliability and function.

With this in mind, the objectives of this study involve the design and characterisation of a small dimension thermosyphon suitable for use as an RFPA cooling solution and, ultimately, thermal management system.

The performance of small-scale (D_i ~ 10 mm) thermosyphons was determined in terms of both the rate of heat transfer and the fluid dynamics. The counter-current flow of the liquid and vapour phases in small-scale thermosyphons resulted in substantial interfacial forces that can lead to rapid deterioration of the rate of heat transfer. With small dimensions there is an additional restriction on the flow due to confinement of the vapour during evaporation, which can significantly affect the two-phase flow regimes.

An initial feasibility study was performed to assess the capability of a two-phase thermosyphon in this particular application, using water as the working fluid. To mimic the operating conditions within the RRH, the condenser section of the thermosyphon was cooled by natural convection to ambient conditions. High watt density ceramic heaters were used as the heat source to replicate both the size and power output of the RFPA. The investigation of thermosyphon performance involved varying the fill volume of working fluid and installing various bend angles in the thermosyphon geometry.

It was found that the thermosyphon could provide adequate cooling for the required application. The results highlighted the benefits of using bends in the thermosyphon geometry of a small-scale thermosyphon to reduce the liquid-vapour interfacial forces that can lead to deterioration of the heat transfer within the device. The vertical thermosyphon exhibited oscillatory, geyser boiling behaviour which deviated from the conventional boiling mechanisms described for thermosyphons: nucleate pool boiling and falling film condensation.

The oscillatory boiling behaviour of small dimension thermosyphons was investigated by designing and constructing a fully transparent thermosyphon. Synchronised flow visualisation via high-speed imaging and thermal measurements enabled an interlinked study of the flow regimes and heat transfer. Three working fluids were employed to assess the performance with varied thermophysical properties. The observed flow regimes could be characterised in terms of the degree of confinement and rate of vapour production. Flow pattern maps were developed which could guide future small dimension thermosyphon design to avoid the geyser boiling regime, a result of a combination of both high levels of confinement and vapour production. The rate of heat transfer associated with each flow regime highlighted the flow regimes that were most conducive to high rates of heat transfer, mainly churn flow.

Finally, an augmentation study of the flow regimes and heat transfer was carried out using electrohydrodynamics (EHD). This study outlined the potential opportunity for smart control of the heat transfer within thermosyphons. Both heat transfer enhancement and deterioration were observed, depending on the initial, free-field flow regime. The response of the system to EHD was also fast and reversible.

In conclusion, a deep understanding of the flow regimes and associated heat transfer has been gained through analysis of the dominant forces in two-phase flow in small diameter thermosyphons. A novel thermosyphon design with complex geometry was developed providing a viable cooling solution for electronic applications. Further to this, a transparent test section was developed to characterise flow regimes and heat transfer in small dimension thermosyphons with the additional capability of EHD flow augmentation. This study highlighted the possibility of advanced thermosyphon cooling technologies with the prospect of high thermal performance and intelligent operation.

Acknowledgements

Firstly, I would like to thank my supervisors, Prof. Anthony Robinson and Dr. Roger Kempers, who had endless enthusiasm for this research. Their guidance and support was always on hand and I thoroughly enjoyed learning from them over the last four years.

A special thank you to Gerry Byrne in the thermo lab for his support, friendship and an unending supply of glue that helped me hold everything together throughout this project.

I would also like to thank the technical and workshop staff in the department, especially Mick Reilly, Gordon O'Brien, and JJ Ryan, for their help with the design and construction of my experimental rig. Thank you for your patience in helping me with any issue, big or small.

Thanks to my fellow researchers and friends in the Parsons Building. The many teatime scones and lunchtime chats helped keep me sane over the last four years. Also, a special thank you to my friends for your help in catching all my mistakes, your careful reading is greatly appreciated!

I'd like to thank my parents and my sister, Joanne, for cheering me on to the finish line. They are a constant source of encouragement and support in everything I do and were always there to lend a helping hand, no matter the time or place.

To Dave, who believed I could do this even more than I did, thank you for staying by my side through everything.

Table of Contents

Table of Contents .... **i**

List of Figures .... **v**

List of Tables .... **ix**

Nomenclature .... **xi**

Publications .... **xv**

1. Introduction **1**
  1.1. Thesis outline 3

2. Literature review **5**
  2.1. Thermosyphon operation 5
  2.2. Thermosyphon heat transfer 8
    2.2.1. Condensation heat transfer 8
    2.2.2. Boiling behaviour in thermosyphons 10
  2.3. Limitations to heat transfer 13
    2.3.1. Effects of confinement on boiling in thermosyphons 14
  2.4. Summary 19

3. Feasibility study **21**
  3.1. Introduction 21
  3.2. Literature review 22
    3.2.1. Effect of inclination angle 22
    3.2.2. Effect of bend angle 22
    3.2.3. Effect of fill ratio 23
    3.2.4. Summary 24
  3.3. Experimental methodology 25
    3.3.1. Experimental apparatus 25
    3.3.2. Data reduction 27
  3.4. Results and discussion 29
    3.4.1. Behaviour of vertical thermosyphon under thermal loading conditions 29
    3.4.2. Effects of inclination angle and fluid loading 35
    3.4.3. Failure performance characteristics 43
    3.4.4. Outlook for passively cooling of electronics 48
  3.5. Conclusion 50

4. Flow regimes and heat transfer study ... 53
4.1. Introduction ... 53
4.2. Literature review ... 54
    4.2.1. Analysis of flow regimes – Influence of flow regimes on heat transfer ... 54
    4.2.2. Summary ... 57
4.3. Methodology ... 58
    4.3.1. Experimental design ... 58
    4.3.2. Instrumentation ... 61
    4.3.3. Working fluids ... 62
    4.3.4. Testing methodology ... 64
    4.3.5. Data reduction ... 65
    4.3.6. Uncertainty and error in analysis ... 66
4.4. Results and discussion – Flow regime analysis ... 69
    4.4.1. Working fluid study ... 76
        4.4.1.1. Water at low pressure and low heat flux ... 78
        4.4.1.2. Water at low pressure and high heat flux ... 83
        4.4.1.3. Water at high pressure and low heat flux ... 90
        4.4.1.4. Water at high pressure and high heat flux ... 94
        4.4.1.5. HFE-7000 at low pressure and low heat flux ... 95
        4.4.1.6. HFE-7000 at low pressure and high heat flux ... 99
        4.4.1.7. HFE-7000 at high pressure ... 100
        4.4.1.8. Ethanol at low pressure and low heat flux ... 101
        4.4.1.9. Ethanol at low pressure and high heat flux ... 109
        4.4.1.10. Ethanol at high pressure and low heat flux ... 112
        4.4.1.11. Ethanol at high pressure and high heat flux ... 114
    4.4.2. Flow maps ... 117
    4.4.3. Summary ... 119
4.5. Results and discussion – Heat transfer analysis ... 120
    4.5.1. Temperature distribution ... 120
    4.5.2. Heat transfer analysis ... 124
4.6. Conclusion ... 132

5. Flow augmentation using Electrohydrodynamics ... 135
5.1. Introduction ... 135
5.2. Literature review ... 137
    5.2.1. Electrohydrodynamic augmentation of flow boiling ... 137
    5.2.2. Electrohydrodynamics in heat pipe applications ... 138
    5.2.3. Summary ... 139

5.3. Methodology....140
    5.3.1. Experimental design....140
    5.3.2. Instrumentation....141
    5.3.3. Testing methodology....142
5.4. Results and discussion....143
5.5. Conclusion....151

6. Conclusion....153

7. Further Work....157

Bibliography....159

Appendix A. Biot number analysis....165

Appendix B. Heat loss analysis....167

Appendix C. Influence of electrode on confinement....169

List of Figures

Chapter 1

Figure 1.1 - Remote Radiohead box (for illustration purposes) 1

Figure 1.2 - Thermal imaging of heat spread from RFPA 2

Chapter 2

Figure 2.1 - Two-phase thermosyphon operation, adapted from [4] 5

Figure 2.2 - Surface tension, inertia and gravity dominated regions, source: [27] 10

Chapter 3

Figure 3.1 - Operation envelope of a thermosyphon, [38] 24

Figure 3.2 - Schematic of stainless steel thermosyphon with bends 26

Figure 3.3 - Temperatures and pressure at 40W in (a) the evaporator and (b) the condenser showing geyser boiling 30

Figure 3.4 - Temperature standard deviation of (a) evaporator wall and (b) evaporator vapour 30

Figure 3.5 - Evaporator wall temperature distributions for higher power range 31

Figure 3.6 - Wall and vapour temperature and pressure in (a) the evaporator and (b) the condenser at Q = 250 W 32

Figure 3.7 - Wall and vapour temperature and pressure in (a) the evaporator and (b) the condenser at Q = 300 W 33

Figure 3.8 - Wall and vapour temperature and pressure in (a) the evaporator and (b) the condenser at Q = 325 W 33

Figure 3.9 - Entrainment limit prediction using Faghri *et al*. correlation [37] 34

Figure 3.10 - (a) Total thermal resistance variation with bend angle and power (V_f = 15 mL) and (b) Variation of total thermal resistance with fluid loading (vertical orientation, 0°) 35

Figure 3.11 - (a) Evaporator thermal resistance and (b) condenser thermal resistance at various bend angles for V_f = 15 mL 37

Figure 3.12 - (a) Evaporator thermal resistance and (b) condenser thermal resistance at various fill ratios for 0° 41

Figure 3.13 - Thermal resistances per thermosyphon section for each angle over a range of power settings ($V_f = 15$ mL) 43

Figure 3.14 - Failure power levels for varying fill volume and bend angle; total thermal resistance at failure for varying fill volume and bend angle 44

Figure 3.15 - Flow of liquid condensate for each bend angle case at failure 45

Figure 3.16 - Evaporator wall temperature standard deviation with fill ratio (all bend angles) 47

Figure 3.17 - Thermal resistances across the entire system ($V_f = 15$ mL; 0° bend) 48

Chapter 4

Figure 4.1 - Flow regimes for boiling in vertical tubes, source: [59] 56

Figure 4.2 - (a) Schematic of apparatus; (b) Instrumentation of test section; (c) 3D rendering of thermosyphon; (d) Photographic image of thermosyphon 59

Figure 4.3 - Relative dominance of forces on two-phase flow in the current study 70

Figure 4.4 - Confinement and rate of vapour production of each fluid under investigation 74

Figure 4.5 - Water at low pressure and low heat flux (parameter values shown in figure) 78

Figure 4.6 - Water thermosyphon, $q = 7.5$ kW/m^2, $P_r = 0.0002$, $\Delta t = 0.06$ s 79

Figure 4.7 - Temperature and pressure trace for water at low pressure $P_r = 0.0002$, $q = 7.5$ kW/m^2 80

Figure 4.8 - Liquid jets following column collision. Water, $P_r = 0.0002$, $q = 7.5$ kW/m^2 83

Figure 4.9 - Evaporator temperature trace for water at high heat flux 19 kW/m^2 < q < 59 kW/m^2 84

Figure 4.10 - High-speed images for water, 19 kW/m^2 < q < 59 kW/m^2 85

Figure 4.11 - Water at low pressure and high heat flux 86

Figure 4.12 - Water, $P_r = 0.0002$, $q = 39$ kW/m^2, $\Delta t = 0.06$ s 87

Figure 4.13 - Temperature and pressure trace, water, $P_r = 0.0002$, $q = 39$ kW/m^2 88

Figure 4.14 - Entrainment of liquid upwards by vapour flow (water, $q = 58.7$ kW/m^2) 89

Figure 4.15 - Water at high pressure and low heat flux 91

Figure 4.16 - Water at high pressure, $P_r = 0.06$, $q = 5.5$ kW/m^2, $\Delta t = 0.06$ s 92

Figure 4.17 - Temperature and pressure trace, water at high pressure, $P_r = 0.06$, $q = 5.5$ kW/m^2 93

Figure 4.18 - Water at high pressure and high heat flux 94

Figure 4.19 - Temperature and pressure trace, and high-speed image, water, $P_r = 0.06$, $q = 17$ kW/m^2 95

Figure 4.20 - HFE-7000 at low pressure and low heat flux 96

Figure 4.21 - Temperature and pressure trace, HFE-7000, $P_r = 0.06$, $q = 7.8$ kW/m^2 97

Figure 4.22 - HFE-7000, $P_r = 0.06$, $q = 7.8$ kW/m^2, $\Delta t = 0.06$ s 98

Figure 4.23 - HFE-7000 at low pressure and high heat flux 99

Figure 4.24 - Temperature and pressure trace, and high-speed image showing film evaporation with nucleation, HFE-7000, $P_r = 0.02$, $q = 21$ kW/m^2 100

Figure 4.25 - HFE-7000 at high pressure, low heat flux (left) and high heat flux (right) 101

Figure 4.26 - Ethanol at low pressure and low heat flux 102

Figure 4.27 - Ethanol, $P_r = 0.001$, $q = 7$ kW/m^2 103

Figure 4.28 - Temperature and pressure trace, ethanol $P_r = 0.001$, $q = 7$ kW/m^2 104

Figure 4.29 - Upper: Temperature and pressure measurements, $q = 7$ kW/m^2 and 27 kW/m^2; Lower: FFT derived frequency of pressure measurement, ethanol, $P_r = 0.001$ 105

Figure 4.30 - Temperature traces for ethanol at high heat flux, $P_r = 0.001$ 107

Figure 4.31 - Ethanol, $P_r = 0.001$, $19 < q < 46.5$ kW/m^2 108

Figure 4.32 - Ethanol at low pressure and high heat flux 109

Figure 4.33 - Ethanol, $P_r = 0.001$, $q = 27$ kW/m^2, ...110

Figure 4.34 - Ethanol temperature and pressure trace, $P_r = 0.001$, $q = 27$ kW/m^2 111

Figure 4.35 - Ethanol at high pressure and low heat flux 112

Figure 4.36 - Ethanol, $P_r = 0.02$, $q = 5.6$ kW/m^2, $\Delta t = 0.06$ s 113

Figure 4.37 - Ethanol temperature and pressure trace, $P_r = 0.02$, $q = 5.6$ kW/m^2 114

Figure 4.38 - Ethanol at high pressure and high heat flux 114

Figure 4.39 - Temperature and pressure trace and high-speed image, ethanol, $P_r = 0.02$, $q = 17$ kW/m^2 115

Figure 4.40 - Flow pattern map for evaporator section, momentum flux coordinates 117

Figure 4.41 - Flow pattern map condenser section, momentum flux coordinates 118

Figure 4.42 - Temperature per section along thermosyphon length, low pressure condition 121

Figure 4.43 - Temperature flux for upper (T10) and lower (T8) thermocouple 122

Figure 4.44 - Evaporator heat transfer coefficient for each liquid compared to Imura correlation [31] 125

Figure 4.45 - Water evaporator flow map and measured heat transfer coefficient 126

Figure 4.46 - Ethanol evaporator flow map and measured heat transfer coefficient........ 127
Figure 4.47 - HFE-7000 evaporator flow map and measured heat transfer coefficient 128
Figure 4.48 - Condenser heat transfer coefficient and Nusselt correlation 129
Figure 4.49 - Condenser flow map and heat transfer coefficients of ethanol and water .. 130

Chapter 5

Figure 5.1 - Experimental set-up schematic, transparent thermosyphon showing representation of the high voltage connection 140
Figure 5.2 - Evaporator superheat with and without EHD (a) $q = 8$ kW/m^2 and (b) $q = 15$ kW/m^2 144
Figure 5.3 - Thermosyphon operation with no EHD forces, $q = 8$ kW/m^2 145
Figure 5.4 - Thermosyphon operation with no EHD forces, $q = 15$ kW/m^2 145
Figure 5.5 - Heat transfer coefficient trends for: (a) 50 % fill, low heat flux; (b) 100 % fill, low heat flux; (c) 50 % fill, high heat flux; (d) 100 % fill, high heat flux 146
Figure 5.6 - Evaporator superheat temperature time traces for low (left) and high (right) heat flux at $f = 100$ Hz 147
Figure 5.7 - EHD influence on flow. Top: $V = 0$ kV, $q = 8$ kW/m^2; Bottom: $V = 8$ kV, $q = 8$ kW/m^2 148
Figure 5.8 - EHD influence on flow. Top: $V = 0$ kV, $q = 15$ kW/m^2; Bottom: $V = 8$ kV, $q = 15$ kW/m^2 148
Figure 5.9 - Time trace for temperature and pressure with application and removal of EHD voltage ($q = 15$ kW/m^2, $V = 7.5$ kV, 100 % fill volume) 149

Appendix B

Figure B.1 - Thermal resistance network, evaporator to atmosphere 167

Appendix C

Figure C.1 - Evaporator heat transfer coefficients for low and high heat flux, 100 % and 50 % loading both with and without electrode 169
Figure C.2 - Representative images of the evaporator section for low and high heat flux, 50 % and 100 % loading both with and without electrode 170

List of Tables

Chapter 2

Table 2.1 - Summary of geyser boiling investigations [(*) denotes transparent test sections] 18

Chapter 3

Table 3.1 - Uncertainty in measured parameters 27

Table 3.2 - Propagation of error in R_{tot} with changing input power 28

Table 3.3 - Evaporator and condenser thermal resistance values 43

Chapter 4

Table 4.1 - Thermophysical properties of working fluids at atmospheric pressure (1.01 bar) 63

Table 4.2 - Test parameter matrix for transparent thermosyphon. 64

Table 4.3 - Uncertainty associated with experimental measurements 67

Table 4.4 - Overview of flow regimes for each fluid, reduced pressure, input power and dimensionless numbers, *Co*, *Bo*, *We* 72

Table 4.5 - Overview of evaporator wall temperature time trace for test conditions 73

Chapter 5

Table 5.1 - Test parameter matrix for transparent thermosyphon with EHD 142

Table 5.2 - Dimensionless relationships for increasing applied high voltage 143

Appendix A

Table A.1 - Experimental parameters used in Biot number analysis 165

Appendix B

Table B.1 - Experimental parameters for thermal resistance calculation 167

Nomenclature

Symbol	Description	Units
A	Surface area	m^2
Bi	Biot number	-
Bo	Bond number	-
Co	Confinement number	-
C_p	Specific heat	J/kgK
D	Diameter	m
E	Electric field strength	kV/m
f	Frequency	Hz
f_e	Electric force density	N/m^2
FFT	Fast Fourier Transform	-
FOM	Figure of Merit	-
Fr	Froude number	-
G	Mass flux	kg/m^2s
g	Gravitational acceleration	m/s^2
h	Heat transfer coefficient	W/Km^2
h_{fg}	Latent heat of vaporisation	J/kg
HV	High voltage	V
I	Current	A
j_v^*	Superficial vapour velocity or vapour production rate	-
K	Constant	-
k	Thermal conductivity	W/mK
L	Length	m
$\dot{m}$	Mass flow rate	kg/s
M_d	Masuda number	-
N_{lg}	Electrogravitational number	-
P	Pressure	bar
ΔP	Pressure difference	bar
p	Momentum flux	kg/ms^2
P_{crit}	Critical pressure	bar

Symbol	Description	Units
Pr	Prandtl number	-
P_r	Reduced pressure ($P_r = P/P_{crit}$)	-
Q	Power	W
q	Heat flux	W/m^2
R	Thermal resistance	K/W
R_0	Gas constant (water vapour)	J/kgK
r	Radius	m
Re	Reynolds number	-
RFPA	Radio Frequency Power Amplifier	-
RRH	Remote Radiohead	-
T	Temperature	°C
ΔT	Temperature difference	°C
t	Time	s
V	Voltage	V
V_f	Fill volume	mL or %
We	Weber number	-

Greek

Symbol	Description	Units
ε	Permittivity	N/V^2
ε_r	Relative permittivity or dielectric constant ($\varepsilon_r = \varepsilon/\varepsilon_0$)	-
ε_0	Permittivity of free space ($\varepsilon_0 = 8.85 \times 10^{-12}$)	N/V^2
θ	Angle	°
λ_c	Characteristic bubble length	m
μ	Dynamic viscosity	Ns/m^2
ν	Kinematic viscosity	m^2/s
ρ	Density	kg/m^3
ρ_{ei}	Charge density	C/m^3
σ	Surface tension	N/m

Subscripts

Symbol	Description	Units
0	Reference	
a	Adiabatic	
atm	Atmospheric	
c or cond	Condenser	
c-a	Condenser to ambient air	
conv	Convective	
e	Evaporator	
i	Inner	
l	Liquid	
max	Maximum	
NC	Natural convection	
o	Outer	
sat	Saturation	
SH	Superheat	
th	Thermal	
tot	Total	
ts	Thermosyphon	
v	Vapour	
w	Wall	
∞	Far field	

Publications

Peer reviewed conference papers

K. Smith, R. Kempers, A. Robinson, Boiling and condensation in small diameter closed two phase thermosyphons. 9th International Conference on Boiling and Condensation Heat Transfer. Boulder, Colorado. 2015.

K. Smith, R. Kempers, A. Robinson, S. Siedel, Flow visualisation in a transparent thermosyphon: Influence of internal pressure. Proceedings of the 15th International Heat Transfer Conference. Kyoto, Japan. 2014.

K. Smith, R. Kempers, S. Siedel, A. Robinson, Two Phase Flow in Small Diameter Thermosyphons. 52nd European Two Phase Flow Group Meeting. Dresden, Germany. 2014

K. Smith, S. Siedel, A. Robinson, R. Kempers, Visual study of fluid dynamics in wickless transparent heat pipes. 17th International Heat Pipe Conference. Kanpur, India. 2013.

K. Smith, S. Siedel, A. Robinson, R. Kempers, Investigation of thermosyphon performance with changing adiabatic section geometry. 17th International Heat Pipe Conference. Kanpur, India. 2013.

K. Smith, S. Siedel, L. Akalanne, R. Kempers, A. Robinson, Investigation of naturally aspirated thermosyphon for power amplifier cooling. 8th World Conference on Experimental Heat Transfer, Fluid Mechanics and Thermodynamics. Lisbon, Portugal. 2013.

1. Introduction

This research has been motivated by the need for a more effective cooling solution for electronic components used in telecommunications hardware, specifically Radio Frequency Power Amplifier (RFPA) transistors housed in Remote Radioheads (RRH), shown in Figure 1.1. Design of cooling equipment for this particular application is complicated by the fact that this hardware is positioned outdoors, usually on top of buildings or masts. Due to this, any RRH heat transfer device is subject to size and weight constraints for ease of installation and maintenance.

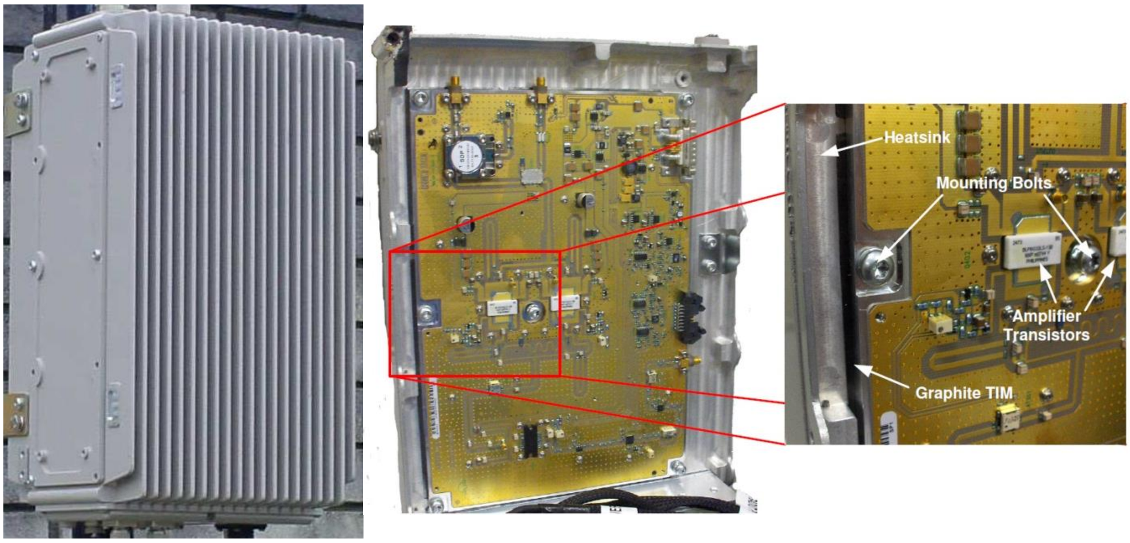

Figure 1.1 - Remote Radiohead box (for illustration purposes)

Current cooling mechanisms include conduction from the RFPA transistor to the finned enclosure and natural convection to the atmosphere. A number of factors can impact the reliability of the RRH, variable weather conditions subject the hardware to thermal cycling, while higher heat generation in the RFPA leads to a parasitic spread of heat through the electronic circuitry, as shown in Figure 1.2.

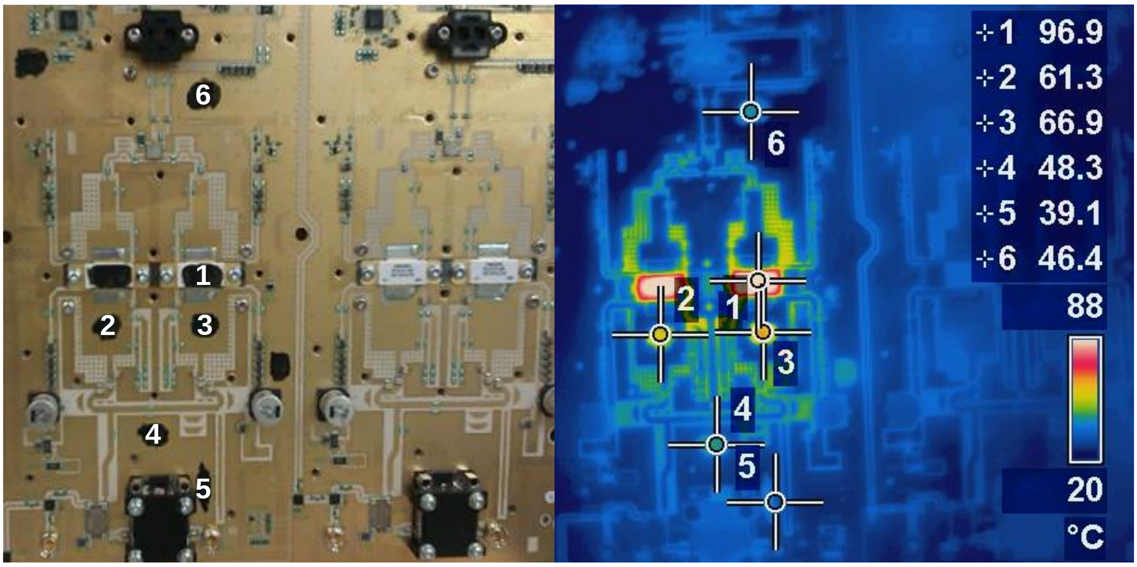

Figure 1.2 - Thermal imaging of heat spread from RFPA

Two-phase closed thermosyphons have the potential to provide effective cooling while adhering to these design constraints due to their high effective thermal conductivity, low cost and passive, reliable operation.

The objectives of this study were to investigate the feasibility of using a naturally aspirated thermosyphon system as a cooling and thermal control solution for telecommunications hardware and to understand the mechanisms determining the performance of the device, in terms of flow regimes and heat transfer. It is envisaged that by gaining an understanding of the factors influencing the two-phase flow behaviour and associated heat transfer performance of small-scale thermosyphons, design guidelines could be produced. In this way, the operation of such thermosyphons could be optimised for the required application. Further to this, the feasibility of controlling the thermal performance of the thermosyphon using electric fields is explored. It is proposed that the application of this technology could result in an intelligent thermal management system.

1.1. Thesis outline

The current work is divided into three main investigations, which develop and explore the objectives listed in the above section. Chapter 2 consists of an overarching literature survey, discussing topics relevant to all investigations in this work. Following this the chapters are divided according to each experimental study.

Within each chapter there is a dedicated literature review which is intended as an addition to Chapter 2 and discusses topics relevant to the particular investigation. Each investigation involved a different or modified experimental apparatus. For this reason, the experimental methodology of each study will be detailed individually in the associated chapter. Similarly, the results of each investigation will be discussed in turn in the relevant chapter.

In Chapter 3, a study of a small-scale thermosyphon for use in conjunction with telecommunications hardware is detailed. Considered in this chapter is the feasibility of a naturally aspirated thermosyphon for use as an electronics cooling device. Chapter 4 follows with an in-depth study of the flow regimes and associated heat transfer performance of a small-scale transparent thermosyphon. Chapter 5 documents the augmentation of the thermal performance of heat transfer in thermosyphons using electrohydrodynamics (EHD).

The results of these three investigations are summarised in Chapter 6 and recommendations for future work are outlined in Chapter 7.

2. Literature review

2.1. Thermosyphon operation

Thermosyphons have been recognised as simple, low cost and effective heat transfer devices [1]. The use of evaporation and condensation heat transfer within these devices means that the effective thermal conductivity of thermosyphons can exceed that of solid materials by several orders of magnitude [2 – 3].

In general, thermosyphons operate between a concentrated high temperature heat source and a low temperature heat sink. It is possible to transfer large amounts of heat over relatively large distances, even with a small temperature difference between the heat source and sink. Thermosyphons employ the use of gravitational forces to return the condensate to the heat source, or evaporator section as shown in Figure 2.1.

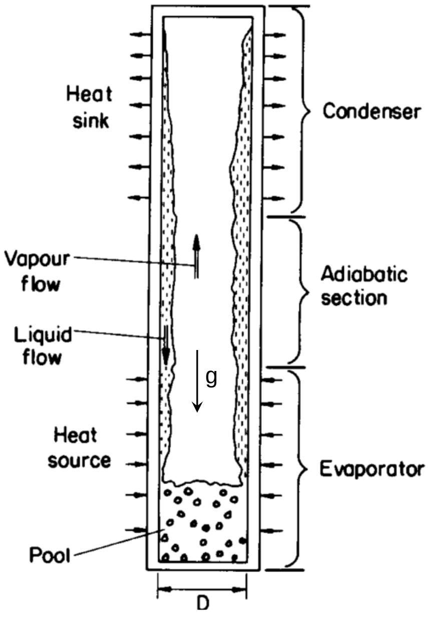

Figure 2.1 - Two-phase thermosyphon operation, adapted from [4]

In this way, their manufacture is simplified compared to heat pipes, in which a wick is installed to aid the return flow of condensate. However, there are some limitations to the operation of thermosyphons due to the fact that the liquid and vapour phases are flowing counter-currently.

Since the 1960's, many books and guides have been published giving comprehensive details on thermosyphons from device conception to performance optimisation, most notably E.S.D.U. [4], Faghri [5] and Reay *et al.* [3], along with the International Heat Pipe Conference proceedings. These references describe the main mechanisms of heat and mass transfer in thermosyphons. Heat is supplied to an evaporator section containing a small amount of working fluid which evaporates. In general, it is speculated that there is a combination of pool boiling in the lower evaporator sections, and also film evaporation in the upper section from the returning condensate. The evaporated vapour flows through the core region of the pipe to a condenser section which is externally cooled. Here the vapour condenses on the pipe wall and gravitational forces drive the condensate flow back to the evaporator section.

There is still uncertainty in the explanation of the complex mechanisms occurring during thermosyphon operation. This complexity is further compounded by the fact that thermosyphon performance is significantly affected by a large number of design parameters [6]. These parameters are basic to thermosyphon design, such as geometry, working fluid fill volume, thermophysical properties of the working fluid, inclination angle and saturation conditions. Prediction of thermosyphon behaviour on a general scale is extremely difficult due to these parameter variations. The range of variation in thermosyphon design and performance across the existing literature means that complete understanding of the heat and mass transfer within these devices is not fully understood.

With recent advances in technology and the electronics industry, more advance cooling solutions are being sought to cope with the growing issue of effective heat dissipation from higher heat flux sources [7 – 9]. As the size of electronics becomes smaller, investigation of small-scale thermosyphons has become popular on a mini and meso-scale. Reducing the form factor of two-phase devices can induce complications in the optimisation of the device, especially in the case of counter-current flow regimes, as are present in thermosyphons [10]. Boiling in small diameter tubes can present issues due to bubble confinement, resulting in flow behaviour that is quite different to traditional thermosyphon boiling models [11].

In an effort to maximise the performance of smaller scale thermosyphons, more complex thermosyphon designs have been produced. Looped heat pipes and capillary pumped heat pipes have eliminated the complexities of counter-current flow by incorporating separate liquid and vapour flow paths. These design modifications have been shown to greatly improve heat transfer compared to single phase solutions in high heat flux electronic components, as reviewed in detail by Franco & Filippeschi [12].

With regard to the design of conventional counter-current vertical thermosyphons, there is still very little literature on their performance at small diameters, $D_i < 10$ mm. A lack of visual observation of the internal flow in small diameter thermosyphons means the understanding of the physical mechanisms causing this behaviour is mainly based on speculation.

Visual studies of the two-phase flow in thermosyphons are uncommon, due to complication of design and practicalities. Existing research on visual analysis of thermosyphon fluid dynamics is in tubes of large diameter, $D_i > 10$ mm, and is not relevant considering the application of this work [13 – 18].

The focus of this research is on small diameter thermosyphons, of a dimension compatible with telecommunications hardware with tube diameters in the range of 3 mm < D_i < 10 mm (within conventional dimension as described by Kandlikar [19]) and steady operation was expected. The results however, point to instabilities and a visual analysis of the flow gives evidence of strong confinement effects. It is therefore proposed that thermosyphons of this scale are transitional in behaviour, showing properties inherent to both confined and conventional scale channels. The two-phase flow observed in this study were different to those conventionally described in the thermosyphon literature.

2.2. Thermosyphon heat transfer

The performance of a thermosyphon is generally described in terms of the heat transfer coefficient, h, or thermal resistance, R_{th}, of the evaporator and condenser section, separately. These values are related by Eqn. (2.1).

$$R_{th} = \frac{1}{A \cdot h}$$

Eqn. (2.1)

Therefore, optimum thermosyphon performance is one where the thermal resistance is minimised across the evaporator and condenser sections. In order for this to be possible, the most effective mechanisms of boiling and condensation are preferable. These mechanisms depend on the saturation conditions within the thermosyphon and the thermophysical properties of the working fluid. Prediction of the heat transfer coefficient in thermosyphons is complicated by the sensitivity to design as mentioned in Section 2.1.

2.2.1. Condensation heat transfer

The rate of heat transfer in the condenser section is influenced by the condensate and vapour flow. The effectiveness of the different modes of condensation heat transfer are given in [20]. In general, it is understood that the condensate forms a liquid film on the wall of the thermosyphon. The heat transfer coefficient in the condenser section is generally predicted using the Nusselt theory for falling liquid films, Eqn. (2.2).

$$h_{Nusselt} = 0.943\left\{\frac{\rho_l(\rho_l - \rho_v)gk_l^3\left[h_{fg} + 0.68C_{pl}(T_v - T_c)\right]}{\mu_l(T_v - T_c)L_c}\right\}^{0.25}$$

Eqn. (2.2)

Chen *et al.* [21] studied reflux condensation in a two-phase closed thermosyphon of large dimension using water and methanol as the working fluid. It was found that Nusselt Theory over-predicted the heat transfer coefficient compared to the experimental data. It was suggested that the shear effects between the liquid and vapour phases within the thermosyphon caused an increase in the condensate film thickness, reducing the heat transfer in this region. However, accounting for these shear effects did not make up for the discrepancies in the observed with Nusselt's Theory.

Gross [22] proposed that Nusselt's Theory does not correlate well with all experimental conditions. Data from a number of different research facilities was presented in [22] and a modified equation for reflux condensation heat transfer was proposed. This new correlation showed a ± 10 % agreement with over 50 % of the experimental data used. It was also noted that the rate of condensation heat transfer deteriorated with high vapour velocities, due to an increase in film thickness in the condenser region. This scenario is common in thermosyphons where the interface between the liquid and vapour are subject to high shear forces. Liquid droplets from the falling condensate are pulled into the vapour core and propelled upwards to the condenser section, thickening the film in this region. The phenomenon is called flooding or entrainment and presents a limitation in the heat transfer capabilities of thermosyphons.

Other research has also recognised the limits of using Nusselt Theory in predicting thermosyphon condensation heat transfer. Modification factors have been proposed which account for the discrepancies with Nusselt's Theory when applied to reflux condensation heat transfer in thermosyphons. Hashimoto and Kaminaga [23] experimentally investigated reflux condensation in a thermosyphon at low Reynolds numbers. They found that the condensation heat transfer was negatively affected by the entrainment of liquid droplets into the upward vapour flow. Again, Nusselt Theory over-predicted the condensation heat transfer and a correction factor that would account for entrainment in thermosyphon counter-current flows was proposed, Eqn. (2.3).

$$h_c = 0.85 Re_l^{0.1} \exp\left[-0.000067\left(\frac{\rho_l}{\rho_v}\right) - 0.6\right]\left\{0.943\left[\frac{\rho_l(\rho_l-\rho_v)g k_l^3 h_{fg}}{\mu_l(T_v-T_c)L_c}\right]^{0.25}\right\} \qquad \textbf{Eqn. (2.3)}$$

Where

$$Re_l = \frac{4Q}{\pi D h_{fg} \mu_l} \qquad \textbf{Eqn. (2.4)}$$

Jouhara and Robinson [24] experimentally investigated heat transfer in small diameter thermosyphons using a range of working fluids: water, FC-84, FC-77 & FC-3282. They also found that the Nusselt theory was inadequate in accounting for the liquid entrainment, especially at low power conditions. A modification of the equation given by [23] was proposed based on a regression analysis of experimental data.

2.2.2. Boiling behaviour in thermosyphons

The mechanisms of heat transfer in the evaporator section are thought to be more complex, with evaporation occurring simultaneously in both the liquid pool and the falling liquid film. The sensitivity of the thermosyphon performance to operating conditions means it very difficult to predict the behaviour occurring inside. As many thermosyphons are built using opaque metals, the heat transfer mechanisms occurring within the evaporator have only been speculated upon. Such speculation is based on correlations with existing equations for different modes of boiling. Typically, empirical data is compared to a number of equations to find the best fit for a particular experiment.

Baba *et al.* [25] determined that boiling systems are influenced by surface tension, inertia and gravitational/body forces due to the density difference between phases, as characterised by Reynolds and Satterlee [26]. The interaction and relationship between these forces for a particular system can be represented by the Weber, Bond and Froude numbers.

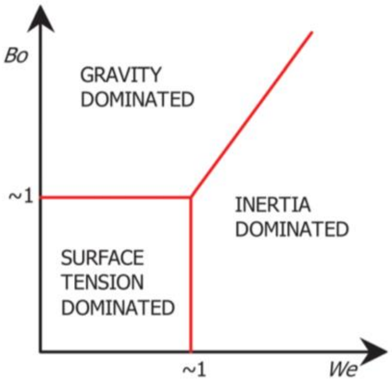

Figure 2.2 - Surface tension, inertia and gravity dominated regions, source: [27]

The Weber number describes the relationship between inertia and surface tension forces of two-phase flow. Pool boiling is characterised by low Weber numbers, where interfacial forces dominate creating discrete bubbles. The surface tension forces to body/gravitational forces are represented by the Bond number. The Bond number describes the active forces during bubble growth and detachment from a surface, where gravity and body forces will dominate at high Bond numbers. The Froude number is a ratio of the Bond and Weber numbers and represents the inertial to gravitational forces.

The Rohsenow correlation [28], Eqn. (2.5), is generally accepted to correlate heat transfer coefficients in the nucleate boiling regime. This can be rearranged to give the boiling heat transfer coefficient, Eqn. (2.6) using the relation $q = h\Delta T$.

$$\frac{C_{pl}\Delta T_b}{h_{fg}} = C_{sf}\left[\frac{q\lambda_c}{\mu_l h_{fg}}\right]^{0.33} Pr_l^{1.7} \qquad \textbf{Eqn. (2.5)}$$

$$h_e = \frac{q^{0.66}}{\frac{C_{pl}\cdot C_{sf}}{h_{fg}}\left[\frac{\lambda_c}{\mu_l h_{fg}}\right]^{0.33} Pr_l^{1.7}} \qquad \textbf{Eqn. (2.6)}$$

Park *et al.* [29] conducted experiments in a thermosyphon, using FC-72, which investigated the working fluid fill ratio and the influence of surface grooves on thermosyphon performance. It was found that the Rohsenow correlation best predicted the heat transfer coefficient for smooth surfaces. Pioro [30] investigated the accuracy of prediction methods of nucleate pool boiling using existing equations proposed by Rohsenow, Kutateladze, Labuntsov, Kruzhilin and the author. They confirmed that the Rohsenow correlation showed the best agreement for the conditions under investigation and accounting for the particular fluid/surface combination.

Other empirical and semi-empirical pool boiling correlations exist in the literature, given in [10], [31 – 33]. Of particular relevance is the correlation proposed by Imura *et al.* [31], Eqn. (2.7).

$$h_e = 0.32\left(\frac{\rho_l^{0.65}k_l^{0.3}C_{pl}^{0.7}g^{0.2}}{\rho_v^{0.25}h_{fg}^{0.4}\mu_l^{0.1}}\right)\left(\frac{P_v}{P_{atm}}\right)^{0.3} q^{0.4} \qquad \textbf{Eqn. (2.7)}$$

This equation was based on a least square correlation with their experimental data of heat transfer within a closed two-phase thermosyphon. More recently, Noie [2] found the Imura correlation to be within good agreement with heat transfer coefficients for their experimental conditions.

Chowdhury [33] investigated boiling heat transfer in a natural circulation loop using three different working fluids: water, ethanol and Freon R-113 in a very small diameter tube, D_i = 2.8 mm. They proposed a correlation for pool boiling which accounts for the influence of both the density ratio at reduced pressures, and Confinement number effects in small diameter tubes.

El-Genk and Saber [10] proposed a correlation for three different heat transfer regimes (natural convection, combined convection and nucleate boiling) within the evaporator section and a condition for transition between these regimes. In this paper over 700 heat transfer data points from various different researchers were sorted into different regimes and compared to new and existing correlations for heat transfer. The data covered a wide range of internal diameters, 6 mm < D_i < 37 mm, and a variety of working fluids: water, ethanol, methanol, Dowtherm-A, R-11 and R-113. A mixing coefficient, ψ, was proposed which accounted for the motion of sliding and rising bubbles in the liquid pool during nucleate boiling. The heat transfer coefficient proposed for the nucleate boiling regime was based on a combination of the heat transfer correlation proposed by Kutateladze and the mixing coefficient. This equation showed agreement within ± 15 % of the experimental data and accounted for the importance of the confinement effects in small diameter tubes.

2.3. Limitations to heat transfer

The relevant limitations to heat transfer in thermosyphons are presented in this section. The limitations represent the mechanisms which result in failure of the thermosyphon whereby heat transfer between the evaporator and condenser section ceases. These limits are described in more detail in [4 – 5] along with correlations to predict the onset of failure due to the limitations.

The flooding limit, or entrainment limit, is a result of the interfacial shear stress between the liquid and vapour phases. As the velocity difference between the vapour and liquid is increased, the liquid-vapour interface becomes wavy and unstable. The vapour velocity will accelerate with increasing imposed heat flux and can overcome the surface tension force of the liquid, pulling liquid droplets from the wall and into the vapour core. With further increase in the heat flux, all condensate can be prevented from returning to the evaporator. The working fluid accumulates in the condenser section, reducing heat transfer in this region. In the evaporator, there are large excursions of the wall temperature and dryout of the evaporator wall can occur.

The dryout limit in thermosyphons is a result of inadequate fill volume of the working fluid. This limit is reached when all of the liquid has evaporated and exists either in the falling film regime or in the vapour core and there is no liquid pool remaining in the evaporator section. Dry patches begin to grow from the bottom of the evaporator section, increasing in size with heat flux. The wall temperature in the evaporator section can increase rapidly at dryout as there is no longer any evaporation occurring.

The boiling limit is encountered in thermosyphons at high heat fluxes. At the critical heat flux, evaporation is so vigorous that film boiling occurs. Vapour bubbles coalesce at the wall surface and prevent the liquid from rewetting the surface. Evaporation ceases and the evaporator wall temperatures can rise exponentially due to the high imposed heat flux.

Models for the critical heat flux in thermosyphons due to each of these limits have been developed and are presented in [3 – 5]. The majority of these predictions of maximum heat flux are focussed on the flooding or entrainment limit. Most flooding limit correlations are based on that of Wallis [34], which calculates the balance between inertial and buoyancy forces, or Kutateladze [35] which, in addition to [34], takes account of the surface tension forces. Tien and Chung [36] combined the results of [34] and [35] to account of the dimensional effects of the thermosyphon. Faghri [37] further developed [36] to take account of fluid properties and this is considered the most general flooding correlation.

More recently, El-Genk and Saber [38] presented an operational envelope for the optimum fill ratio of two-phase closed thermosyphons based on the geometry, saturation conditions and imposed heat flux. The boundaries of the operation envelope referred to the entrainment, boiling and dryout limits. It was found that the size of the operational envelope is proportional to evaporator aspect ratio, and increasing saturation conditions. Jiao *et al.* [39] also investigated the effects of fill ratio on the critical heat flux due to flooding, dryout and boiling limits in two-phase closed thermosyphons. Experimental results, using nitrogen as the working fluid, showed good agreement with calculated results. A maximum fill ratio was proposed which produced optimum thermosyphon performance before the onset of limitations. An operational range was proposed for the vertical two-phase thermosyphon, which was also analysed for sensitivity to geometry and pressure conditions.

2.3.1. Effects of confinement on boiling in thermosyphons

With decreasing form factor, the operation of the thermosyphon can be subject to heat and mass flow restrictions due to confinement of the working fluid phases within the tube. There is less space in the annulus of the thermosyphon for the upward vapour flow, leading to a complex interaction of capillary, buoyancy and inertial forces at the confined liquid-vapour interface. The factors affecting heat transfer in small-scale thermosyphons, therefore, are the thermophysical properties of the working fluid, fill volume, and the dimension of the tube. Operating conditions, such as pressure and heat flux, should also be taken into account.

Due to the change in thermophysical properties of the fluid with pressure, there will also be a change in the size of the bubbles as the pressure of the system changes. Larger bubbles are present at lower pressures, due to the rapid increase in vapour specific volume with reducing pressure, and hence bubble growth is enhanced. For this reason, the reduced pressure, $P_r = P/P_{crit}$, for each particular experiment is important.

The definition of *'small-scale'* can vary in the existing literature. In a recent review of micro channel flow, Ribatski [40] discussed the existing transitions from micro to macro scale. In a comparison of 9 different studies it was evident that conventional scale behaviour is expected in diameters around 6 mm, with reduced pressure conditions ranging from $0.001 < P_r < 0.8$.

Bubble departure size has been studied in fundamental boiling research over a range of experimental conditions [20], [41]. The Laplace length, or capillary length, λ_c, represents a balance of liquid surface tension and liquid-vapour buoyancy forces, Eqn. (2.8). This length is used to describe the characteristic bubble departure diameter using the thermophysical properties of the fluid at the operating pressure.

$$\lambda_c = \sqrt{\frac{\sigma}{(\rho_l - \rho_v)g}} \qquad \textbf{Eqn. (2.8)}$$

The Confinement number, Co, is a ratio of the bubble departure size, λ_c, to the channel diameter, D_i, Eqn. (2.9). This quantifies the level of confinement of growing bubbles for a given channel diameter, expressed as the following equation:

$$Co = \frac{\lambda_c}{D_i} = \frac{1}{D_i}\sqrt{\frac{\sigma}{(\rho_l - \rho_v)g}} \qquad \textbf{Eqn. (2.9)}$$

Fluid and channel size conditions giving high values of Confinement number, $Co \sim 1$, indicate a large bubble size relative to channel size, typical in micro-scale flow. Conversely, $Co \ll 1$ represents a situation resembling small bubbles in an infinitely large pool. For smaller diameter thermosyphons, the confinement number indicates the benefits of high vapour pressure fluids, as they should produce smaller bubbles.

For channel flow regimes, Ong and Thome [11] described a transition region between micro and macro scale flow behaviour, referred to as meso-scale, using Co. It was found that this transition regime was present for $0.3 < Co < 0.4$. Conventional channel flow is expected for $Co < 0.3$.

Franco and Filippeschi [14], and Jouhara and Robinson [24], used the Laplace length scale to define small dimension thermosyphons as one which $D_i = 2\lambda_c$. The rationale for using this relationship in [24] is the disturbance of the flow when two bubbles orientated in opposing directions grow and interact at half the tube diameter.

Confinement can affect the heat transfer performance of thermosyphons, resulting in a more transient operation with fluctuations in pressure and temperature. This phenomenon has been referred to in the literature as the Geyser effect. The Geyser effect describes nucleating bubbles which quickly grow to the size of the thermosyphon tube, trapping some volume of the liquid pool above. Evaporation from the liquid film surrounding the bubble causes further increase in bubble size and the liquid plug is forced into the condenser section where it can collide with the end wall of the thermosyphon. Once the subcooled liquid plug returns to the evaporator there is a quiet period as the liquid pool temperature rises to the necessary superheat for another boiling event to occur. Though the oscillation of liquid plugs is not desired in thermosyphon behaviour, this behaviour is not a limitation of performance but represents a pseudo-steady state of operation where there is a significant contribution of sensible heat transfer. This could explain the over-prediction of nucleate boiling heat transfer coefficients, which predict high rates of heat transfer due solely to the latent energy involved in phase change.

The geyser effect was studied by Casarosa *et al.* [18] and a heat transfer analysis was accompanied with visual images of the behaviour. Water was used as the working fluid at a low pressure condition. It was found that the frequency of oscillation increased with increasing heat flux. The evaporation heat transfer coefficient showed poor agreement with existing nucleate boiling correlations; however, a correlation was made relating the heat transfer coefficient to the imposed heat flux and the vapour pressure.

More recently, Khazee *et al.* [42] investigated geyser boiling in thermosyphons with varying diameter, fill ratio and heat input. They found that geyser boiling was only present in cases where the fill ratio was greater than 30%. The frequency of oscillation in their experiment was found to be proportional to the fill ratio, but inversely proportional to the imposed heat flux and aspect ratio of the evaporator section. An equation to predict the period of geyser oscillations was also proposed based on the experimental data.

Filippeschi *et al*. [43] investigated boiling in miniature pools of FC-72 in periodic two-phase thermosyphons. In such a system the evaporator section experiences periodic dryout. The study reported that, as the volume of the liquid pool is decreased, there is a greater deviation from nucleate pool boiling in the evaporator and an unstable transient boiling regime is dominant.

Jouhara *et al.* [44] investigated a two-phase closed thermosyphon in which the condenser section was axially offset from the evaporator by an angle of 12°. A mixture of water and ethanol was used as the working fluid and compared to operation with pure water, and a range of inclination angles were tested. It was found that the presence of ethanol with water drastically reduced the presence of geysering at lower powers in the evaporator section. The water-ethanol mixture provided the same heat transfer performance as that of pure water. It was also found that the inclination angle did not have an effect on the performance of the thermosyphon.

Confined flow boiling is harnessed in the operation of other types of thermosyphons and heat pipes, such as oscillating heat pipes and capillary pumped loop heat pipes. These devices have been designed to cope with oscillatory behaviour of fluids at small dimension and are described in [1].

Overall, the common factors in the presence of geyser boiling in the existing literature is the use of water as a working fluid, high fill ratios, and low pressure conditions. However, there are still large variations in the experimental parameters investigated. Table 2.1 gives an overview of the experimental conditions described in the existing literature in which geyser boiling was encountered. This highlights a need for further work in the area of small diameter channels at varying pressure conditions, particularly within 0.2 < *Co* < 0.4. For a full understanding of the confinement behaviour, more recent visual analysis of the flow needs to be conducted.

Reference	D_i **[mm]**	**Working fluid**	**Fill ratio [%]**	P_r	λ_c **[mm]**	***Co***
Casarosa *et al.* [18] (*)	42	Water	> 112	$1.87\ \text{x}10^{-4}$	2.7	0.06
Negishi *et al.* [45] (*)	15	Water Ethanol	5 – 100	$1.87\ \text{x}10^{-4}$ $1.56\ \text{x}10^{-3}$	2.7 1.7	0.21 0.12
Negishi [46] (*)	22	Water	30	$2.47\ \text{x}10^{-4}$	2.7	0.12
Lin *et al.* [47] (*)	29.6	Water Ethanol	30 – 140	$1.38\ \text{x}10^{-4}$ $1.56\ \text{x}10^{-3}$	2.7 1.7	0.09 0.06
Kuncoro [48] (*)	18	Water R-113	100	$1.47\ \text{x}10^{-4}$ $1.06\ \text{x}10^{-2}$	2.7 1.1	0.15 0.06
Abreu *et al.* [49]	15	Water	60 – 80	$8.18\ \text{x}10^{-4}$	2.7	0.18
Noie [2]	25	Water	30 – 90	$1.25\ \text{x}10^{-3}$	2.6	0.11
Sarmasti Emami *et al.* [50]	14 – 24	Water	15 – 45	$2.47\ \text{x}10^{-4}$	2.7	0.19
Khazee *et al.* [42]	15 – 25	Methanol	30 – 100	$3.46\ \text{x}10^{-3}$	1.7	0.11
Jouhara *et al.* [24]	6	Water	80 – 160	$5.21\ \text{x}10^{-4}$	2.7	0.45
Jouhara *et al.* [44]	20.2	Water	50	$8.18\ \text{x}10^{-4}$	2.7	0.13

Table 2.1 - Summary of geyser boiling investigations [(*) denotes transparent test sections]

2.4. Summary

Highlighted in this chapter is a need for further research into counter-current, two-phase flow behaviour in small-scale channels, and the consequences of the flow regimes on the heat transfer performance. It is clear that there are some adverse effects on the flow regimes as the channel size is reduced, especially for the case of thermosyphons where the liquid and vapour phases are opposed in flow direction. The entrainment limit is most commonly encountered in thermosyphon operation, and is a major factor in causing failure of these devices.

The above discussion outlines some key gaps in the existing knowledge with regard to understanding the behaviour and performance of thermosyphons, particularly of small dimension. The limited previous work in the range $0.2 < Co < 0.4$ in vertical counter-flow thermosyphons was highlighted.

Much of the existing literature investigates the thermal performance of metal thermosyphons, where the mechanisms of heat transfer are inferred from temperature and pressure measurements. A visual study of thermosyphons with small dimension is required in order for the two-phase flow behaviour over a range of operating conditions to be understood fully.

3. Feasibility study

3.1. Introduction

The focus of this investigation is to assess the performance of a naturally aspirated thermosyphon in cooling telecommunications based hardware, particularly Radio Frequency Power Amplifiers (RFPA) installed in Remote Radioheads (RRH). The design of a cooling solution for such an application is complicated by the operational requirements, due to the tower top location of this hardware there are size and weight constraints for ease of installation and maintenance. Considering the RRH is situated outdoors, thermal cycling of the electronic components is a concern as it can impact the reliability and functionality of the circuitry.

The design of a thermosyphon for this particular application is further complicated by shape and size restrictions, where bends may need to be incorporated into the geometry. In counter-current flow regimes such as those present in thermosyphons, bends may pose a further limitation to the heat and mass transfer.

This study aims to investigate the thermal performance of a thermosyphon design incorporating bends between the evaporator and condenser sections. The thermosyphon performance is assessed in terms of its viability for use as an electronics cooling solution.

3.2. Literature review

The existing literature relevant to the current study of thermosyphon design and performance are outlined in this section. The topics specific to this investigation were the effect of inclination, bends in the geometry and working fluid fill volume on the performance of the thermosyphon.

3.2.1. Effect of inclination angle

The inclination angle of a thermosyphon can affect its performance in terms of heat transfer capability. To date much of the research into thermosyphon inclination has been carried out on straight test sections where the whole apparatus has been tilted at an angle.

Work by Nguyen-Chi and Groll [51] noted a significant influence of the inclination angle on thermosyphon performance. It was found that the maximum rate of heat transfer occurs between an angle of 40° and 60° to the horizontal plane. Their research also found that the fill ratio had a more significant effect on the rate of heat transfer at higher inclination angles. Payakaruk *et al*. [52] showed that the inclination angle could in some cases assist the return of condensate to the evaporator, increasing the operational limits of the heat pipe. Most often it has been found that there is an optimum tilt angle range in which the heat transfer capability of the thermosyphon is enhanced.

3.2.2. Effect of bend angle

There is little existing literature on thermosyphons with only one section at an inclined angle, or a bend in the test section geometry. Lock [53] conducted experiments on an "elbow" type thermosyphon, with a 90° bend between the evaporator and condenser. Two different orientations were tested to measure the influence of bend angle on condenser and evaporator performance. It was found the failure mechanism differed for each of the two cases. For the case of a vertical condenser/horizontal evaporator, the failure mechanism was a dryout failure as the liquid was prevented from returning to refill the evaporator. The vertical evaporator test indicated that fluid was not draining fully from the horizontal condenser section, while a liquid pool remained in the lower evaporator section, referred to as the flooding limit. Though this study established the investigation of bends in thermosyphon design, there has been little further experimental research into additional bend angles.

McKee and Hobbs [54] developed a flexible thermosyphon that was capable of folding at an angle up to 180° along with computational code to predict the power limits of the flexible thermosyphon. On comparing the computational and experimental results it was found that the computer code over predicted the power limits by 200 %. This was most likely due to flow restrictions imposed by the bends in the adiabatic section, resulting unexpected flow behaviour.

3.2.3. Effect of fill ratio

The volume of working fluid contained in the thermosyphon has an impact on the thermal performance, with most researchers reporting an optimum filling range over which the heat transfer capability is enhanced. A summary of minimum liquid requirements has been detailed in thermosyphon design guides, Faghri [5], Reay and Kew [3] and E.S.D.U [4]. The filling ratio is usually described as the volume of working fluid relative to the volume of the evaporator, or in some cases, total thermosyphon volume. El-Genk and Saber [38] proposed an operation envelope which details the limits of closed two-phase thermosyphon (CTPT) performance with respect to the filling ratio and input power, as shown in Figure 3.1. The closing boundary for the thermosyphon operation occurs with the counter-current flooding limit (CCFL).

A more recent study by Jiao *et al*. [55] developed a computational model to predict the effects of filing ratio on the thermal performance of a thermosyphon at steady state. This study concludes that the evaporator filling ratio should be kept in the range proposed by El-Genk and Saber [38], as shown in Figure 3.1. It is also confirmed that the boundaries of the filling ratio envelope are inversely proportional to the heat input, but proportional to the operating pressure and tube diameter. This model was further developed to include dryout, flooding and boiling criteria and the influence of the filling ratio [39]. These predictions are more comprehensive in their modelling of the behaviour of the thermosyphon with varying heat input.

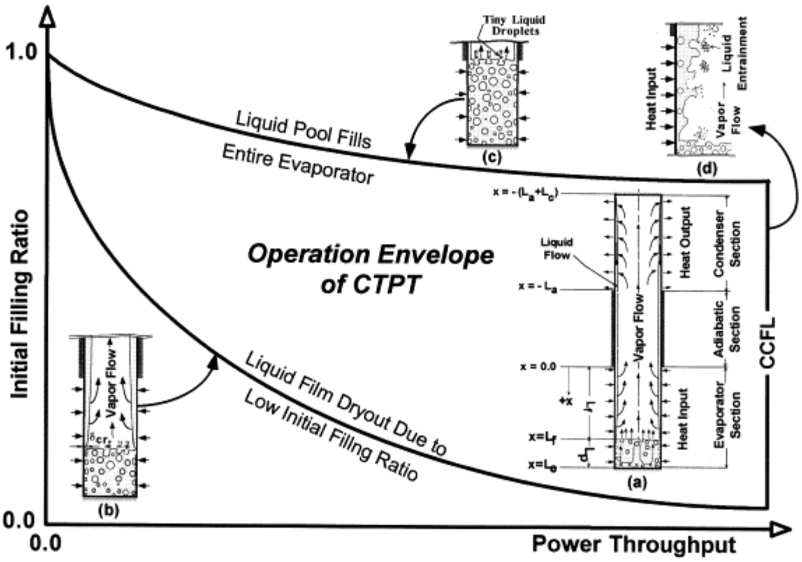

Figure 3.1 - Operation envelope of a thermosyphon, [38]

3.2.4. Summary

The need for further research of thermosyphon design with sizes and shapes applicable to telecommunications hardware has been outlined here. The lack of existing research on the operation of reflux thermosyphons with more complex geometry was also highlighted.

The goal of the work in this chapter is to determine the capability of a small dimension thermosyphon designed specifically for RFPA cooling applications. A more complex thermosyphon geometry with bends was considered to address the size and weight limitations imposed by the application. These flow restrictions will inherently have an effect on the heat transfer of the device, and therefore require further investigation.

3.3. Experimental methodology

In this investigation, the performance of four thermosyphons having bends in the adiabatic section of 0°, 30°, 60° and 90° from vertical will be studied, along with the effect of working fluid fill volume, V_f. In order to realistically represent the operation conditions for the proposed application, the condenser section for each test consisted of a radially finned heat sink, with no forced convection, so that the effectiveness of thermosyphon cooling by natural convection could be investigated. High watt density heaters were used to represent the RFPAs. The performance of the thermosyphon was quantified by measuring the thermal resistance in each of the sections for increasing power levels similar to those which would typically be experienced in industrial applications.

3.3.1. Experimental apparatus

A schematic of the experimental apparatus is illustrated in Figure 3.2. The evaporator of the thermosyphons used in this experiment consisted of a rectangular copper block of dimensions 70 x 20 x 30 mm. A cylindrical hole, 16.7 mm diameter, was drilled through the centre of the copper block to serve as the interior boiling surface. Heat was applied to one side of the evaporator section using two Watlow Ultramic ceramic heaters (25 x 15 x 2.5 mm), each with a maximum power of 180 W. The heaters were bolted to the evaporator using clamps, and thermal paste ensured good contact with the evaporator wall surface. The heaters were powered by a variable voltage transformer and the power was measured using multimeters. The temperatures of the heaters were measured using internal K-type thermocouples (numbered 5 & 6 in Figure 3.2). A uniform heat flux distribution was assumed across the copper evaporator section. This assumption was validated using a Biot number analysis, detailed in Appendix A.

The thermosyphon condenser section consisted of a radially finned anodized aluminium heat sink, with an external diameter of 150 mm and internal diameter 35 mm (TitanTurbo heat sink model number: HS-5430-0537). The heat sink was modified such that the top end was sealed, and the bottom drilled and tapped to allow a plumbed connection to the adiabatic section. The chamber formed by the inner diameter served as the condensation surface of the thermosyphon. Heat was then conducted outwards through the radially mounted fins for dissipation to the surroundings by natural convection.

The evaporator and condenser sections were each fitted with two Ø 1 mm T-type, stainless steel sheathed thermocouples, one fitted in the section wall and one in the vapour core (numbered 1 – 4 in Figure 3.2). Internal pressure was measured in the system using an absolute pressure transducer (Omega PX01-5T), located in the condenser section. All pressure and temperatures in the system were recorded using a data acquisition (DAQ) system and National Instruments LabView.

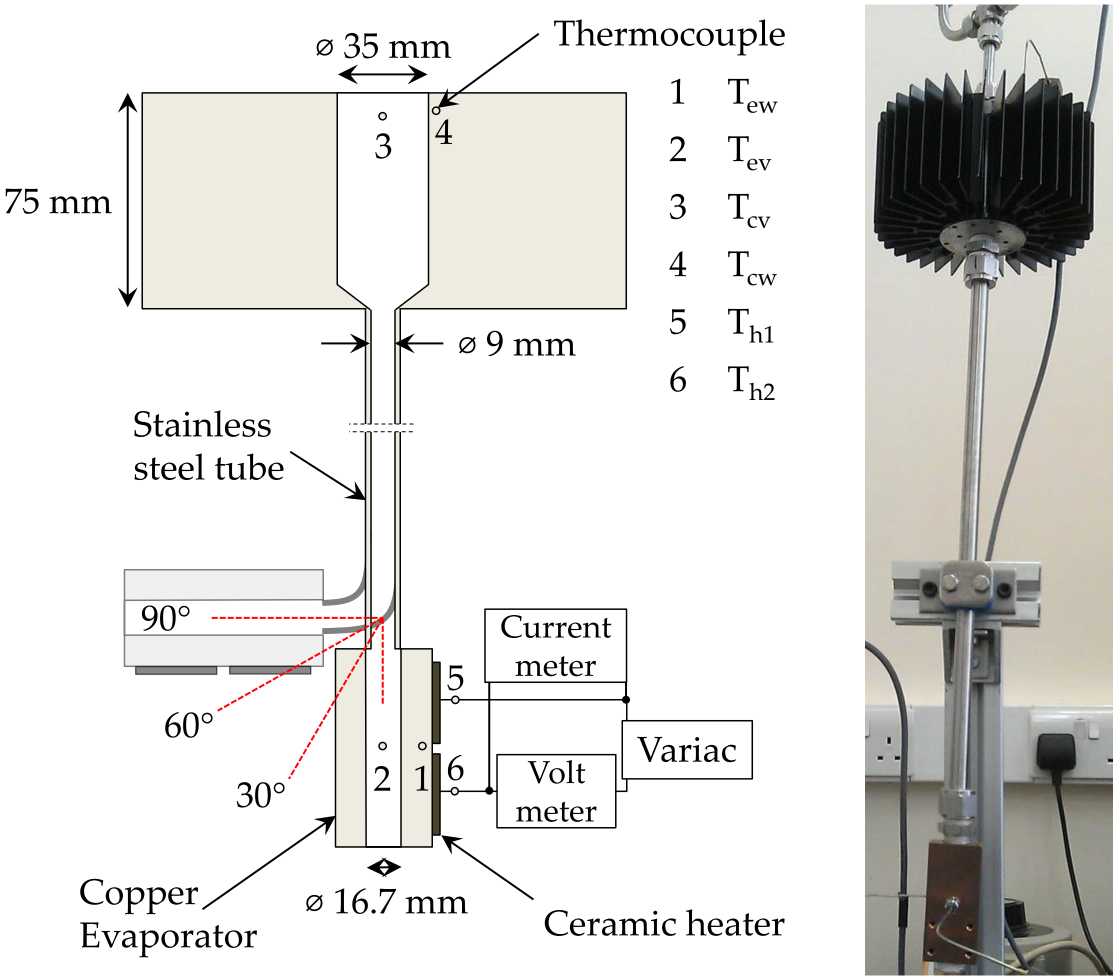

Figure 3.2 - Schematic of stainless steel thermosyphon with bends

The evaporator and condenser sections were connected using a stainless steel adiabatic tube with an internal diameter of 9 mm. To investigate the effects of changing bend angle, equal lengths of 400 mm stainless steel tubing were bent to angles of 30°, 60° and 90° from the vertical plane, and these were also compared to a straight vertical tube (denoted 0°). Each of the bent adiabatic sections was created using the same pipe bending device, having a radius of curvature, $R_c = 38$ mm. This resulted in a bend radius, $R_c/D_o \sim 3$. The evaporator and adiabatic sections were wrapped in high temperature insulation to prevent ambient heat losses.

In order to limit the presence of non-condensable gas, the thermosyphon was evacuated using a vacuum pump for 30 minutes prior to testing to a pressure of 0.1 bar. Degassed water was chosen as the working fluid. The fill volume of working fluid was measured using a graduated burette. The fluid volume, V_f, for each bend angle were such that the evaporator section was half-filled ($V_f = 7.5$ mL), full ($V_f = 15$ mL) and over-filled ($V_f = 22.5$ mL), corresponding to filling ratios of 50 %, 100 % and 150 % respectively.

3.3.2. Data reduction

The uncertainty associated with the experimental measurements was quantified using the manufacturer's specification for each device, as shown in Table 3.1.

Measurement	Device	Experimental uncertainty
Temperature	Omega T-type thermocouple	± 0.5 °C
Heater temperature	K-type thermocouple	± 1 °C
Pressure	Omegadyne pressure transducer	± 3 %
Voltage	Metrix MX22 multimeter	± 1 %
Current	Metrix MX22 multimeter	± 1.2 %

Table 3.1 - Uncertainty in measured parameters

The overall thermal resistance, R_{tot}, of the thermosyphon was calculated using Eqn. (3.1) as outlined in E.S.D.U. [4]. Similarly, the thermal resistances in the evaporator and condenser sections, R_e and R_c, were calculated using Eqn. (3.2) and Eqn. (3.3). The temperatures T_{ew}, T_{ev}, T_{cw}, and T_{cv} are time averages of the quasi-steady-state temperatures taken from thermocouples in the evaporator wall, evaporator vapour, condenser wall and condenser vapour respectively.

$$R_{tot} = \frac{\overline{T_{ew}} - \overline{T_{cw}}}{Q}$$ **Eqn. (3.1)**

$$R_e = \frac{\overline{T_{ew}} - \overline{T_{ev}}}{Q}$$ **Eqn. (3.2)**

$$R_c = \frac{\overline{T_{ev}} - \overline{T_{cw}}}{Q}$$ **Eqn. (3.3)**

The propagation of error through the calculated parameters was evaluated using the method outlined by Kline and McClintock [56], as shown in Eqn. (3.4):

$$\Delta f = \sqrt{\sum_{i=1}^{n} \left(\frac{\partial f}{\partial x_i} \Delta x_i \right)^2}$$ **Eqn. (3.4)**

To account for losses the total uncertainty associated with the power measurement was estimated to be ± 5 %. Considering the uncertainty of temperature and power measurements, the propagation of error in the thermal resistance was calculated to be within a maximum of 8 %, shown in Table 3.2.

Appendix B. outlines the ambient heat losses from the stainless steel thermosyphon wrapped in high temperature insulation. These losses are small enough to be assumed negligible.

Power	**40 W**	**70 W**	**100 W**	**150 W**	**200 W**	**250 W**	**300 W**
Uncertainty in R_{tot}	6.0%	6.8%	7.5%	7.9%	6.7%	7.0%	6.2%

Table 3.2 - Propagation of error in R_{tot} with changing input power

3.4. Results and discussion

The following sections analyse the performance of the thermosyphon. Firstly, the case of the straight vertical thermosyphon (0° bend) and the mid fluid loading (100 %) will be discussed in detail in terms of the overall behaviour across the range of power inputs tested. Following this the heat transfer of this initial case will be compared and contrasted to those of the other bend angles and fill volumes. Finally, the failure mechanisms of the thermosyphon are proposed based on this analysis. The findings of each of these sections are then evaluated in terms of the practical application goal of this work, namely using thermosyphons as heat transfer devices in telecommunications hardware.

3.4.1. Behaviour of vertical thermosyphon under thermal loading conditions

The results of the straight vertical (0°) thermosyphon present some interesting trends in terms of temperature and pressure oscillations at both low and high power levels, with steady operation at intermediate powers. As there is no visual access to the thermosyphon, the temperature and pressure transients are used to infer the mechanisms of boiling taking place. For illustration, the following results are presented for the 0° thermosyphon, with $V_f = 15$ mL.

Figure 3.3 shows the temperature and pressure time trace plots for the thermosyphon at $Q = 40$ W. Here, it is evident that there are fluctuations in the evaporator vapour temperature, and also in the associated pressure. Due to the low power setting, and low pressure and temperature in the evaporator, this indicates geyser boiling in the evaporator [5], [27], [42], [47], [50]. Geyser boiling is commonly encountered with large filling ratios and high density differences, whereby a vapour bubble forms and increases in size along the length of the thermosyphon, often forcing a slug of liquid to the top of the thermosyphon. This slug of liquid can strike the end cap of the condenser, producing an audible ticking sound during thermosyphon start up. Once this liquid hits the condenser cap it falls back to the evaporator as a liquid film on the thermosyphon wall. The fluctuations in temperature and pressure associated with geyser boiling can be seen in the temperature of both the condenser and evaporator vapour, and to a lesser extent in the wall temperature of each section, shown in Figure 3.3.

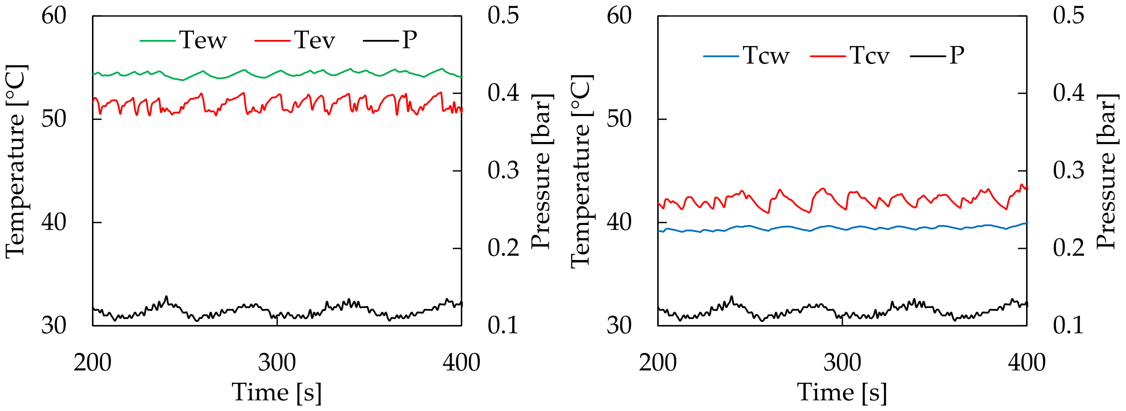

(a) (b)

Figure 3.3 - Temperatures and pressure at 40W in (a) the evaporator and (b) the condenser showing geyser boiling

For increasing power levels, 40 W > *Q* > 70 W, the oscillatory trends in temperature of the evaporator wall and vapour are evident in the standard deviation plots of Figure 3.4. In these figures the geysering phenomenon is evident for low power levels *Q* < 70 W, as shown by an increase in standard deviation of the temperatures in this region. Figure 3.4 highlights more stable behaviour of the thermosyphon as the power input is increased from 70 W to 150 W, with no large fluctuations in temperature and pressure. This indicates that between 70 W and 150 W the heat transfer in the evaporator is steadier, which suggests the thermosyphon is operating within the nucleate boiling regime.

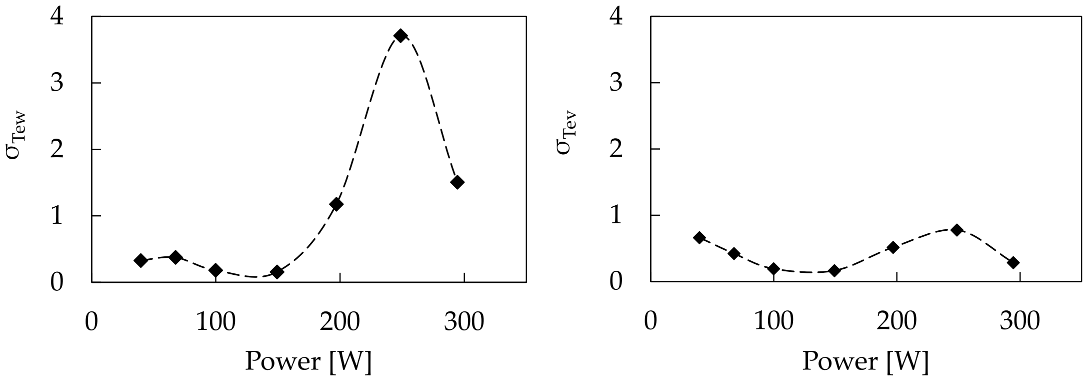

(a) (b)

Figure 3.4 - Temperature standard deviation of (a) evaporator wall and (b) evaporator vapour

For higher power levels in the range $Q > 150$ W the observed temperature fluctuations become more intense, as shown in Figure 3.4. The standard deviation increases sharply as the thermosyphon approaches failure. By monitoring the standard deviation of the operating temperature, it is thought that failure of thermosyphons in industrial applications could be recognised and possibly avoided.

The oscillatory behaviour of the thermosyphon in the range $150\text{ W} < Q < 325\text{ W}$ is emphasised in the evaporator wall temperature measurements, shown in Figure 3.5. The failure of the thermosyphon was observed at 325 W, designated as a rapid excursion of the evaporator wall temperature.

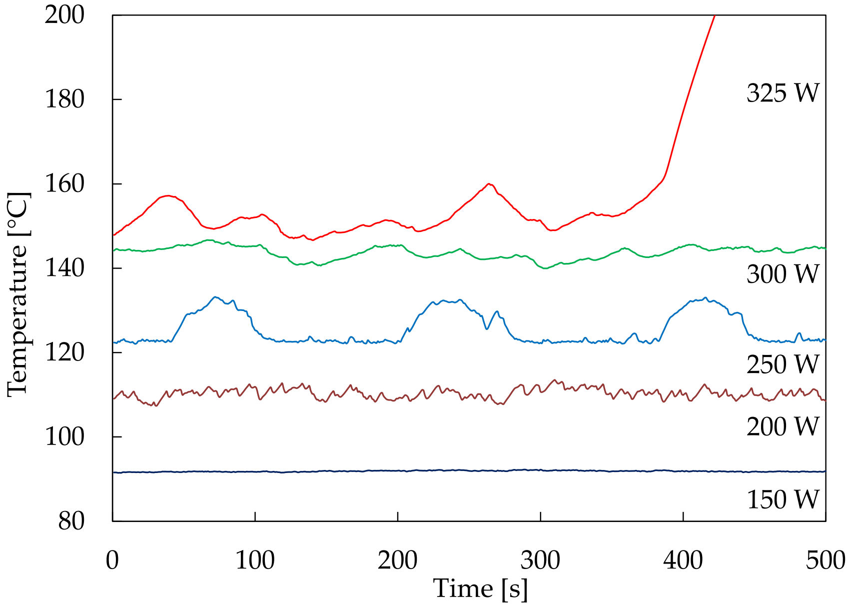

Figure 3.5 - Evaporator wall temperature distributions for higher power range

Of particular note in Figure 3.5 is unsteadiness of the evaporator wall temperature at higher power levels ($Q \geq 200$ W). The periodic fluctuation in the temperature at $Q = 250$ W indicates a flooding oscillation.

The temperature and pressure measurements in the evaporator and condenser during this event are shown in Figure 3.6. It is evident that an unsteady behaviour is occurring in the evaporator section, where the wall temperature shows a fluctuation of ~ 10 °C. This oscillatory regime corresponds to a peak standard deviation of the wall temperature, shown in Figure 3.4.

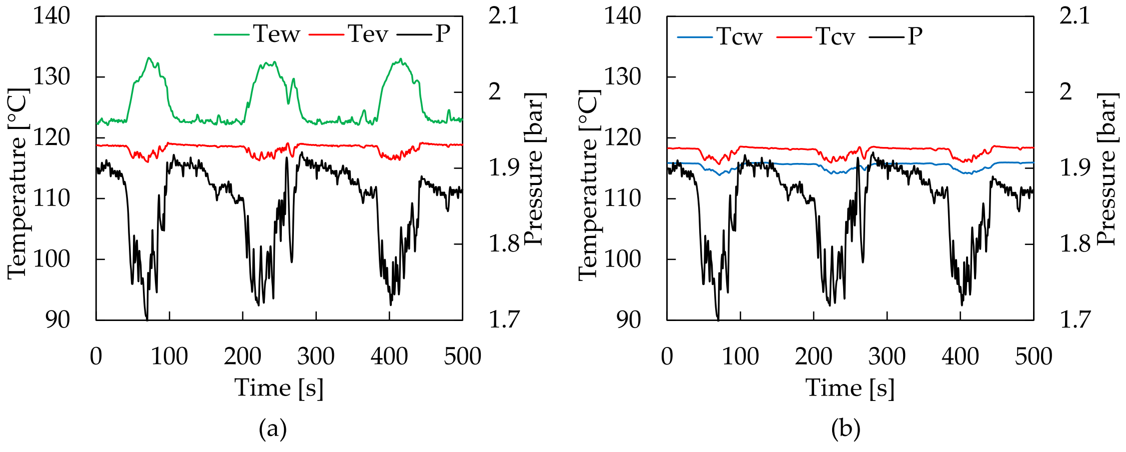

Figure 3.6 - Wall and vapour temperature and pressure in (a) the evaporator and (b) the condenser at Q = 250 W

Flooding oscillation is a temporary limitation, usually occurring at high heat inputs, where the vapour velocity is large enough to entrain liquid droplets into the vapour core which are subsequently carried to the condenser section. As a result, less liquid returns to the evaporator, and there is partial dryout in the evaporator. This causes a decrease in pressure, as there is less evaporation occurring. The vapour pressure decreases until there is no longer enough force to hold the liquid in the condenser section, at this point the liquid will fall back to the evaporator. This phenomenon was also observed by Lock [57].

At 300 W the thermosyphon begins to show signs of failure, as shown in Figure 3.7. There is a notable increase in the pressure measurement with substantial oscillations, from $P = 1.85$ bar at $Q = 250$ W, to $P = 2.93$ bar at $Q = 300$ W. Large fluctuations are observed in the evaporator wall temperature, also quantified by a rapid increase in the standard deviation in Figure 3.4, this indicates the imminent failure of the thermosyphon.

The temperature and pressure conditions at failure are illustrated in Figure 3.8, for $Q = 325$ W. At this power level, the velocity of the vapour flowing to the condenser is increased, causing the initial increase in pressure evident in Figure 3.8. This high velocity vapour results in entrainment of the condensate flowing back to the evaporator and unsteady evaporator wall temperatures are observed. Similar to flooding oscillation at 250 W, the liquid is held in the condenser section and the evaporator experiences dryout.

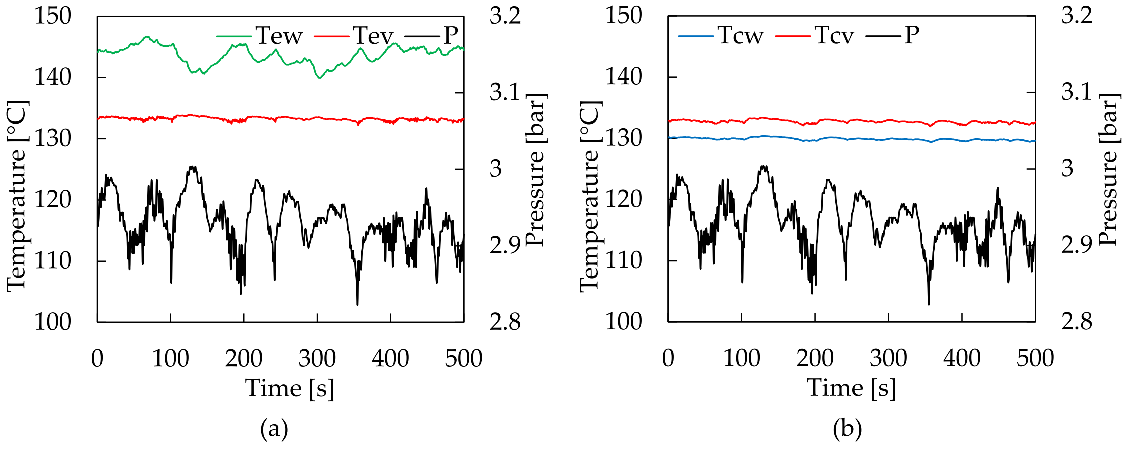

Figure 3.7 - Wall and vapour temperature and pressure in (a) the evaporator and (b) the condenser at Q = 300 W

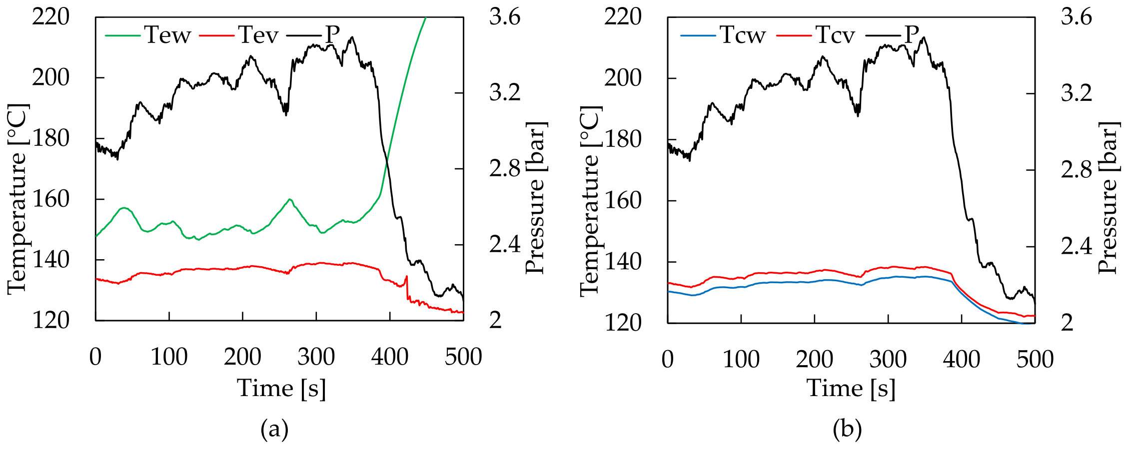

Figure 3.8 - Wall and vapour temperature and pressure in (a) the evaporator and (b) the condenser at Q = 325 W

With a reduced rate of evaporation, the pressure of the system drops and the condensate is free to return to the evaporator, as evident in Figure 3.8 at 400 s. At this high power level, the heat flux in the evaporator is such that rewetting of the wall is prevented and the evaporator wall temperature increases exponentially, observed at ~ 370 s in Figure 3.8. This limit is referred to as the boiling limit [5], beyond this point there is a rapid deterioration of the thermosyphon heat transfer.

Considering the condenser temperatures in Figure 3.8 (b), as the vapour condenses within this region, the system changes thermodynamic states, such that the saturation pressure and temperature drop. This is important as it offers a passive safety mechanism of the thermosyphon should this failure limit be reached in application. As the flow of liquid between the evaporator and condenser is restricted, the thermosyphon begins to act as two separate systems with respect to temperature. In the condenser, as more heat is removed by natural convection, the liquid is subcooled, and the pressure decreases.

The entrainment limit of thermosyphons has been investigated in previous work, detailed in Chapter 2. These studies show that the entrainment limit depends on the fill ratio of the working fluid, and orientation of the thermosyphon. The critical heat input, Q_{max}, for the onset of flooding as described by Faghri *et al.* [37], can be estimated using Eqn. (3.5). For this experiment, it can be seen that this prediction gives a conservative estimate of the failure power, as shown in Figure 3.9. The critical power input as predicted for a vapour temperature of 145 °C is 220 W.

$$Q_{max} = K h_{fg} A_i [g\sigma(\rho_l - \rho_v)]^{0.25} \times \left(\rho_v^{-0.25} + \rho_l^{-0.25}\right)^{-2}$$

Eqn. (3.5)

where

$$K = R' \, tanh^2(0.5Bo^{0.25}) \; ; \; (R' = 1)$$

Eqn. (3.6)

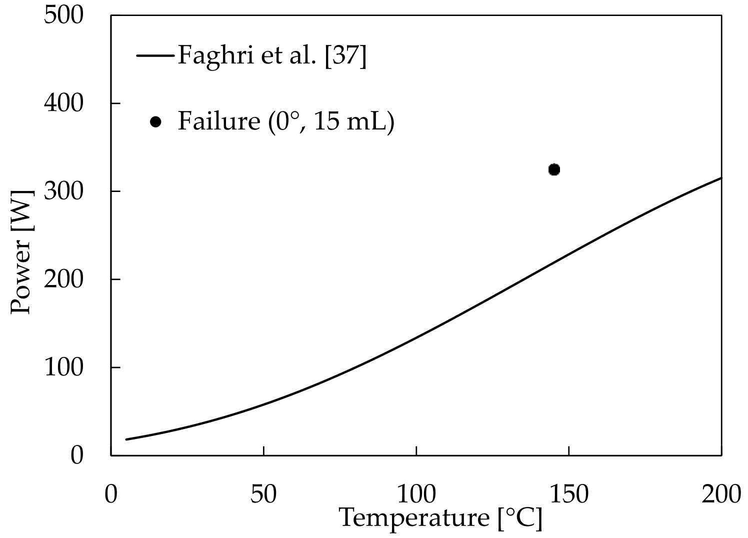

Figure 3.9 - Entrainment limit prediction using Faghri *et al.* correlation [37]

3.4.2. Effects of inclination angle and fluid loading

The thermal resistances of all thermosyphon tests were calculated using the formulae outlined in Section 3.3.2 (Eqn. (3.1), Eqn. (3.2) and Eqn. (3.3)). The total thermal resistances for each of the bend angles and fluid loadings are presented in Figure 3.10. As evident in Figure 3.10, there is generally little change in the overall thermal resistance as both the bend angle and fluid loading are varied. It is noted, however, that for the 90° bend case the thermal resistance increased as it approached failure, $R_{tot} = 0.09$ K/W at $Q = 270$ W, shown in Figure 3.10 (a). For the 0°, 30° and 60° there was very little change as the device approached failure, with $R_{tot} \approx 0.02$ K/W.

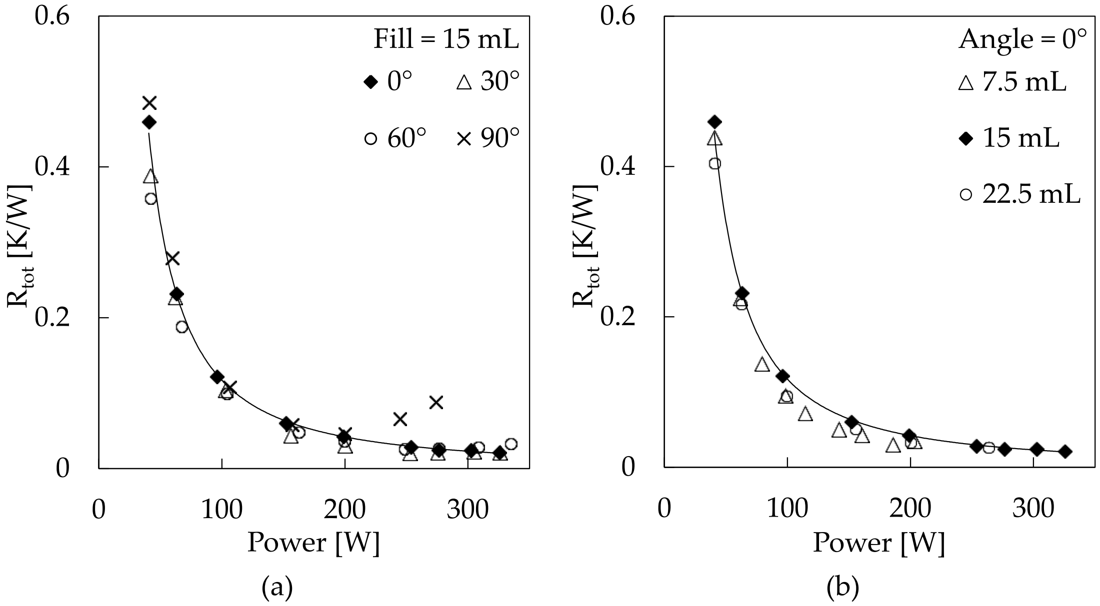

Figure 3.10 - (a) Total thermal resistance variation with bend angle and power ($V_f = 15$ mL) and (b) Variation of total thermal resistance with fluid loading (vertical orientation, 0°)

The evaporator and condenser thermal resistances will be discussed separately. It is worth noting here that the effective thermal resistance of the vapour core, based on the approximated pressure drop of the vapour flowing between the evaporator and the condenser, was estimated using the following relation, [3],

$$R_v = \frac{R_0 T_v^2 \Delta P_v}{P_v h_{fg} Q} \qquad \textbf{Eqn. (3.7)}$$

$$\Delta P_v = \frac{8\mu_v \dot{m}}{\rho_v \pi r_v^4}\left(\frac{L_e + L_c}{2} + L_a\right) \qquad \textbf{Eqn. (3.8)}$$

For example, for the low power case (Q = 40 W) the vapour core resistance is R_{vap} = 0.0003 K/W, and subsequently decreases with increasing power. Thus, the effective thermal resistance associated with the vapour core can be neglected for the range of parameters studied in this investigation.

Figure 3.11 shows the thermal resistance trend in the (a) evaporator and (b) condenser section with both increasing power and bend angle from 0° to 90°. For comparison purposes, the Imura pool boiling correlation [31] is included in Figure 3.11 (a). As discussed in Chapter 2, the Imura correlation is widely regarded as an accurate tool in predicting pool boiling regimes within thermosyphons, and is defined by Eqn. (3.9).

$$h_e = 0.32\left(\frac{\rho_l^{0.65} k_l^{0.3} C_{pl}^{0.7} g^{0.2}}{\rho_v^{0.25} h_{fg}^{0.4} \mu_l^{0.1}}\right)\left(\frac{P_v}{P_{atm}}\right)^{0.3} q^{0.4} \qquad \textbf{Eqn. (3.9)}$$

The performance of the condensation regimes in Figure 3.11 (b) are compared to both Nusselt's equation for falling film condensation, Eqn. (3.10), and the modification of this theory for thermosyphon applications, proposed by Hashimoto and Kaminaga [23], Eqn. (3.11).

$$h_{Nusselt} = 0.943\left\{\frac{\rho_l(\rho_l - \rho_v) g k_l^3 \left[h_{fg} + 0.68 C_{pl}(T_v - T_c)\right]}{\mu_l (T_v - T_c) L_c}\right\}^{0.25} \qquad \textbf{Eqn. (3.10)}$$

$$h_c = 0.85 Re_l^{0.1} \exp\left[-0.000067\left(\frac{\rho_l}{\rho_v}\right) - 0.6\right]\left\{0.943\left[\frac{\rho_l(\rho_l - \rho_v) g k_l^3 h_{fg}}{\mu_l (T_v - T_c) L_c}\right]^{0.25}\right\} \qquad \textbf{Eqn. (3.11)}$$

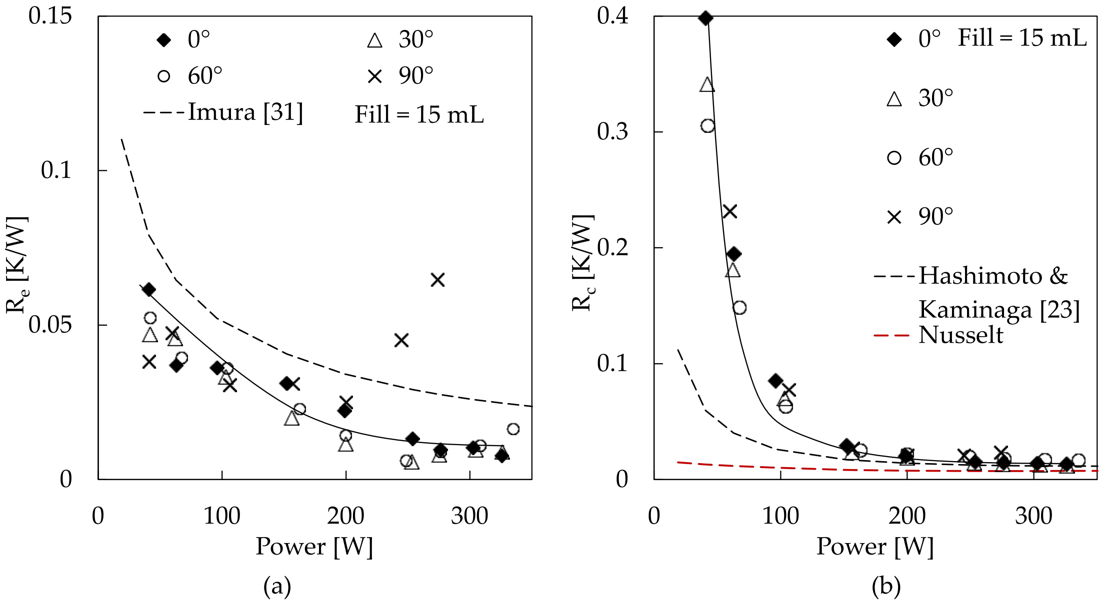

Figure 3.11 - (a) Evaporator thermal resistance and (b) condenser thermal resistance at various bend angles for V_f = 15 mL

Comparing the 0° bend angle to the curve for nucleate pool boiling in the evaporator section [31], shown in Figure 3.11 (a), it is evident there is a significant increase in the heat transfer performance moving from $Q = 40$ W to $Q = 60$ W, $R_e = 0.062$ K/W drops by 40 % to $R_e = 0.037$ K/W at $Q = 60$ W. As discussed previously, a geyser boiling phenomenon occurs in the evaporator, noted by oscillations in the wall and vapour temperatures (Figure 3.3). During the geyser boiling regime large plugs of liquid are forced upwards from the evaporator toward the condenser. The heat transfer under these conditions is thus a mixture of latent and sensible heat and is less effective than nucleate pool boiling. As result of this, there is a relatively higher thermal resistance in the evaporator compared with higher powers (70 W > Q > 150 W) where the mechanism of heat transfer is nucleate boiling.

At lower power levels, the geyser boiling regime defines how the heat energy is transported to the condenser section and thus the thermal resistance in the condenser section is dictated by the evaporator behaviour. Heat energy is transported to the condenser as vapour (latent) and heated liquid (sensible) as a result of the unsteady boiling behaviour in the evaporator section. It is clear in Figure 3.11 (b) that there is very poor heat transfer in the condenser section at low power levels due to the geyser boiling regime. It is also evident in Figure 3.11 (b) that the thermal resistances are larger than those predicted by Hashimoto and Kaminaga [23] during the geyser regime. This is direct evidence that the geyser phenomenon at low power results in heat transfer mechanisms that are different to those expected, such as falling film condensation, and that this regime is detrimental to the rate of heat transfer.

Without visualisation of the boiling and condensation occurring within the thermosyphon at low power, these mechanisms must be inferred from the thermal measurements. The changes in thermal resistance of both the evaporator and condenser combined with the time resolved measurements shown in Section 3.4.1 provide strong evidence that geyser boiling occurs at lower power. Also, this geyser regime has a significant influence on the entire thermosyphon performance, affecting the mechanisms of heat transfer in both the evaporator and condenser.

Figure 3.11 (a) shows a continual reduction in the thermal resistance of the evaporator section at moderate to high applied power levels in the evaporator, $70\ \mathrm{W} < Q < 200\ \mathrm{W}$. This drop in evaporator thermal resistance indicates a change in the mechanism of boiling. During this phase the measured thermal resistances are similar in trend and magnitude to that of the Imura correlation [31] (within 30 % agreement). This, coupled with the smooth evaporator wall temperature profile in Figure 3.5 and associated low standard deviation in Figure 3.4, indicates that the boiling regime in the evaporator has transitioned to that of nucleate pool boiling.

Higher heat transfer coefficients that improve with increasing the imposed heat input are consistent with nucleate boiling. It is well known that the increased vapour production enhances the heat transfer due to increased liquid agitation near the heated surface [58]. This is also evidenced by the reduction of both evaporator wall and vapour temperature fluctuations for $70\ \mathrm{W} < Q < 200\ \mathrm{W}$ shown in Figure 3.4 and Figure 3.5. The reduction in the amplitude of the wall temperature oscillation suggests that the mechanism has transitioned to more “traditional” thermosyphon behaviour, where the heat is transferred by up-flowing vapour and liquid condensate return. As the heat input is increased towards $Q = 200$ W, nucleate boiling becomes more rigorous, resulting in a further drop in thermal resistance in the evaporator section at higher power levels.

For the condenser at moderate to high power ($70 \text{ W} < Q < 200 \text{ W}$), there is a steep reduction in the thermal resistance, as seen in Figure 3.11 (b). This indicates that the thermosyphon is performing in a condensation phase change regime. It can also be seen in Figure 3.11 (b) that the condenser thermal resistance approaches the predicted condensation thermal resistances of Hashimoto and Kaminaga [23]. This correlation implies that film condensation is occurring within the condenser section over this range of input power, with some effects of entrainment due to the counter-current flow arrangement. Further increase of the power results in the thermal resistance of the condenser approaching a regime of falling film condensation as predicted by the Nusselt correlation, Figure 3.11 (b).

For the highest power tested, $200 \text{ W} < Q < 325 \text{ W}$, there is a notable plateau in the measured evaporator thermal resistance (Figure 3.11 (a)). This is consistent with the temperature fluctuations observed in Section 3.4.1. The flooding oscillation regime observed over this power range deteriorates the effective nucleate pool boiling heat transfer, and as a result the thermal resistance measurement starts to flatten.

For these high power levels, $200 \text{ W} < Q < 325 \text{ W}$, the evaporator oscillations have little effect on the condenser performance. The high mass flux of the vapour to the condenser at high powers ensures a dominant upward flow of vapour to the condenser. The thermal resistance shown in Figure 3.11 (b) approaches that of the Nusselt correlation at high power levels. This indicates that the mechanism of heat transfer in the condenser section is falling film condensation.

With regard to the thermal resistances in the evaporator for changing bend angles, Figure 3.11 (a) shows that the 30° and 60° case follow the same general trend as that described for the 0° case. It is evident however, that there is a slight reduction in the thermal resistance of the evaporator section at power levels below 100 W. Looking ahead to Figure 3.16 it is also evident that there are no significant oscillations in the evaporator temperature within this applied power range for the 30° and 60° bends. These results indicate that the effects of geyser boiling may be lessened with the installation of bends in the thermosyphon geometry. In the case of the 30° and 60° bend angles, there is improved separation of the liquid and vapour phases due to gravity in the evaporator, i.e. phase stratification. This may act to lessen the probability of liquid becoming trapped above a growing vapour bubble. The flow restriction imposed by the bend angle in the adiabatic section will further act to disturb the upward flowing fluid, breaking large vapour bubbles and liquid plugs that may be suspended by vapour. In this way less liquid is forced to the condenser section by the rising vapour, and the geyser regime is mitigated.

A different trend is observed for the case of 90° bend, shown in Figure 3.11 (a). For the lower power levels, the hydrostatic pressure acting on the liquid in the adiabatic section returning to the evaporator is sufficiently high to overcome the rising vapour inertia force, and thus refill the evaporator section. Therefore, the evaporator is cooled by the returning condensate and the boiling behaviour resembles that of the other bend angle cases. As the heat input is increased, $Q > 200$ W, the thermal resistance for the 90° bend increases to more than 300 % of the other angle test cases and exceeds that predicted by the Imura pool boiling correlation. This indicates that nucleate pool boiling is no longer occurring in the evaporator section. The sharp reduction in the heat transfer at this point suggests earlier onset on dryout for the 90° bend angle, where the lack of hydrostatic head in the adiabatic section prevents liquid returning to the evaporator. This restriction on the fluid is also compounded by higher vapour velocities flowing upward at these elevated power levels. For the 90° bend case, without the aid of gravity to counteract the inertia of the vapour, the returning liquid condensate is held out of the evaporator, either pooling in the bend of the adiabatic section, or becoming entrained into the vapour core flow. With diminishing condensate to wet the evaporator as the power is further increased, the mechanisms of heat transfer continually deteriorate. This results in a rise in the thermal resistance and associated increase in the wall temperature for these experimental conditions.

Figure 3.12 shows the changes in the thermal resistance with fill volume, from $V_f = 7.5$ mL – 22.5 mL, for the case of the 0° bend angle. Figure 3.12 (a) shows that there is very little change in the trend of the evaporator thermal resistance for $V_f = 15$ mL and $V_f = 22.5$ mL. This suggests that, at high fill volumes, the evaporator thermal resistance is less sensitive to fluid loading.

Also of interest in Figure 3.12 is the performance of the lowest fill volume case, which does not present evidence of geysering as described above. Looking at the evaporator thermal resistances in Figure 3.12 (a), there is a consistently lower measured thermal resistance for the case of $V_f = 7.5$ mL. Looking forward to Figure 3.16 it is also clear that there are no notable fluctuations in the evaporator wall temperature for the lowest fill volume. The lower thermal resistances and steady wall temperatures are evidence to suggest that nucleate boiling is occurring in the evaporator, even at the lower power inputs. This has important practical implications for low power applications, in that the thermal performance can be improved and geyser boiling avoided by simply considering the liquid fill volume.

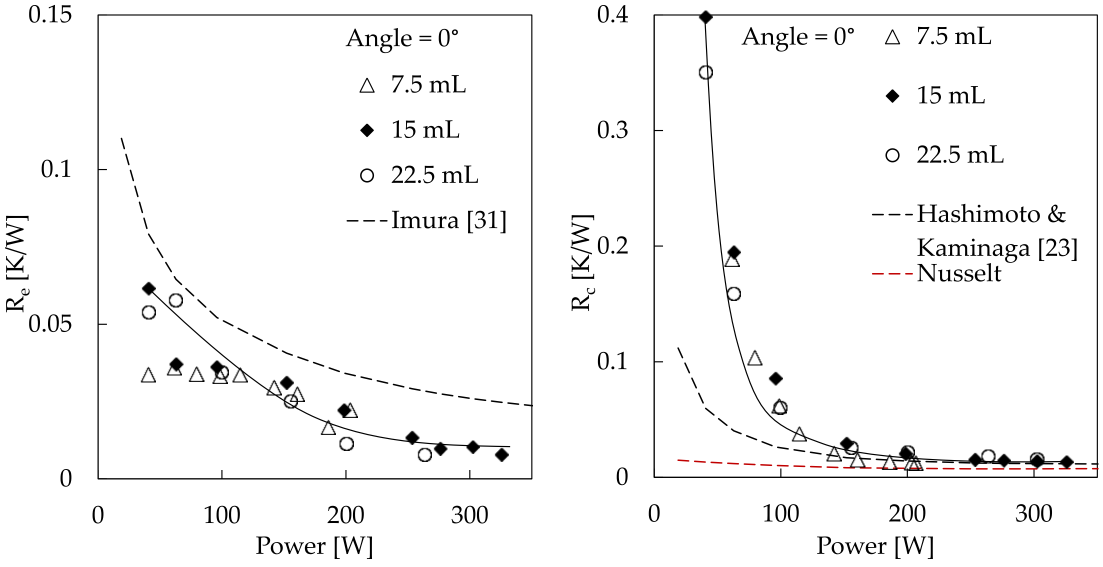

(a) (b)

Figure 3.12 - (a) Evaporator thermal resistance and (b) condenser thermal resistance at various fill ratios for 0°

For the condenser section, there is still a substantial thermal resistance evident at low fill volumes and power levels, shown in Figure 3.12 (b). This is due to the fact that, at lower fill volumes and lower powers, there is less liquid circulating through the thermosyphon and the vapour velocity is relatively low. It is possible that some of the vapour condenses along the adiabatic section and, as a result, the condenser is not active at low power and low fill volume. Once the power, and thus vapour velocity, is increased in Figure 3.12 (b) there is a substantial reduction in the condenser thermal resistance at low fill volumes. The measured thermal resistance is closer to that predicted using the Hashimoto and Kaminaga correlation [23], showing that the dominant mechanism of heat transfer is falling film condensation.

Figure 3.13 shows the component thermal resistances as a percentage of the total resistance for $V_f = 15$ mL and the corresponding values of the evaporator and condenser thermal resistances are shown in Table 3.3. The trends shown here are representative of all fill volumes tested. At lower power, $Q = 40$ W, the high condenser thermal resistance dominates as there is limited phase change heat transfer occurring and a geyser-type regime dominates. The mid power of $Q = 150$ W shows a balance between the evaporation and condensation thermal resistances, consistent with nucleate pool boiling and falling film condensation regimes outlined previously. At the higher power level of $Q = 250$ W there is again an increase in the relative proportion of the condenser thermal resistance over the range $0° < \theta < 60°$. This is due the observed flooding regime at this power level, leading to higher condenser thermal resistance compared to that of the evaporator. The higher proportion of the evaporator thermal resistance for the 90° bend is due to partial dryout in the evaporator, as discussed previously.

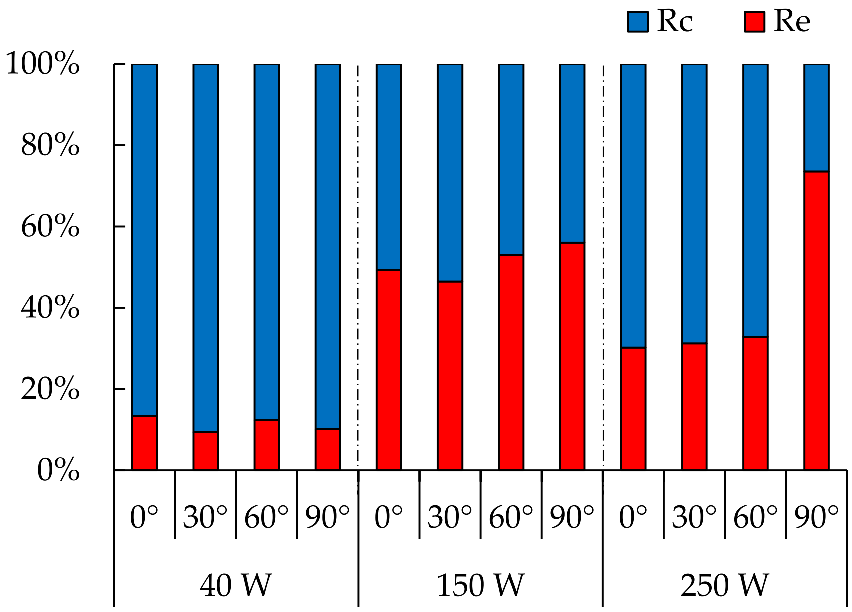

Figure 3.13 - Thermal resistances per thermosyphon section for each angle over a range of power settings (V_f = 15 mL)

	Power [W]	0°	30°	60°	90°
R_e	40	0.054	0.045	0.054	0.038
[K/W]	150	0.025	0.022	0.030	0.030
	250	0.008	0.008	0.010	0.068
R_c	40	0.351	0.432	0.382	0.340
[K/W]	150	0.026	0.026	0.026	0.024
	250	0.018	0.017	0.021	0.025

Table 3.3 - Evaporator and condenser thermal resistance values

3.4.3. Failure performance characteristics

The failure power of the thermosyphon as a function of fill volume for each of the bend angles tested was investigated, as it is crucial with regard to defining the operational limit of the thermosyphon. The failure point of each bend angle and fill volume was noted by large excursions in the evaporator wall temperature, coupled with a high degree of pressure fluctuation, as presented previously in Figure 3.8.

The behaviour of the thermosyphon at failure, in relation to the power level and thermal resistance, is highlighted in Figure 3.14. Considering the trend of failure power with fill loading for the 0° case, shown in Figure 3.14 (a), it is clear that there is an optimum fill loading in terms of achieving the maximum power performance, here observed as $V_f = 15$ mL. This result is consistent with the operational envelopes of thermosyphons described in the literature. As discussed in Section 3.2.3, an operational envelope in terms of the fill ratio and input power, was developed by El-Genk and Saber [38]. The boundaries of this envelope represent the dryout, flooding and entrainment limits of the two-phase closed thermosyphons.

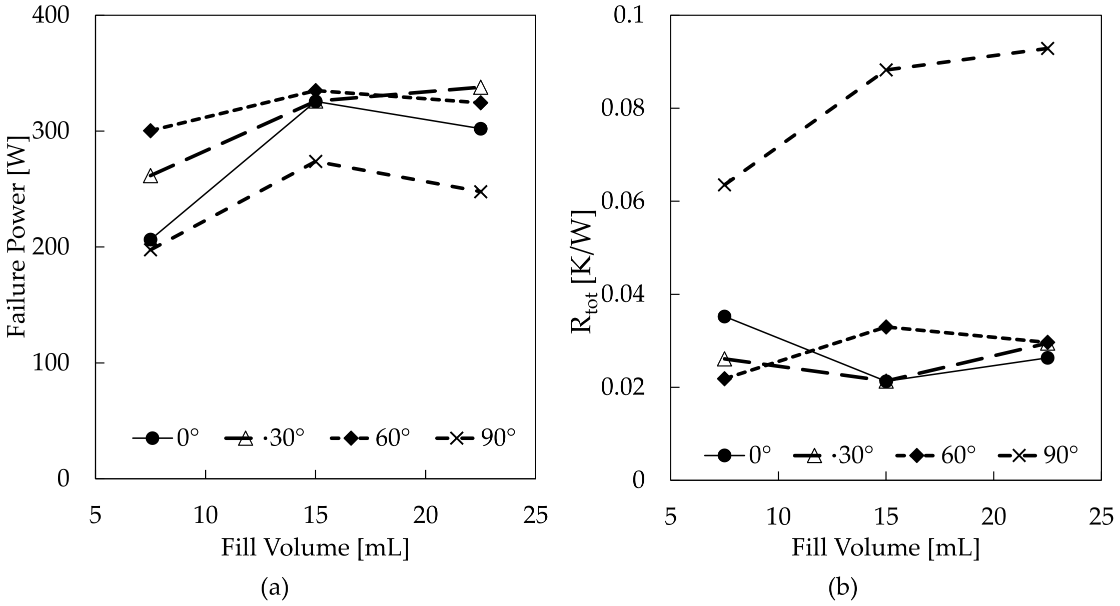

(a) (b)

Figure 3.14 - Failure power levels for varying fill volume and bend angle; total thermal resistance at failure for varying fill volume and bend angle

In Figure 3.14 (a) at the lowest fill ratio, $V_f = 7.5$ mL, and 0° bend angle, the failure power is 60 % lower than that of the mid fluid loading. In terms of the thermal resistances immediately prior to failure, Figure 3.14 (b) shows there is a higher thermal resistance evident for the 0° low fluid loading case. The low failure power and high thermal resistance of this experimental arrangement are due to insufficient fluid circulation through the thermosyphon. The limited volume of liquid flows down the sides of the evaporator under the influence of gravity, resulting in a thin film that may not span the entire evaporator length, as illustrated in Figure 3.15. At high power levels, the film evaporates rapidly and cannot provide adequate cooling to the heaters. The heat input reaches a maximum point where dryout of the evaporator occurs, there is significant increase in the evaporator wall temperature and the vapour circulates through the upper sections of the thermosyphon.

With increased fluid loading, Figure 3.14 indicates that the failure power increases for $V_f = 15$ mL. This represents a different failure mechanism occurring at higher fill volumes, where the thermosyphon reaches the counter-current flooding limit, as described by El-Genk and Saber [38]. For the $V_f = 15$ mL case, the dryout is a result of the high vapour production rates in the evaporator preventing the liquid from returning to this section, as opposed to that of the lower fluid loading where there was insufficient fluid circulating through the thermosyphon. The flooding limit is reached when the liquid is held up in the condenser section, which leads to a large excursion of the evaporator temperature and subsequent failure of the thermosyphon.

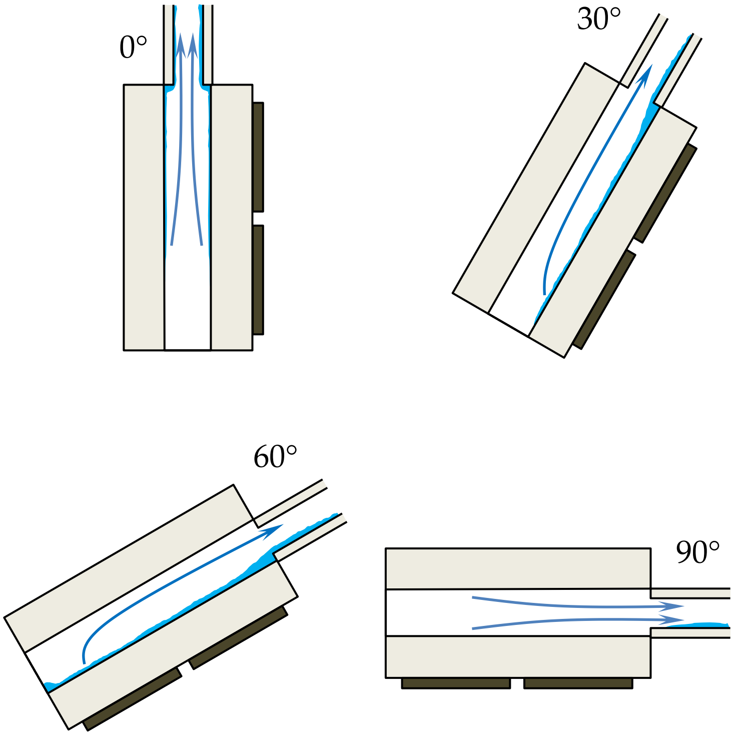

Figure 3.15 - Flow of liquid condensate for each bend angle case at failure

The mechanism of failure of the highest fill ratio at the 0° angle, shown in Figure 3.14, is most likely due to the boiling limitation for high fill volumes and high heat input, as outlined by Faghri [5]. At the higher power levels, the boiling in the evaporator becomes more vigorous. At the maximum heat input the bubbles begin to coalesce at the evaporator wall, generating a layer of vapour between the wall and liquid phase. The wall is insulated from the cooling liquid and the wall temperature of the evaporator section rises significantly, leading to failure of the thermosyphon.

The failure mechanisms for the 30° and 60° bend angles show the same trend as the 0° case for changing fill volumes, with the failure power increasing with increasing fill, as shown in Figure 3.14. However, a notable improvement in failure power is evident at the lower fill volume, $V_f = 7.5$ mL, for the 30° and 60° bend angles. It appears that at these higher bend angles the flow of returning condensate is directed in such a way that it can cool the heated surface more effectively, as illustrated in Figure 3.15. A bend in the evaporator results in a more stratified counter-current flow in the evaporator region, where the vapour rises to the top of the evaporator. The condensate is free to flow back to the evaporator section under the influence of gravity covering the heated surface more evenly and the evaporator wall is less susceptible to dryout with lower fill volume. Considering the standard deviation of the evaporator wall temperature, shown in Figure 3.16 (b) & (c), it is evident that, for the lower fill volumes, the thermosyphon is already operating in a transient regime with oscillatory behaviour. However, for the 30° and 60° bend angles, the thermosyphon is capable of sustaining pseudo-steady behaviour over a higher range of input power levels.

A higher bend angle (60°), Figure 3.15 and Figure 3.16 (c) show that there is further stratification of the flow while still maintaining the required hydrostatic head to force liquid return throughout the evaporator. It is likely that the bend angles result in a thicker liquid film in the evaporator section covering the heated wall, and the onset of dryout is delayed to higher power levels for lower fill volumes. Therefore, the improved failure power for the 30° and 60° bend angles is thought to be a combination of the liquid stratification at the bend enabling more liquid to enter the evaporator, and improved filling of this section due to the hydrostatic pressure gradient forcing the liquid downwards.

Finally, considering the case of the 90° bend, shown in Figure 3.14 the thermosyphon performance deteriorates. This is due to a combination of factors, resulting in premature dryout of the evaporator section. For the 90° bend, a larger hydrostatic head is required to overcome the increase in vapour inertia forces at higher power levels. Without the aid of hydrostatic forces, the liquid is prevented from entering the evaporator and most likely pools in the bend section, as illustrated in Figure 3.15. With no condensate return, the evaporator section quickly dries out and failure occurs.

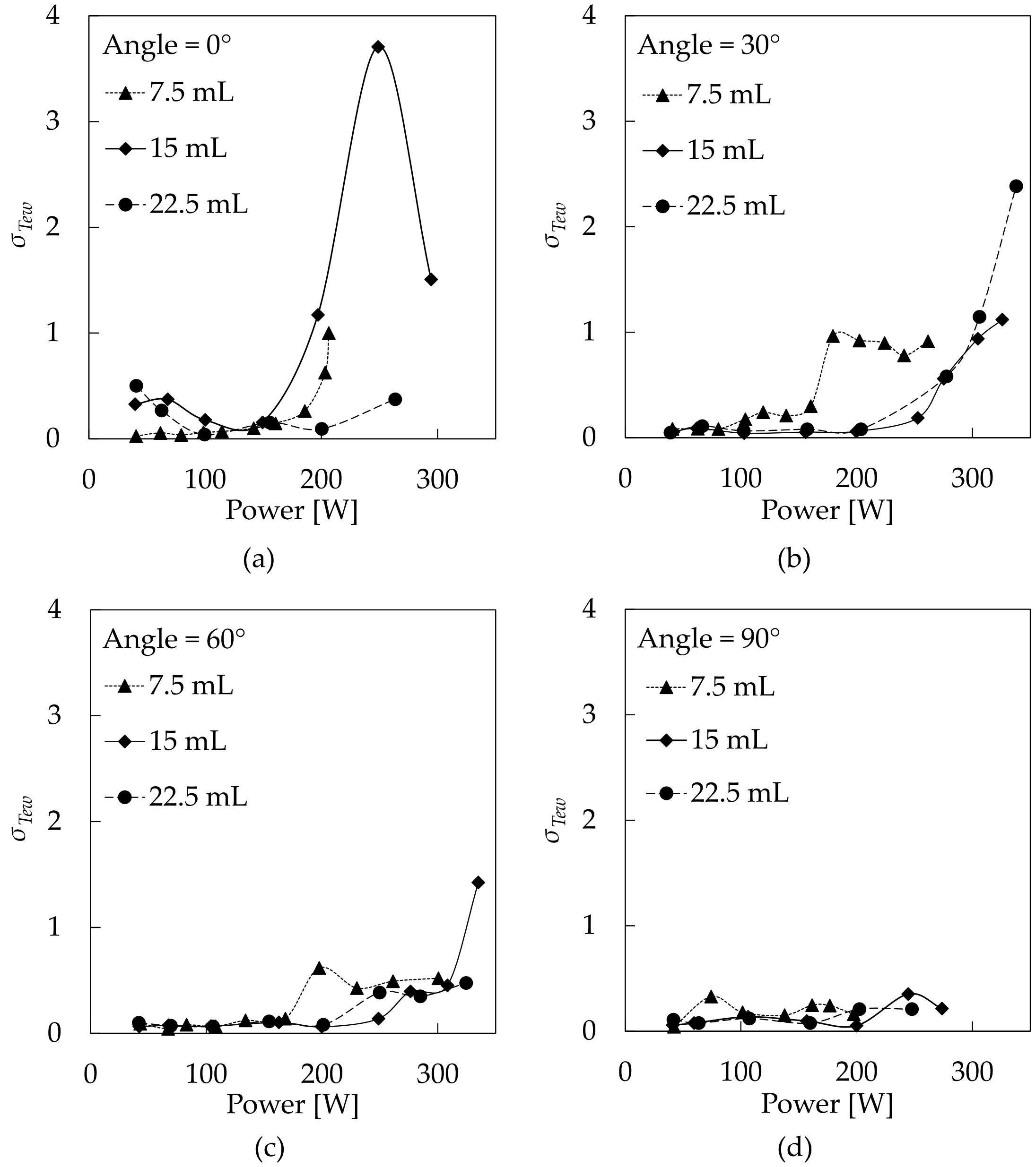

(a) (b) (c) (d)

Figure 3.16 - Evaporator wall temperature standard deviation with fill ratio (all bend angles)

The onset of failure is also indicated by an increase in the standard deviation of the temperature. Figure 3.16 shows the standard deviation of evaporator wall temperature for each bend angle over the experimental range of fill volumes. For the 0° bend, there are fluctuations evident at low power ($Q < 100$ W) and high fill volumes, $V_f = 15$ & 22.5 mL, shown in Figure 3.16 (a). These fluctuations are due to geyser boiling, and are not associated with thermosyphon failure. The focus in this section is on the regions where severe temperature oscillations occur at high power levels, which are indicative of the dryout events in the evaporator leading to the failure of the thermosyphon.

These results suggest promising practical implications for the 30° and 60° bend angles cases. The results indicate that the sensitivity of the thermosyphon to fill volumes can be mitigated with bends in the adiabatic section, due to the flow stratification in the evaporator. This prolongs the operation of the thermosyphon to higher power levels, which is beneficial in some cooling applications.

3.4.4. Outlook for passively cooling of electronics

Figure 3.17 shows the thermal resistances across the various sections of the experimental apparatus at increasing levels of heat input, $Q = 60$, 150 & 300 W. The resistances shown in this figure are: from the heaters to the evaporator section, R_{TIM}, across the length of the thermosyphon, R_{tot}, and across the natural convection heat sink to ambient air, $R_{c\text{-}a}$.

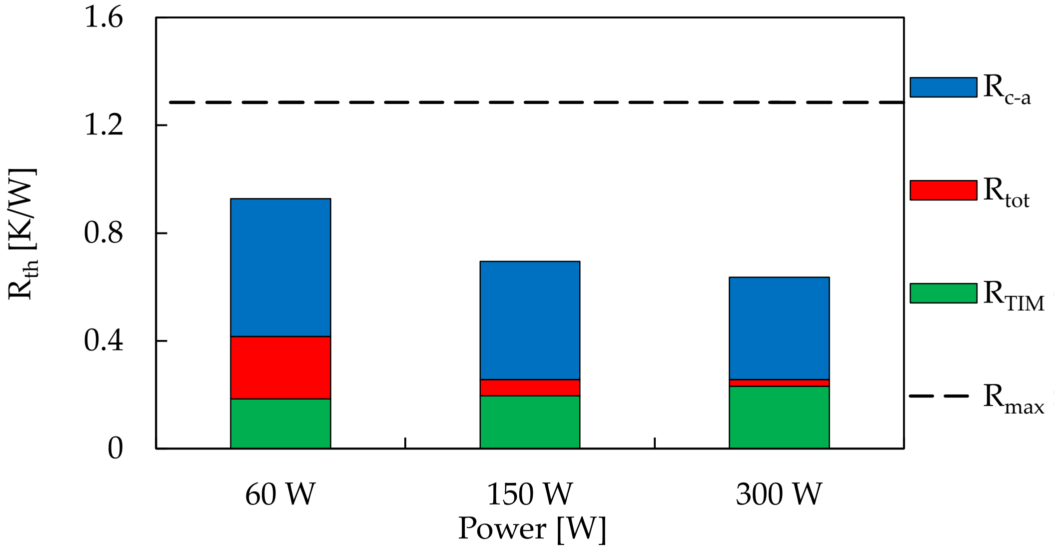

Figure 3.17 - Thermal resistances across the entire system ($V_f = 15$ mL; 0° bend)

It is clear from this Figure 3.17 that the thermal resistance of the thermosyphon, R_{tot}, reduces significantly with increasing power, showing a ~ 75 % reduction from Q = 60 W to Q = 150 W. As discussed previously, this is an indication that the evaporator is within the nucleate pool boiling regime and heat transfer is enhanced. It is also evident that the thermosyphon represents only a small percentage of the thermal network, from the heaters to ambient air, R_{tot} contributes 4 % at Q = 300 W. This confirms that the thermosyphon is the path of lowest resistance to dissipate the heat generated by the heaters. The largest thermal resistance of the system is that of the natural convection heat sink which consumes over half the thermal resistance budget.

Figure 3.17 highlights the reducing trend of the total thermal resistance across the entire system, from R_{th} = 0.9 K/W at Q = 60 W, to R_{th} = 0.6 K/W at Q = 300 W. Even as the device approaches failure at Q = 300 W, there is no significant increase in the thermal resistance, which is 50 % lower than the maximum operating thermal resistance of the power amplifiers. The threshold temperature for the radio frequency power amplifiers is 200 °C with a typical combined maximum power of 140 W (R_{max} ~ 1.3 K/W). The natural convection cooled thermosyphon system offers acceptable cooling capabilities compared with conventional heat sink cooling techniques. This has positive implications with regard to device performance and reliability. Additionally, the failure limit power of 325 W is greater than a factor of safety of 2 above that of the threshold operation limit of the RFPA, which is promising in the context of the target application. However, the unsteadiness associated with the geysering phenomena would require special consideration due to pressure pulsations possibly causing fatigue-type failure of the thermosyphon wall.

3.5. Conclusion

The results presented in this chapter highlight the need for further investigation with visualisation of the mechanisms affecting the operation of small dimension thermosyphons, in both the vertical and bent orientation. The main findings of this chapter are itemised as follows:

- Geyser boiling is present for higher fill volumes in the vertical thermosyphon orientation which can negatively affect the heat transfer performance of the thermosyphon, particularly at low power conditions.

- The geyser regime can be avoided with lower fill volumes. However, low fill volumes were also found to fail at lower power levels, due to insufficient fluid circulating through the thermosyphon.

- It was found that the failure of the thermosyphon at low fill volumes could be delayed with the bend angles of 30° and 60°, where the bend acted to direct the liquid condensate, under the influence of gravity, to more effectively cover and cool the heater surface.

- The 30° and 60° bend angles showed less sensitivity to fill volume, operating in a steady manner across all fill volumes, suggesting that these bends also mitigated the oscillations associated with geyser boiling.

- The bend angles of 30° and 60° presented improvements in the thermosyphon performance in terms of lower thermal resistance, higher power to failure and more steady operation at low powers. For the case of this study, the 60° bend angle showed the best performance in terms of both thermal resistance and failure power. The results also suggest that there is an optimum bend angle and fill volume at which the thermal performance is maximised.

- For the case of the 90° bend, the heat transfer was deteriorated, with higher thermal resistances and failure at lower power levels.

- Relatively, the thermal resistance of the thermosyphon is a small percentage (~ 4 %) compared to the natural convection heat sink and thermal interface of the heaters at high powers. Thus, the thermosyphon is effectively a thermal shunt between the heaters and the ambient conditions.

Importantly, in terms of the objectives of this study, it was found that the naturally aspirated thermosyphon was capable of adequately cooling the heat source application under investigation and the installation of bend angles in the thermosyphon geometry did not pose any limitations to the heat transfer capabilities of the device. For steady thermal performance during operation it would be beneficial to avoid the oscillatory behaviour encountered at high fill volumes in the vertical thermosyphon orientation. The forces driving the oscillatory behaviour of the thermosyphon require further investigation and this will be considered in the following chapter.

4. Flow regimes and heat transfer study

4.1. Introduction

The objective of this study was to identify and understand the oscillatory behaviour observed with certain thermosyphon operating conditions. Oscillations in temperature and pressure have been observed in the previous tests, outlined in Chapter 3, and unless properly understood and avoided, this phenomenon could lead to damage of the thermosyphon. In order to achieve this objective, a transparent thermosyphon test section was constructed, of similar dimension to the thermosyphon of the previous chapter. Within small dimension thermosyphons the two-phase flow regimes and associated heat transfer are dictated by the confinement of flow and interactions between the channel and the fluid.

To investigate the effects of confinement with changing thermophysical properties a parameter study was carried out using three different fluids: water, ethanol and engineered fluid HFE-7000 from 3M. In this way the parameters influencing particular flow regimes can be determined and understood.

4.2. Literature review

4.2.1. Analysis of flow regimes – Influence of flow regimes on heat transfer

Flow regimes aid in the description of the interfacial interactions associated with two-phase flow. These interactions are complex as they are influenced by a wide range of parameters associated with two-phase flow. A combination of fluid thermophysical properties and experimental operating conditions will define the type of flow to be expected. Experimental conditions such as channel shape, size, orientation, flow direction and velocity, saturation conditions, and heating conditions will affect two-phase flow. Fluid properties, in particular surface tension, viscosity, density and contact angle, will have varying degrees of influence depending on the defined experimental conditions.

Analysis of flow regimes in the context of heat transfer analysis is important, and often neglected in historical thermosyphon research. For boiling and condensation, heat transfer coefficients in two-phase flow and the flow patterns are intrinsically linked. Prediction of flow patterns can improve models for the prediction of heat transfer coefficients. Similarly, the effects of heat transfer coefficients on flow patterns need to be understood to predict flow regime transitions. Heat transfer analysis and flow regime characterisation are complementary; understanding trends and transitions in one area can help to explain those in the other.

Extensive work has been done in the area of characterising and predicting flow regimes for a range of different fluids and conditions. For convective boiling and condensation, the main experimental conditions used in flow regime classification are adiabatic or diabatic (flow boiling and condensation studies), horizontal, vertical or inclined channel orientation and direction of flow (co-current, counter-current, upward or downward).

Cheng *et al.* [59] provides a comprehensive review of the advances of flow regime analysis in recent decades. This source also highlights the areas of flow recognition, classification and mapping that need attention in future research. The following section will summarise studies described in [59] of particular relevance to this research. It should be noted, however, that in general, the following flow regime descriptions pertain to co-current flow boiling conditions, unless otherwise stated.

Flow pattern maps have been developed as prediction tools for flow patterns and transition regions where the flow regime is expected to change form. These maps generally relate the liquid and gas phases using certain flow parameters which act as a coordinate system. The choice of parameters generally varies between investigators. The commonly used coordinate systems are generally related to the velocity, mass flux, or momentum flux of each phase. In some cases, dimensionless numbers are used, such as *Re*, *We*, *Bo*, and *Fr*, which take account of the properties of the liquid and vapour phases.

Flow pattern maps proposed in the literature are of two types, empirical and theoretical. Empirical maps are based on the observations of particular experimental conditions and are widely used. The transitions of flow regimes are based on visual analysis and comparison with earlier studies. Theoretical models use analytical expressions to predict the flow regimes and transitions of two-phase flow based on the fluid (and heat transfer) characteristics.

For flow boiling in vertical channels, the flow regimes as observed in previous experiments are illustrated in Figure 4.1. Descriptions of these flow regimes are given in Collier [20] and Cheng [59]. Figure 4.1 also highlights the mechanisms of heat transfer associated with each type of flow. Though this figure outlines the observed trends in flow regimes and heat transfer, theoretical models to predict the onset of flow pattern transitions are yet to be developed. Therefore, flow pattern maps to predict the transitions regions for vertical heated flow are not present in the existing literature.

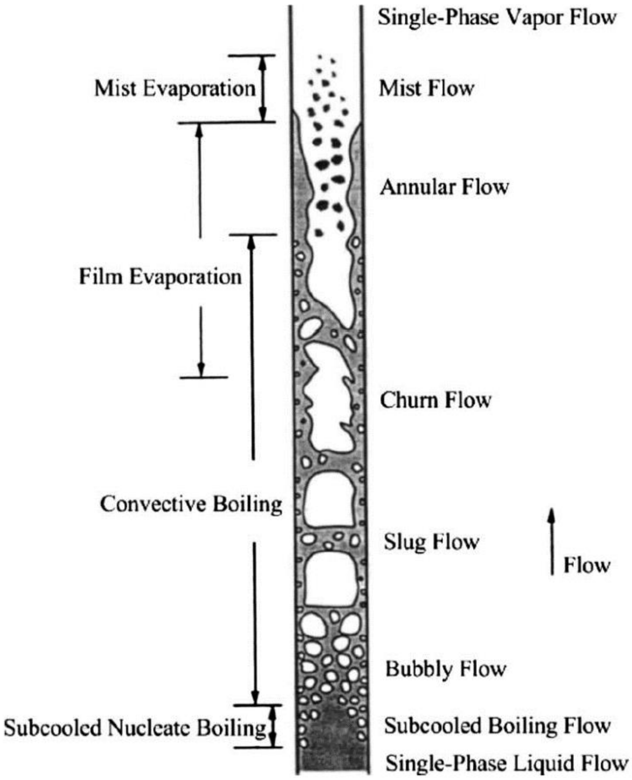

Figure 4.1 - Flow regimes for boiling in vertical tubes, source: [59]

One of the most established empirical flow maps for vertical adiabatic channels is that of Hewitt and Roberts [60]. This map was developed using experimental observation and momentum flux is used to relate the liquid and vapour transitions. Taitel *et al.* [61] developed a theoretical adiabatic flow map for vertical tubes. The conditions for flow regime transitions are characterised using analytical arguments based on physical mechanisms of two-phase flow. Therefore, the predictions of flow transition account for the influence of channel size and fluid properties. The proposed flow patterns in this map describe bubble, slug, churn, and dispersed annular flow.

Flow pattern maps for heated channels are not as well described in the literature. One of the first diabatic flow pattern maps was developed by Kattan *et al.* [62] for horizontal flow boiling of refrigerant fluids. This map was developed using experimental observations of the flow in conjunction with thermal data. Using this information, new heat transfer prediction models linked to the flow regimes were produced. The investigation has been the catalyst for many further studies, however predictive models for flow regimes in heated vertical channels are yet to be developed.

4.2.2. Summary

The existing literature presented in this section, combined with that of Chapter 2, point to a lack of recent flow visualisation of thermosyphons, especially across the entire length from evaporator to condenser. Consequently, there is also some misconception on the flow regime occurring within a thermosyphon, and how these flow regimes contribute to the overall heat transfer of the thermosyphon. With this is mind there is a need to progress the current knowledge toward development of diabatic flow pattern maps for vertical orientation.

The focus of this work will be to investigate the mechanisms of boiling both with and without confinement. The performance of a fully transparent thermosyphon will be analysed in terms of both the observed flow regimes and the measured heat transfer coefficients.

4.3. Methodology

4.3.1. Experimental design

The objective of these experiments was to fully visualise the two-phase flow patterns along the entire length of the thermosyphon. This was achieved by designing and fabricating a completely transparent thermosyphon and test apparatus which provided transparent heated and cooling sections without any flow restrictions.

The experimental set-up for the tests carried out in this investigation is shown in Figure 4.2. The main body of the thermosyphon consists of a length of sapphire tube, 500 mm in length, with 8 mm inner diameter and 1 mm wall thickness (10 mm outer diameter). Sapphire was used for the test section because it has a thermal conductivity commensurate of metals ($k \approx 40$ W/mK) and is transparent to light in the visible spectrum (~ 80 %). The high thermal conductivity of sapphire is desirable, compared to other transparent low conductivity materials such as glass, because it: (i) mitigates large temperature differences across the tube wall, (ii) responds quickly to dynamic changes within the thermosyphon and (iii) offers a low enough thermal resistivity that heat can be extracted from a water cooled condenser of practical length. The evaporator section was 100 mm long, and the condenser section was 200 mm in length. These sections were separated by a 180 mm adiabatic length.

The outer surface of sapphire tube was coated with electrically conductive (10 Ω/m^2) and visually transparent Indium Tin Oxide (ITO). The 100 mm evaporator section was ohmically heated by an Elektro-Automatik (8360-10T) D.C. power supply which imposed a voltage differential across, and subsequent current flow through, the ITO coating. The electrical connection to the tube surface was through metal leads, tightly fixed to the surface of the sapphire tube at the desired spacing. The thickness and electrical resistivity of the coating was such that an adequate level of uniform heating could be achieved in the evaporator section, while still allowing full internal visualisation of the thermosyphon test section.

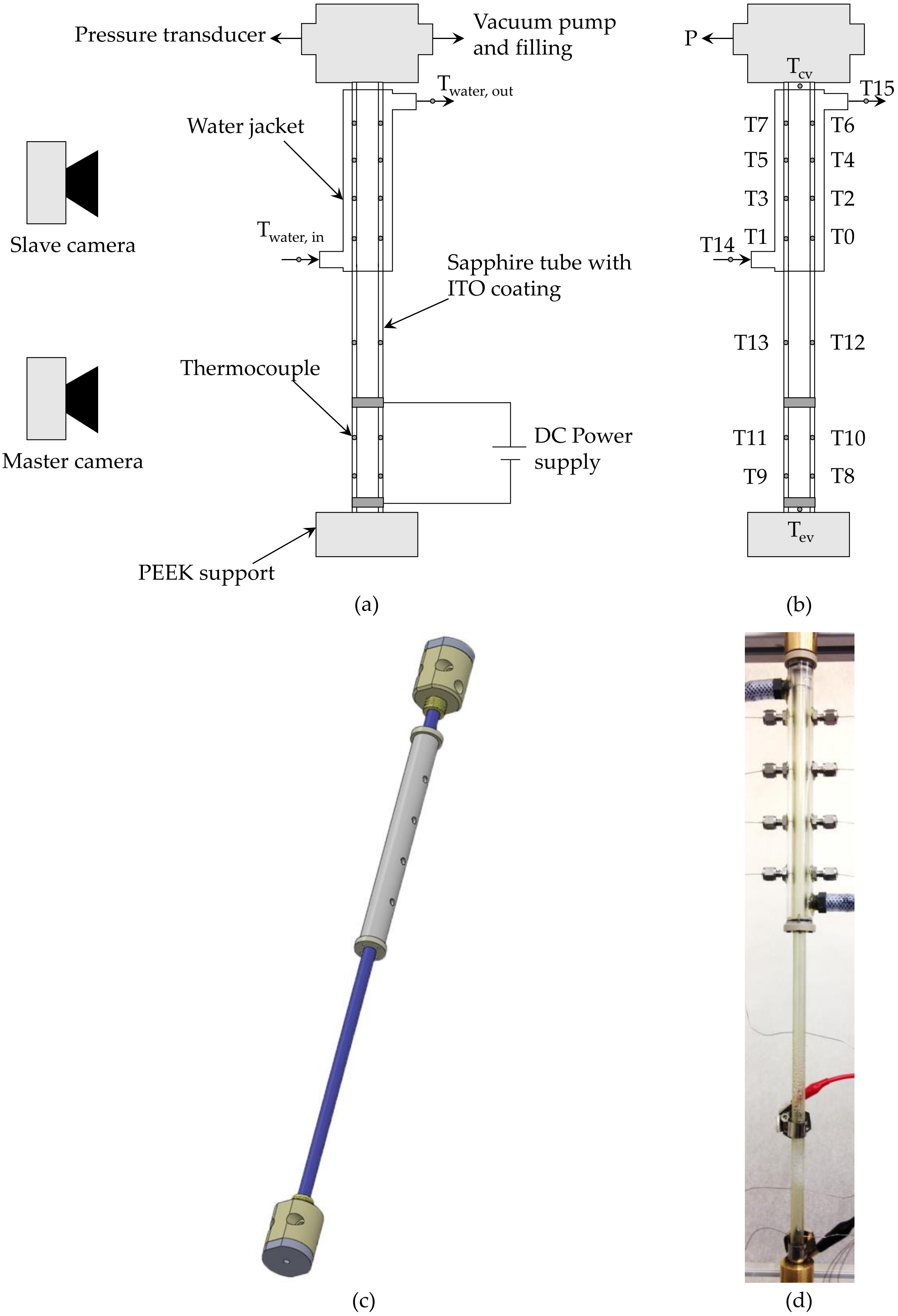

Figure 4.2 - (a) Schematic of apparatus; (b) Instrumentation of test section; (c) 3D rendering of thermosyphon; (d) Photographic image of thermosyphon

Cooling was achieved in the 200 mm condenser section using an annular, transparent polycarbonate water jacket. The condenser water jacket was connected to a Julabo A40 chiller unit through which the condenser water temperature could be controlled and set. A sufficiently high cooling water flow rate ensured a low enough water-side thermal resistance such that the condenser wall temperature was maintained close to that of the cooling water. This, coupled with the small temperature drop across the tube wall (max. 1 °C), facilitated the use of the chiller set point temperature as the control for the nominal thermodynamic state of the working fluid within the thermosyphon during operation. Thermocouples were positioned in the inlet and outlet of the condenser jacket to verify small temperature drops across the condenser section.

In order to seal the entire system, supporting end caps were manufactured from PEEK (Figure 4.2). The function of these end caps was twofold: they allowed for the thermosyphon to be affixed to a supporting aluminium profile frame and provided screw fittings to seal the sapphire tube in order for a vacuum tight seal. The screw fittings were manufactured from brass and allowed for two nitrile O-rings to ensure an air tight seal. Plumbing of the pressure transducer, filling line and vacuum line was with 1/8″ stainless steel tubing and Swagelok pipe fittings. All materials were chosen as they were chemically and thermally sound for use with all working fluids under investigation. Once sealed the thermosyphon was vacuumed to 0.01 bar before testing.

The thermosyphon itself was instrumented with 14 thermocouples inserted into the external tube wall, as shown in Figure 4.2. Two thermocouples were installed inside the tube (T_{ev} and T_{cv} in Figure 4.2), and a pressure transducer was used to measure the internal pressure of the system.

4.3.2. Instrumentation

To measure the temperature in each of the sections of the thermosyphon and to ensure an accurate reading of the wall temperatures, 0.5 mm diameter holes were drilled into the tube wall to a depth of 0.5 mm (half the depth of the tube wall) and the thermocouples were potted in the holes with thermally conductive paste. The positions of the thermocouples along the wall are shown in Figure 4.2. Two thermocouples were inserted inside the thermosyphon through compression fittings, positioned in the condenser vapour and evaporator liquid pool, T_{ev} and T_{cv} as shown in Figure 4.2.

Prior to testing, all thermocouples were calibrated in the same oil bath against an RTD probe to within 0.5 °C. The 14 thermocouples in the tube wall were T-type, Omega 0.5 mm stainless steel sheathed thermocouples. The use of small diameter thermocouples ensured the fastest response time to temperature changes across the tube wall. Two K-type thermocouple probes, each 1.5 mm in diameter, were positioned internally. These thermocouples were chosen for compatibility with compression fittings as a tight seal needed to be maintained in order to vacuum the system. An Omegadyne PX01C1-050A5T pressure transducer was plumbed into the system, located above the condenser section. This transducer had been calibrated by the manufacturer prior to use.

High-speed cameras were used to provide images of the full length of the test section. The cameras used were NAC Hi-Dcam II and operated using associated NAC software. An external trigger was used to initiate image recording in order to have the images from both cameras synchronised, and also synchronise the temperature and pressure measurements to the images. The high-speed images were captured at a rate of 1000 frames per second (fps), with a 1/1000 exposure time. A 50 mm Nikon lens was used with each camera so that the focal length was such that the whole test section could be viewed across the two cameras, one focused on the evaporator section and one on the condenser. A CMOS control gate was also built between the NI output voltage DAQ and the camera PCI board to ensure that the camera board would not be damaged by high input voltages.

The high-speed images were processed using editing software, ImageMagick (V 6.8.9), where they could be cropped and the separate evaporator and condenser images were paired and stitched together into one image. All images were compiled into video files using FFMPEG.

All pressure and temperature measurements were recorded using National Instruments DAQ systems and controlled using LabView. Thermocouples were wired to a 16-channel NI 9213 DAQ and pressure was measured using a voltage input NI 9201 DAQ. A NI 9263 module was used to output a 5 V signal to trigger the camera system when required. All DAQ modules were connected to a laboratory PC using a 4 module chassis (CDAQ 9174). As the thermocouple DAQ contained 16 thermocouples, the maximum sampling rate for this module, per thermocouple, was 50 samples per second. For the case of the pressure measurements, the voltage DAQ allowed a maximum sampling rate of 1000 samples/second.

A LabView interface was designed to read in the signals from the DAQ modules. This programme was designed to record data at separate sampling rates, depending on the test type. For longer steady state tests (~ 20 minutes) data was captured at the maximum rate for both temperature and pressure and averaged over 1 second. The average value for each thermocouple and pressure was then saved to an output text file every second. For high-speed data recording, a loop was programmed in LabView. This loop sent a 5 V signal to the Camera PCI board on a separate computer, and also triggered a high-speed data recording loop. The high-speed recording loop saved temperature and pressure values at the maximum sampling rate. This meant that for every image there was a pressure measurement and there was one temperature reading for every 20 images.

4.3.3. Working fluids

Deionised water, ethanol and HFE-7000 were employed as the working fluids as part of this study. The fill volume of the thermosyphon is defined as the volume of working fluid relative to the volume of the evaporator section. The fluid fill volume for the tests of this study was such that the evaporator was full (100 %) or half full (50 %), where the total volume of the evaporator was 5 x10^{-6} m^3 (5 mL).

The working fluid were chosen based on a characteristic bubble length scale in order to investigate the influence of bubble size and tube diameter on boiling dynamics, which were discussed in the Chapter 2. All fluids chosen were also transparent to allow for better visualisation of the fluid dynamics. The fluids used were non-toxic, and commercially available. HFE-7000 was also chosen due to its dielectric properties, which could be utilised in further electrohydrodynamic (EHD) testing of the thermosyphon. Table 4.1 summarises the thermodynamic properties of the fluid used at atmospheric pressure. The Figure of Merit, *FOM*, is a performance indicator for working fluids in thermosyphons, described in [3], given as Eqn. (4.1).

$$FOM = \left(\frac{h_{fg} k_l^3 \rho_l^2}{\mu_l}\right)^{\frac{1}{4}} \quad \textbf{Eqn. (4.1)}$$

As can be seen from the table, water has a much higher *FOM*, mostly due to the high liquid thermal conductivity. Water is commonly chosen as a working fluid, along with having a high *FOM*, it is a cheap, non-toxic and readily available. Refrigerants, however, are becoming a more attractive working fluid for electronics cooling applications. In general, they will have low values of λ_c, resulting in more stable performance at small dimension. Lower boiling and freezing temperatures also allow the thermosyphon to operate in wider temperature ranges and below 0 °C.

	T_{sat} [°C]	ρ_l [kg/m³]	ρ_v [kg/m³]	σ [mN/m]	μ_l [mNs/m]	h_{fg} [kJ/kg]	*FOM*
Water	100	958	0.6	59	0.28	2257	6925
Ethanol	78	757	1.4	17.3	0.4	960	1574
HFE-7000	34	1386	8.2	12.4	0.4	132	703

Table 4.1 - Thermophysical properties of working fluids at atmospheric pressure (1.01 bar)

4.3.4. Testing methodology

Before testing, the entire system was evacuated to 0.01 bar for about 30 minutes to ensure the removal of non-condensable gases (NCG). If NCGs are present they can collect in the upper condenser section, and prevent condensation in this region, therefore affecting the condensation heat transfer in this region. Once vacuumed the thermosyphon was then filled with the required working fluid, water, ethanol or HFE-7000, until the evaporator was either full or half full.

Testing consisted of maintaining a constant nominal sub-atmospheric internal pressure while varying the heat flux at the evaporator. The internal operating pressure was controlled by adjusting the temperature of the condenser section using the precision chiller and cold water loop such that decreasing the cold side temperature reduced the saturation pressure of the system.

The heat flux was increased in 10 W increments, and the system was left for a settling period of time, allowing a steady-state to be reached. Once the system was steady, temperature and pressure recordings were taken, and high-speed data and images were taken at the end of each tests setting. The heat flux was increased incrementally until dryout was present in the evaporator, noted by sharp increases in the evaporator temperatures and visually by observing no liquid film present in the evaporator. The maximum heat flux reached varied across each of the fluids, and depending on the fill volume under test. Table 4.2 shows a matrix of the tests carried out.

Working Fluid	P_r	**Fill ratio [%]**	**Heat flux [kW/m^2]**
Water	0.0002 – 0.006	50 – 100	7.5 – 63
Ethanol	0.001 – 0.006 – 0.02	50 – 100	7 – 46
HFE-7000	0.02 – 0.04	50 – 100	7 – 21

Table 4.2 - Test parameter matrix for transparent thermosyphon.

4.3.5. Data reduction

The analysis of the performance of the thermosyphon in terms of the heat transfer coefficient was carried out. In order to calculate the heat transfer coefficient, a measure of the electrical power to the evaporator section was measured. The input heat applied to the heated section, Q_{in}, was calculated using the recorded voltage, V, and current, I (Eqn. (4.2)).

Eqn. (4.2)

$$Q_{in} = V \cdot I$$

To allow full visual access to the total length of the thermosyphon, no insulation was used on the test section. Due to natural convection heat transfer to the surroundings inevitable energy losses were encountered. In order to account for these losses, a natural convection measurement was carried out. This test consisted of applying a heat flux to the evaporator section, while no working fluid was present in the system. Any heat transfer would be purely due to conduction through the tube and natural convection to ambient air. The total heat transferred to the evaporator could then be estimated using Eqn. (4.3),

Eqn. (4.3)

$$Q_{tot} = Q_{in} - Q_{NC}$$

where,

Eqn. (4.4)

$$Q_{NC} = hA(T_{ew} - T_{\infty})$$

This analysis showed losses of up to 6 % for the low pressure experimental conditions. For the higher pressure tests the losses due to natural convection were close to 15 % due to the higher operating temperatures. These losses were incorporated into the analysis presented in the results section.

For each power setting of the heater the corresponding heat flux for the evaporator and condenser sections, q_e and q_c [kW/m^2], were then calculated from Q_{tot} using the inner surface area, A_i, of the respective section, Eqn. (4.5). In this equation, $n = e, c, tot,$ representing the evaporator, condenser and total length of the thermosyphon.

$$q_n = \frac{Q_{tot}}{A_{i,n}}$$ **Eqn. (4.5)**

The heat transfer coefficient is calculated in each of the sections of the thermosyphon, and also across the entire tube, according to Eqn. (4.6). The heat transfer coefficient in the evaporator section, h_e, is calculated between the evaporator wall and evaporator vapour temperature measured in the lower evaporator pool, ($T_{ew} - T_{ev}$). The heat transfer coefficient of the condenser section, h_c, is estimated based on the temperature difference between the internal vapour and the condenser wall temperature, ($T_{ev} - T_{cw}$).

$$h_n = \frac{q_n}{\Delta T}$$ **Eqn. (4.6)**

For the analysis of the flow regimes in Section 4.4.2, the mass flux was calculated based on the heat transferred to the thermosyphon and the latent heat of vaporisation of the fluid, Eqn. (4.7)

$$G = \frac{q_n}{h_{fg}}$$ **Eqn. (4.7)**

The momentum flux, p, was also calculated for both the liquid and vapour phases using the phase density, according to Eqn. (4.8), where $k = l, v$.

$$p = \frac{G^2}{\rho_k}$$ **Eqn. (4.8)**

4.3.6. Uncertainty and error in analysis

In order to accurately measure the behaviour of the thermosyphon, all measurements were calibrated, as outlined in Section 4.3.2. Table 4.3 lists the uncertainties associated with each measurement device used during experiments. The propagation of these errors through the calculations performed on the data was calculated according the method outlined by Kline and McClintock [56], Eqn. (4.9). In this equation, x_i represents each variable on which the function, f, is dependent.

$$\Delta f = \sqrt{\sum_{i=1}^{n} \left(\frac{\partial f}{\partial x_i} \Delta x_i \right)^2} \qquad \textbf{Eqn. (4.9)}$$

Using Eqn. (4.9) the error incurred by the calculation of the input power, Q_{in}, was 0.03 %. Using the associated measurement errors in Table 4.3, the uncertainty in the calculation of the heat transfer coefficient was estimated not to exceed ± 10 %.

Measurement	**Device**	**Experimental uncertainty**
Wall Temperature	Omega T-type thermocouple	± 0.5 °C
Vapour temperature	Radionics K-type thermocouple	± 1 °C
Pressure	Omegadyne pressure transducer	± 3 %
Voltage & Current	Elektroautomatik power supply	< 0.2 %

Table 4.3 - Uncertainty associated with experimental measurements

4.4. Results and discussion – Flow regime analysis

One of the major advances of the present work compared with earlier thermosyphon studies is simultaneous and synchronised capturing of high-speed images and recording of temperature and pressure measurements. Two high-speed cameras allow for full visual access to the entire length of the thermosyphon, while temperature and pressure measurements provide further understanding of the behaviour of the thermosyphon. Changes in the thermal performance are interlinked with the flow phenomena and vice versa. For this reason, both elements need to be considered in tandem in order to understand the mechanisms occurring. In this way, the influence of bubble confinement, *Co*, and the rate of vapour production on the behaviour of the working fluid within a thermosyphon can be examined.

Dimensionless numbers are useful in flow analysis as a tool to pinpoint the forces dominating a particular two-phase flow behaviour. The Weber number, *We*, (Eqn. (4.10)) Bond number, *Bo*, (Eqn. (4.11)) and Froude number, *Fr*, (Eqn. (4.12)) describe the interaction between various forces and can be used to identify the dominant parameters influencing two-phase flow regimes.

$$We = \frac{G^2 D}{\rho_v \sigma_l} = \frac{Inertial\, forces}{Surface\ tension\ forces} \qquad \textbf{Eqn. (4.10)}$$

$$Bo = \frac{D^2 g(\rho_l - \rho_v)}{\sigma_l} = \frac{Gravity\ and\ body\ forces}{Surface\ tenstion\ forces} \qquad \textbf{Eqn. (4.11)}$$

$$Fr = \frac{G}{\sqrt{\rho_v(\rho_l - \rho_v) g D}} = \sqrt{\frac{We}{Bo}} = \frac{Inertial\ forces}{Gravitational\ forces} \qquad \textbf{Eqn. (4.12)}$$

For the present experimental conditions, a summary of the data has been plotted on the *We-Bo* graph, developed by Baba *et al.* [25], shown in Figure 4.3. From this figure it is clear that all experiments conducted as part of this study are well within the gravity/body force driven region, as is typical for Earth-based boiling scenarios, with low inertial influences. The position of the data with respect to the Weber number also indicates that the surface tension forces are dominant over the inertial forces. This is to be expected in a passive convective flow system whereby there is no externally 'pumped' forced flow through the system. The result of this is very low values of mass flux, and thus the Weber number, *We*, for the results presented. For example, the mass flux of the water case for the present work was of the order 10^{-3} kg/sm^2, whereas forced flow boiling systems are several orders of magnitude higher (G ~ 10 – 100 kg/sm^2). With gravitational forces dominating surface tension, and negligible inertial forces, it can be concluded that the gravity/body forces are most significant in the current thermosyphon investigation.

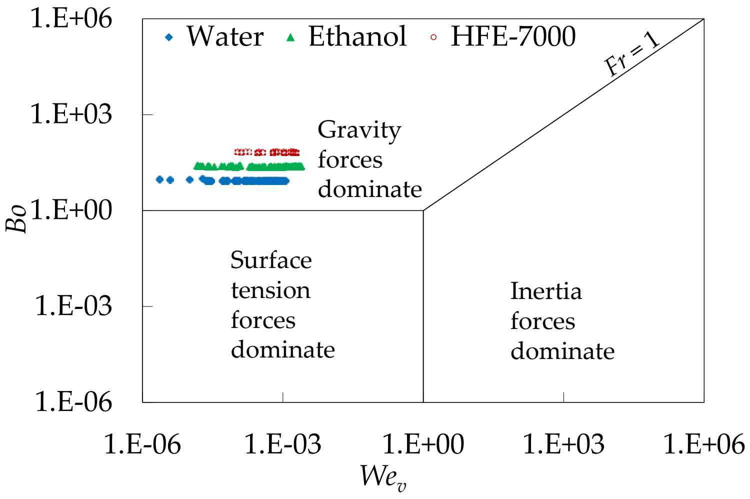

Figure 4.3 - Relative dominance of forces on two-phase flow in the current study

With this in mind, it was found that over the gravity dominated regime the two-phase flow behaviour within the thermosyphon is very sensitive to confinement effects, as noted by Di Marco [27]. Unconfined regimes behave in a manner similar to more established pool boiling regimes, with relatively small bubbles produced continuously. These regimes are generally anticipated in thermosyphon boiling. However, confined boiling regimes are characterised by bubble departure sizes commensurate with the size of the channel. The effect of confinement is heightened at smaller relative tube diameters and the resulting flow regimes are very different to the expected pool boiling regime. In order to investigate the range of parameters affecting small channel, counter-current flow in thermosyphons, three different fluids with varying properties, and thus different confinement levels, were tested and compared.

The relevant thermophysical properties of the three working fluids are listed in Table 4.1. Of particular interest in this investigation is the behaviour of fluids in small dimension tubes, where confinement of the bubble growth is expected, possibly leading to instabilities. These instabilities may present as an oscillatory behaviour of the two-phase flow regime, as identified in Chapter 3. Table 4.4 presents an overview of the flow regimes observed in the evaporator section for the range of test conditions along with the associated dimensionless numbers considered in the flow analysis. Table 4.5 presents an example of the observed trend in the evaporator temperature for each of the flow regimes observed in Table 4.4.

Ong and Thome [11] describe a transition region from micro to macro-channel type flows at $0.3 \leq Co \leq 1$, with the lower threshold for macro-scale flows in the range of approximately $0.3 \leq Co \leq 0.4$. As observed in Table 4.4, $Co = 0.34$ for water, indicating that confinement effects should be expected, typical of those discussed in Ong and Thome [11]. For HFE-7000, since $Co \ll 1$, confinement effects should be small, and a different boiling behaviour to that of water would be expected. For the case of ethanol, the confinement number, $Co \sim 0.2$, is between that of water and HFE-7000 and this is reflected in the observed boiling behaviour.

The rate of vapour production depends on a number of experimental conditions within the system. The pressure of the system strongly influences the vapour density, with vapour density rapidly increasing with increasing pressure. High system pressure results in high vapour density (and low vapour specific volume) and therefore a low rate of vapour production for a given heat input. The resulting two-phase flows are relatively slow and steady. Conversely, lower system pressure results in lower vapour density, and therefore the high specific vapour volume results in high vapour production rates. This leads to a more transient and explosive boiling condition. Similarly, for a given pressure, the heat flux of the experiment will influence the rate of vapour production and thus the two-phase flow regime. Higher levels of heat flux result in more vapour production and a more vigorous boiling. This results in flow regime changes with both pressure and heat flux as observed in Table 4.4, these changes will subsequently be described in more detail.

Fluid	P_r	Heat flux [*We*]	g $\longrightarrow$ 10 mm
Water *Co* = 0.34 *Bo* = 9	0.0002	7.5 kW/m^2 [2.8 x 10^{-5}]	
		19 kW/m^2 [1.7 x 10^{-4}]	
	0.006	5.5 kW/m^2 [2.3 x 10^{-6}]	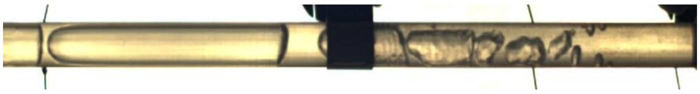
		17 kW/m^2 [1.9 x 10^{-5}]	
Ethanol *Co* = 0.2 *Bo* = 25	0.001	7 kW/m^2 [2.1 x 10^{-4}]	
		19 kW/m^2 [5.6 x 10^{-4}]	
	0.006	6.6 kW/m^2 [3.3 x 10^{-5}]	
		18 kW/m^2 [1.2 x 10^{-4}]	
	0.02	5.5 kW/m^2 [1.5 x 10^{-5}]	
		17 kW/m^2 [8.2 x 10^{-5}]	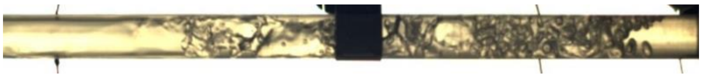
HFE-7000 *Co* = 0.12 *Bo* = 65	0.02	7.8 kW/m^2 [2.9 x 10^{-4}]	
		21 kW/m^2 [1.9 x 10^{-3}]	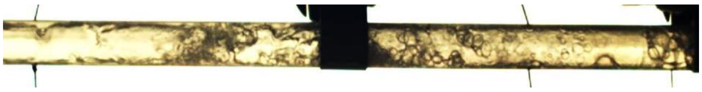
	0.04	7 kW/m^2 [1.6 x 10^{-4}]	
		15 kW/m^2 [6.9 x 10^{-4}]	

Table 4.4 - Overview of flow regimes for each fluid, reduced pressure, input power and dimensionless numbers, *Co*, *Bo*, *We*

Fluid	P_r	Heat flux [*We*]	
Water *Co* = 0.34 *Bo* = 9	0.0002	7.5 kW/m^2 [2.8×10^{-5}]	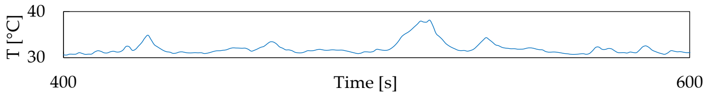
		19 kW/m^2 [1.7×10^{-4}]	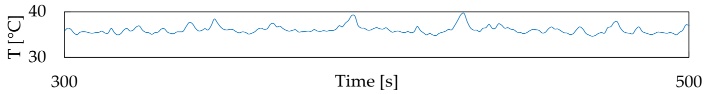
	0.006	5.5 kW/m^2 [2.3×10^{-6}]	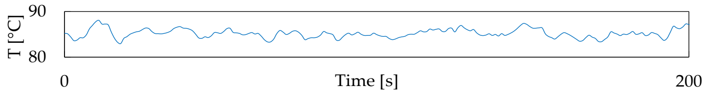
		17 kW/m^2 [1.9×10^{-5}]	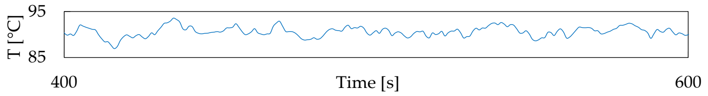
Ethanol *Co* = 0.2 *Bo* = 25	0.001	7 kW/m^2 [2.1×10^{-4}]	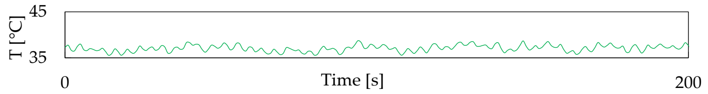
		19 kW/m^2 [5.6×10^{-4}]	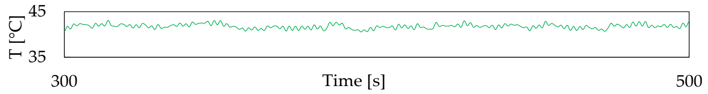
	0.006	6.6 kW/m^2 [3.3×10^{-5}]	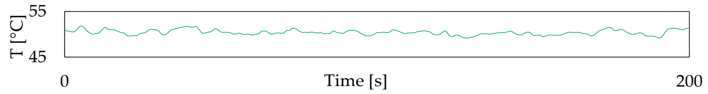
		18 kW/m^2 [1.2×10^{-4}]	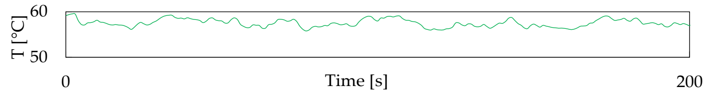
	0.02	5.5 kW/m^2 [1.5×10^{-5}]	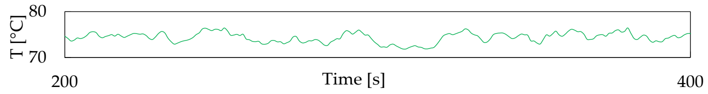
		17 kW/m^2 [8.2×10^{-5}]	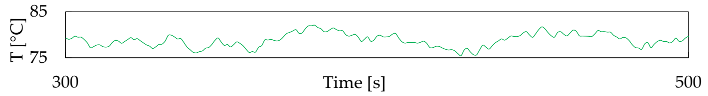
HFE-7000 *Co* = 0.12 *Bo* = 65	0.02	7.8 kW/m^2 [2.9×10^{-4}]	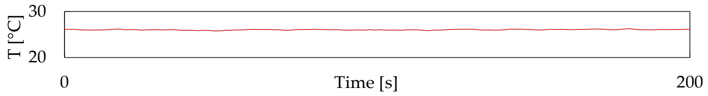
		21 kW/m^2 [1.9×10^{-3}]	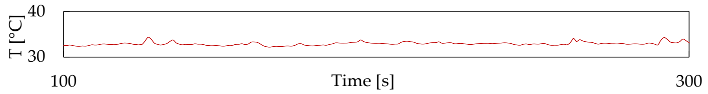
	0.04	7 kW/m^2 [1.6×10^{-4}]	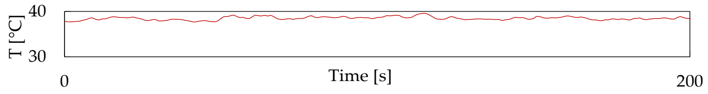
		15 kW/m^2 [6.9×10^{-4}]	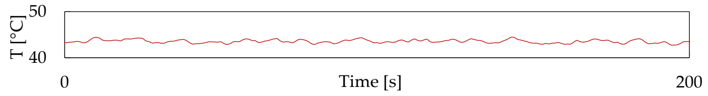

Table 4.5 - Overview of evaporator wall temperature time trace for test conditions

It was found in the present study that the vapour production rate of confined flow results in very different flow behaviour compared to the unconfined cases. Where the superficial vapour velocity is low (at high pressure, low heat flux conditions) it results in confined, slug-type flow regime where vapour bubble production appears slow and orderly. In contrast, at high vapour superficial velocities, as in the case of high heat flux and low pressure, the rate of vapour production becomes substantial, resulting in explosive boiling events and unsteady behaviour of the two-phase flow. During this case, liquid is forced to the condenser by the rapidly growing vapour, as depicted in the images of Table 4.4 for both water and ethanol.

It is therefore proposed that the flow regimes observed in the current study can be divided according to the level of confinement and vapour production rates for each experimental condition, as illustrated in the flow map Figure 4.4.

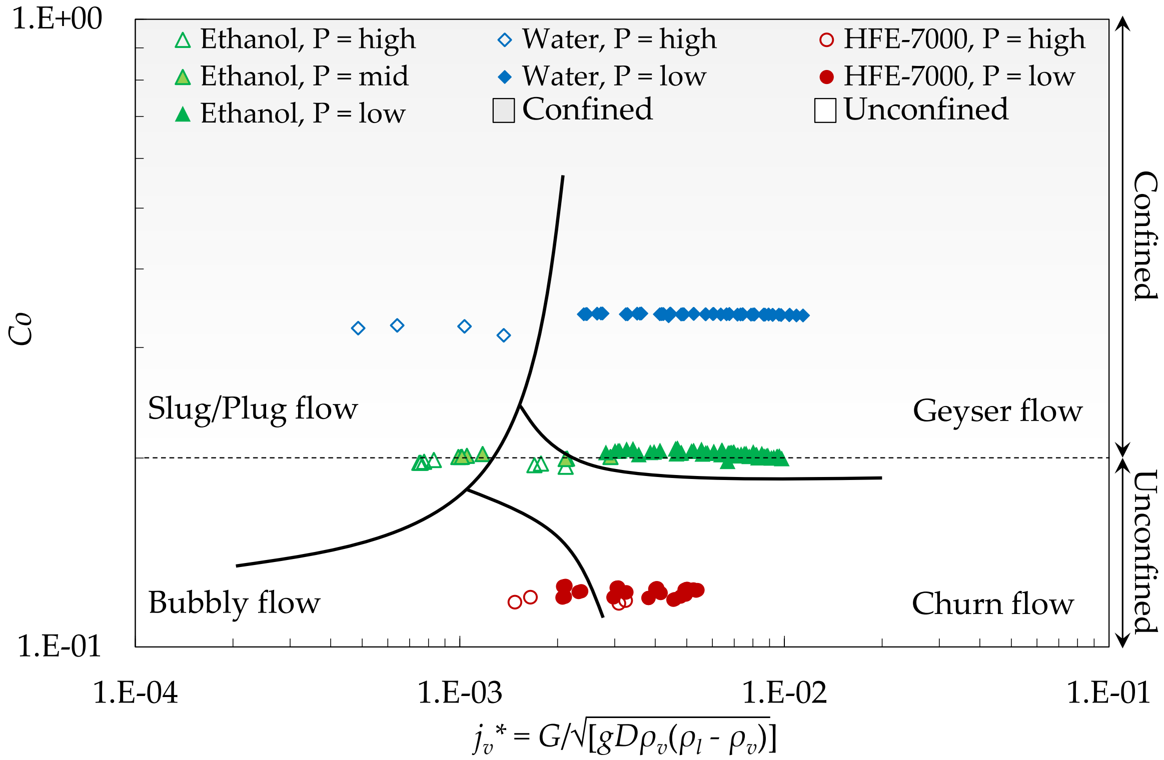

Figure 4.4 - Confinement and rate of vapour production of each fluid under investigation

This graph highlights the two-phase flow regime, as defined by the rate of vapour production, j_v^*, and degree of confinement, *Co*, for each of the fluids and associated test conditions. Two regimes, confined and unconfined flow, were identified through visual observation, with very different two-phase flow behaviours. Figure 4.4 gives an indication of the location of each of the test fluids in terms of the rate of vapour production, j_v^*, and Co.

In the low vapour generation region the associated bubble production rate is slower and steadier resulting in the slug/plug regime. If this flow is also confined, as observed in the current investigation, the bubbles gradually expand to fill the diameter of the channel and in some cases bubble coalescence occurs and larger bubbles are formed. This is referred to as slug/plug flow and is evident in the images of water and ethanol at higher pressures in Table 4.4. Moving to the right of Figure 4.4, high vapour production results in a churn-type flow for unconfined fluids. The geyser boiling regime is characterised by both high confinement and high vapour production rates, as seen for water and ethanol at low pressure in Table 4.4. With higher vapour production, the boiling events are explosive and periodic, leading to a transient oscillatory system. This oscillatory behaviour is evident in the corresponding temperature trace plots for low pressure water and ethanol in Table 4.5, where the lower vapour density caused higher vapour production rates. Along the vertical axis, the tube/fluid interaction is characterised. Small bubbles or large tube diameters will present low levels of confinement, characteristic of bubbly or churn flow. The flow regimes of HFE-7000 presented in Table 4.4 and corresponding steady temperature traces in Table 4.5 are typical of bubbly or churn regimes.

Changing the heat flux to the evaporator will also determine the horizontal position on the graph of Figure 4.4. Higher heat fluxes are associated with higher vapour production rates and will move the system to the right, with more aggressive geyser or churn behaviour observed. Similarly, changing the pressure of the system will significantly alter the vapour density within the thermosyphon. Lower pressures result in high vapour production rates and are more susceptible to geysering.

The main hypothesis explored in this work is that for gravity dominated two-phase flow within thermosyphons, the flow regimes and associated rate of heat transfer are dependent on the level of confinement and rate of vapour production rates.

For thermosyphons with confined boiling and high vapour production rates, oscillatory, geyser-type two-phase flow occurs. For confined thermosyphons with low vapour production rates, a slug-plug-type of flow regime, with a steadier operation, is observed. For unconfined thermosyphon flow, the flow regimes are not oscillatory. Low vapour production rates result in a bubbly-type flow, whereas high vapour production rates create a churn-type of flow.

4.4.1. Working fluid study

The focus of this investigation will be to study and categorise flow regimes in a reflux thermosyphon. The following sections will discuss these regimes in detail, while also looking at some interesting effects on the temperature and pressure. Particular attention will be focussed on the evaporator section during this investigation. In many cases it was found that at high vapour production rates, the flow structure in the evaporator dictated the general two-phase flow behaviour within the thermosyphon, including the condenser behaviour. This was especially true for confined boiling flows where a significant amount of liquid was pushed into the condenser region during geyser events. Only for the case of HFE-7000, due to it being unconfined, the vapour was free to rise to the condenser and falling film condensation was observed.

For each fluid, at various recorded experimental conditions, the flow regimes will be studied and grouped based on defining features. In this study, the basic flow recognition stemmed from the nucleation behaviour of the fluid under particular experimental conditions. The main regime differentiation was whether the bubble nucleation occurred in a single large bubble, explosive event, or whether smaller bubble nucleation and growth was sustained continuously, i.e. transient versus steady two-phase flow.

The definition of the flow regimes in this study were complicated by the nature of the counter-current two-phase flow that is present in this thermosyphon set-up. As discussed in Section 4.2.1, there are no existing flow pattern maps for closed counter-current, vertical flow as described in this investigation. Attempts were made here to draw analogies to vertical flow boiling patterns and confined flow boiling in mini and micro channels. However, a fundamental system difference in the current work was that there is no continuous flow channel for the developing regimes, since the mass fluxes are so low, i.e. there are no inertial effects. As a result, the flow of liquid and vapour within the thermosyphon is constantly conflicting, and once forces of either phase become large enough, this flow is easily disturbed.

The test case using water as the working fluid will first be described in detail in Sections 4.4.1.1 to 4.4.1.4, and following that will be compared to the case of HFE-7000 (Section 4.4.1.5 to 4.4.1.7) and ethanol (Section 4.4.1.8 to 4.4.1.11). All tests were conducted using both 50 % and 100 % filling ratio, however, no significant difference in flow were noted between these two fill volumes for the present investigation. In the following discussion, the 100 % fill volume will be considered, unless otherwise stated. The flow regime map presented in Figure 4.4 is used throughout the following sections to indicate the experimental conditions and resulting flow regime classification. For each discussion, an “X” on the flow map denotes the relevant position.

4.4.1.1. *Water at low pressure and low heat flux*

The heat fluxes tested in the case of water at low pressure, $P_r = 0.0002$, ranged from $q = 7.5 – 63$ kW/m². At this low reduced pressure, the bubble departure diameter, λ_c, was almost half the tube diameter and vapour production rates are relatively high. Single, explosive bubble nucleation is evident in both the flow visualisation and temperature and pressure recordings, for all levels of heat flux. These explosive boiling events give rise to a pseudo-steady oscillatory state. In this scenario, the thermosyphon is still capable of transferring heat, however the boiling events may cause shock damage to the thermosyphon components due to the pressure pulsations. Flow instabilities of this nature have been described in the previous literature, as outlined in Chapter 2. However, full field high-speed videography has not been performed so the precise mechanisms governing this behaviour have been largely speculative.

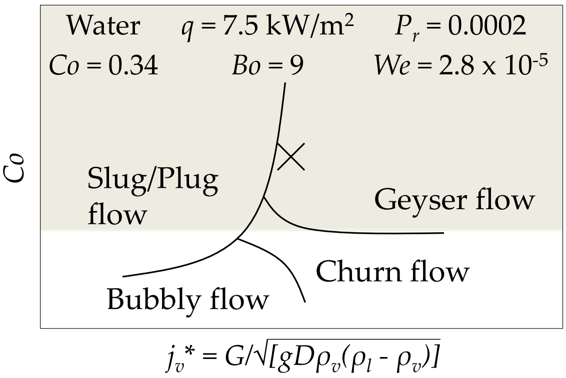

Figure 4.5 - Water at low pressure and low heat flux (parameter values shown in figure)

The position of water at low pressure and low heat flux in relation to the flow regime map is denoted by "X" in Figure 4.5. The high level of confinement for water at the current experimental conditions, coupled with the high rate of vapour production situates this state in the oscillatory geyser regime of two-phase flow.

The following discussion will focus on comparing the high-speed images of Figure 4.6 to the temperature and pressure measurements, shown in Figure 4.7. Figure 4.7 highlights the points along the pressure trace which correspond to the high-speed images.

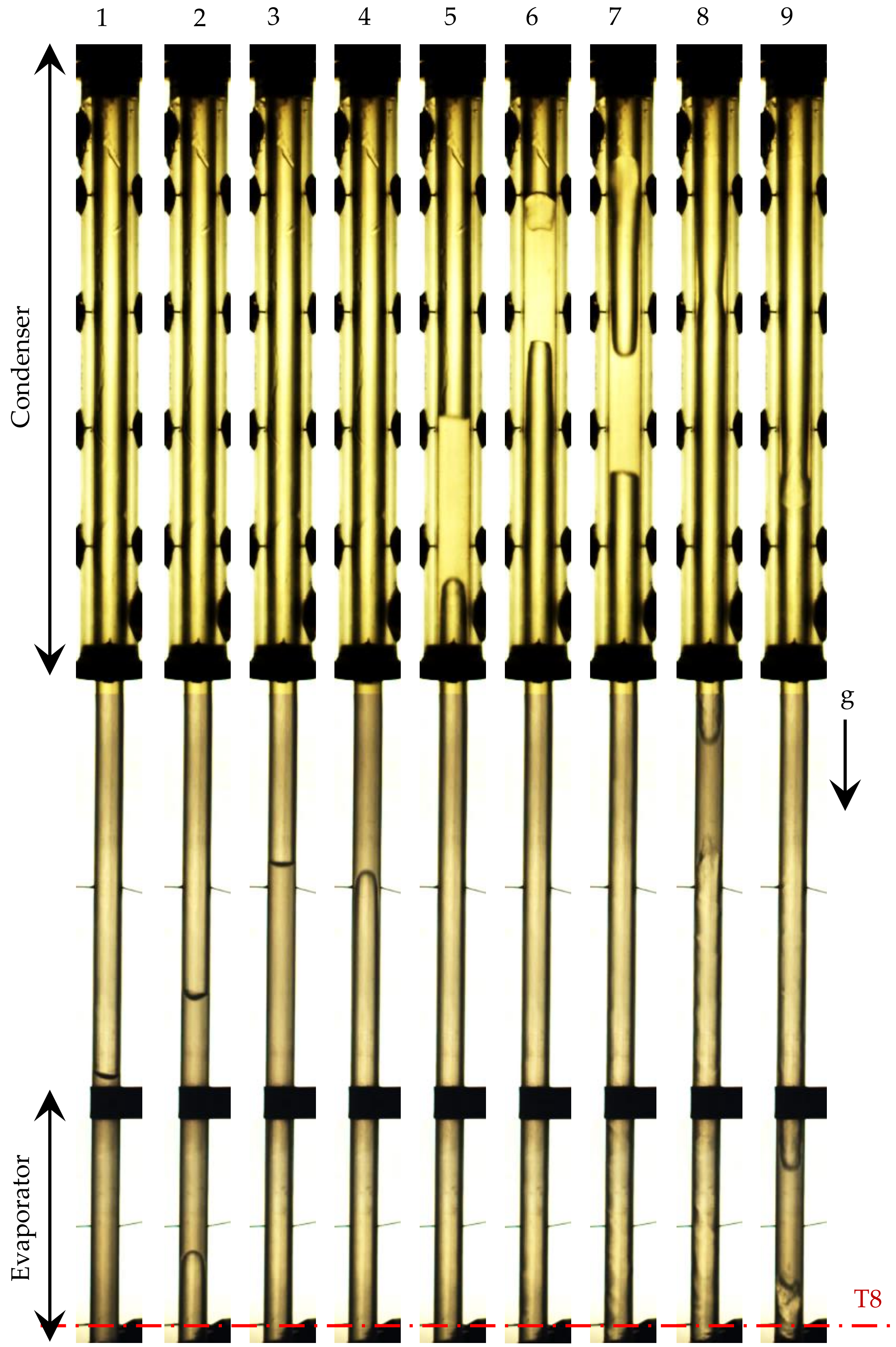

Figure 4.6 - Water thermosyphon, q = 7.5 kW/m², P_r = 0.0002, Δt = 0.06 s

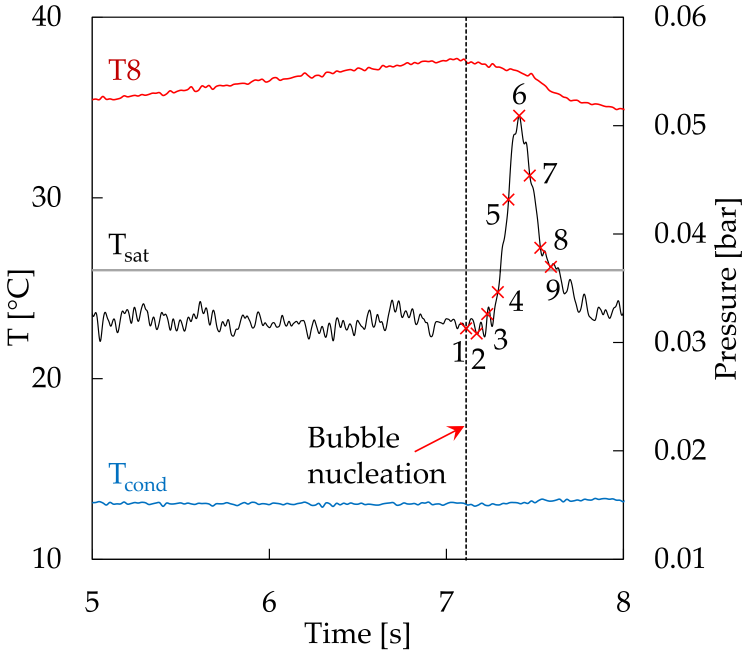

Figure 4.7 - Temperature and pressure trace for water at low pressure P_r = 0.0002, q = 7.5 kW/m²

The recorded images for water at the lowest heat flux of q = 7.5 kW/m², over a period of 3 seconds during a typical geyser event are shown in Figure 4.6, with the associated data in Figure 4.7. The images are separated by a time step of Δt = 0.06 s and start from bubble nucleation in Figure 4.6 (1), to vapour slug growth (2 – 4), with the plug reaching a peak height in the tube at Figure 4.6 (6), before dropping back to the evaporator (7 – 9).

Firstly, considering Figure 4.7, it is clear that prior to bubble nucleation the system pressure is steady and the wall superheat of the evaporator section is increasing steadily. The superheat in the lower evaporator section, T8, is initially ΔT_{SH} = 10 °C and rising with time. During this prolonged waiting period, the liquid pool remains stagnant, represented here in Figure 4.6 image (1). The heat supplied to the evaporator section is transferred to the liquid pool, and stored within it, by conduction and possibly some natural convection, however this is not visible in Figure 4.6 with the current set-up. The wall superheat continues to increase until bubble nucleation occurs, in this instance at the bottom section of the pool, as seen in Figure 4.6 (1). At this point the wall superheat begins to decrease due to evaporative cooling. The high vapour generation rate causes the Taylor-like bubble to grow to such an extent that it fills the tube. This can be attributed to the fact that there is a relatively high level of confinement at these test conditions.

Because nucleation occurred well below the free surface of the liquid, a large volume of liquid is trapped above the vapour slug, as depicted in Figure 4.6 (2). The high rate of bubble growth then forces this plug of liquid from the evaporator section to the condenser section. Thus, in contrast to conventional thermosyphon behaviour reported in existing literature, heat from the evaporator section is transported to the condenser as both sensible and latent heat. The notable decrease in wall superheat indicates an improvement in the heat transfer during the bubble growth phase as the bulk liquid begins to move.

With regard to the internal pressure of the system, as the wall superheat is increasing (between time 5 s and 6 s, Figure 4.7) there is very little change in the pressure. Attempts were made to measure the pressure in the evaporator though it was deemed impractical as it drained working fluid and influenced the boiling dynamics. This being the case, the sole pressure transducer is located at the top of the condenser section of the thermosyphon. Here the internal pressure is influenced by the movement of liquid plugs within the tube. As the liquid plug is forced upwards to the condenser, caused by the boiling event in the evaporator, the vapour in the condenser is compressed, resulting in an increase in the internal pressure in this region.

Due to the disparity between the liquid and vapour densities at this operating pressure (Table 4.1), evaporation results in a high rate of vapour production. The high vapour growth rate forces the liquid plug towards, and ultimately into, the condenser section. As the liquid plug is forced deeper into the condenser, the vapour, and possibly a small amount of non-condensable gas, in the top region of the condenser is compressed. This is evident in Figure 4.7 which shows that the pressure spikes between Figure 4.6 (3) and Figure 4.6 (6) increases sharply by 0.02 bar (57 % increase over quiet-phase pressure). As the liquid plug is cooled and returns back to the evaporator, the pressure reduces and returns to the original state. Once both temperature and pressure resume their state before the geyser event, the liquid pool is refilled and the cycle begins again.

As the bubble is forced into the condenser (Figure 4.6, 2 – 6) the meniscus of the plug tip is flat whilst the base of the plug is convex indicating that the pressure in the lower vapour region is higher than that of the upper region. Assuming quasi-static thermodynamic equilibrium, this will result in an increase in the saturation temperature. Since the wall temperature has dropped due to the evaporative cooling effect and the saturation temperature is increasing, the subsequent wall superheat decreases. In contrast, because the condenser wall temperature is relatively constant, the increased saturation temperature will result in an increased subcooling in the condenser. At Figure 4.6 (6) the liquid plug has reached its peak height in the tube and the pressure has also reached its peak magnitude. At this point the force due to the pressure acting on the base of the plug is insufficient to overcome the downward (pressure, gravity) and wall adhesion forces, and the plug begins to descend back to the evaporator. With changes in the forces acting on the plug, the top and bottom meniscus change shape, with the upper region being concave and the lower becoming flat. This would suggest that the pressure at the tip is now higher which, with the aid of gravity, forces the subcooled plug back to the evaporator.

Large amounts of energy were released when large liquid plugs collided with the end of the tube, or when two columns collided within the tube. Any vapour that had been present in the space between the columns rapidly collapsed. The energy from this collapse was released as sound and some was also transferred to the ends of the liquid columns. A ticking or clapping noise was audible during all of the water tests, a result of the water hammer effect occurring within the tube during oscillations. Most collisions were also followed by jets of liquid being pushed from opposite ends of the columns. This chain of events is depicted in Figure 4.8, with each successive image separated by $\Delta t = 4$ ms.

Figure 4.8 (1) shows the approach of two liquid columns, their direction of motion indicated by the black arrows on the left. On the instance of Figure 4.8 (2) a smacking sound was heard. Following this collapse of the vapour, the energy was transferred to the ends of the liquid column where distinctive jets were formed, image (3). Some heat from the lower column, rising from the evaporator is then transferred to the collapsed region and a vapour bubble forms and begins to grow, Figure 4.8 (4). The liquid jets also grow outwards, propelled by the initial energy release of the vapour collapse, Figure 4.8 (5 – 6).

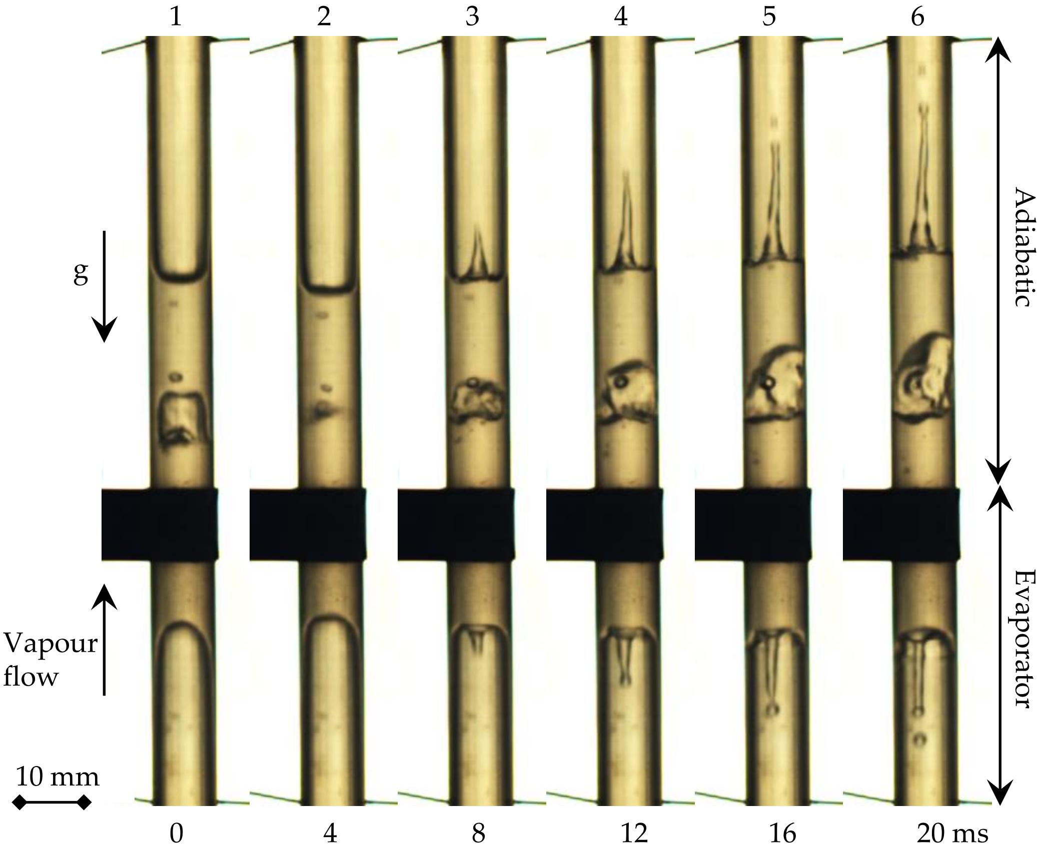

Figure 4.8 - Liquid jets following column collision. Water, $P_r = 0.0002$, $q = 7.5$ kW/m^2

4.4.1.2. Water at low pressure and high heat flux

The boiling behaviour described above was found to continue with increasing heat flux. However once the heat flux was increased, the frequency and magnitude of the events increased, as seen in Figure 4.9 and also Table 4.5. The events were also irregular in period, with some occurring close together, followed by shorter duration quiet phases where the liquid column attempted to return to the evaporator.

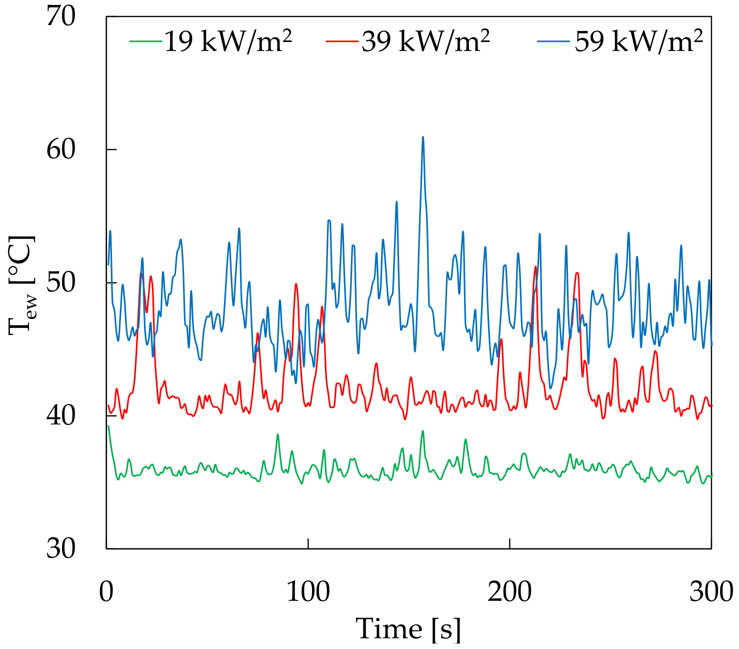

Figure 4.9 - Evaporator temperature trace for water at high heat flux 19 kW/m² < q < 59 kW/m²

The water boiling events were still subject to confinement, even at higher vapour production rates. Figure 4.10 shows an overview of the boiling regimes for water with each increasing heat flux between 19 kW/m² < q < 59 kW/m². In general, there is a smaller evaporator liquid pool with increasing heat flux as there is more liquid entrained upwards from the evaporator.

Observation of the high-speed images of Figure 4.10 shows the liquid plug often being held up in the adiabatic and condenser zones, oscillating between them. Rarely does the plug fully return to the evaporator. In the wake of a rising liquid plug some liquid flows back to the evaporator as a film on the walls and refills a small liquid pool. With higher levels of heat flux the time for these small pools to reach superheat for boiling is reduced and therefore the boiling events occur more frequently, which is evident in the temperature trace histories in Figure 4.9. As is shown, with increased vapour production rates, and thus higher vapour superficial velocities, there is an increase in entrainment of the liquid film returning to the evaporator. In the evaporator the boiling mechanism now resembles a more churn-type flow as seen in Figure 4.10, as more liquid is entrained in the high velocity, upward flowing vapour. In some cases, above $q > 39$ kW/m² film evaporation including some nucleation events are visible in the upper evaporator section.

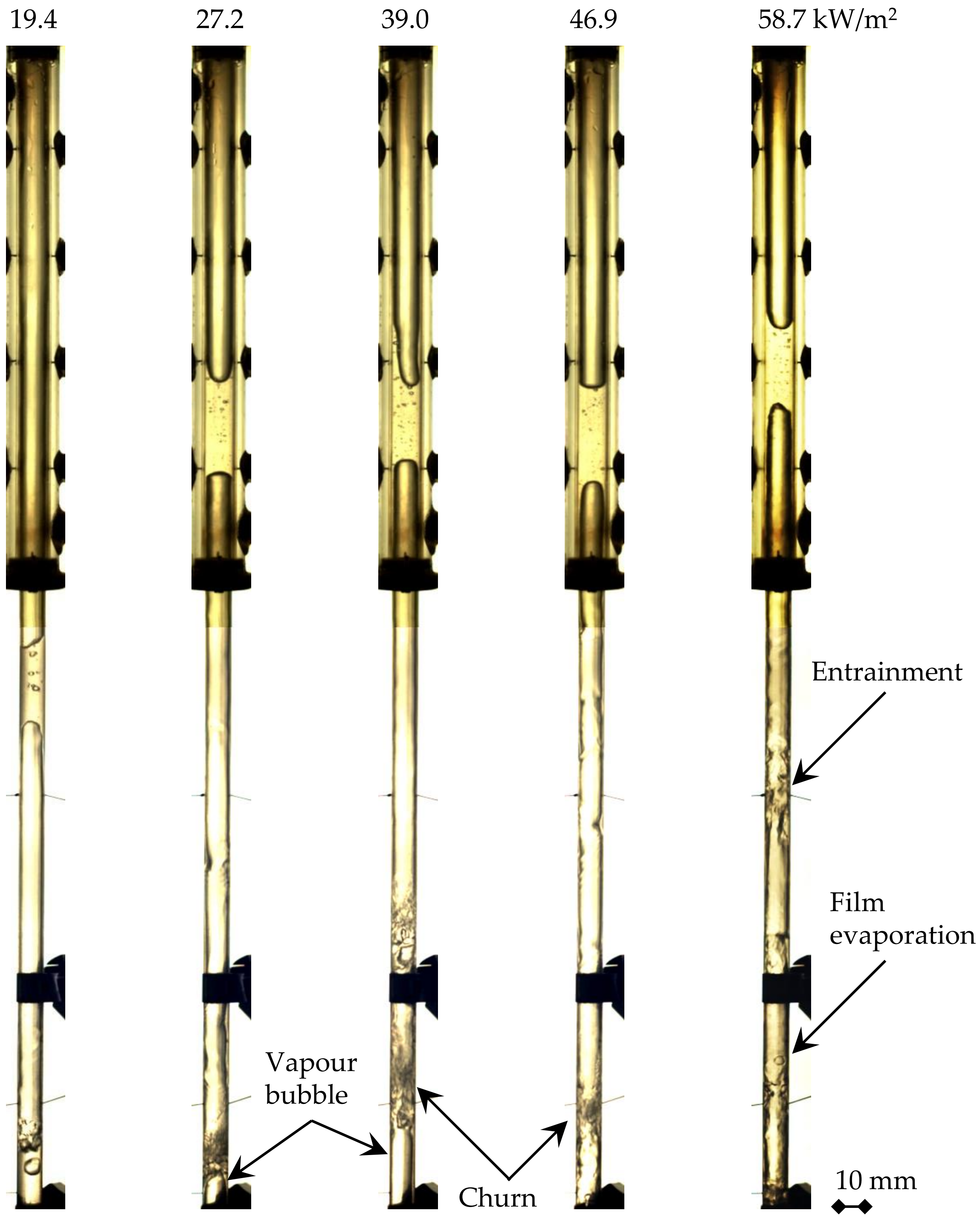

Figure 4.10 - High-speed images for water, 19 kW/m² < q < 59 kW/m²

For water at a higher heat flux of $q = 39$ kW/m², Figure 4.11 indicates that the characteristics of confinement and higher generation rate of vapour situate this state further into the geyser boiling regime. With further increases in heat flux at this low pressure the point moves further to the right of the graph, but the flow regime and heat transfer trends described are still applicable.

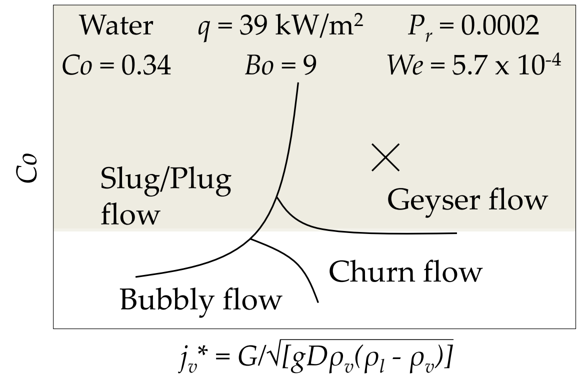

Figure 4.11 - Water at low pressure and high heat flux

It can be seen from Figure 4.12 that the effects of confinement are still evident at higher heat fluxes. The high-speed images in Figure 4.12 are at the same time spacing as those in Figure 4.6. It is evident at this higher heat flux that the vapour production rate is higher as the movement of the column through the thermosyphon is faster. Figure 4.13 shows the temperature and pressure time trace for this state, water at $q = 39$ kW/m² and $P_r = 0.0002$.

Considering the high-speed images of Figure 4.12, it is evident that there is little of the liquid pool remaining in the evaporator section. In Figure 4.12 (1) there is a column of liquid suspended in the condenser section, while a boiling event occurs in the evaporator, and high vapour velocities entrain liquid into the vapour core. This upward flow is continued in Figure 4.12 (2 – 3). The maximum height of the liquid plug is reached in Figure 4.12 (3) where the corresponding pressure also reaches a maximum in Figure 4.13. The plug begins to descend in the thermosyphon in Figure 4.12 (4), due to the same behaviour as in the case of lower heat flux, i.e. pressure and gravitational forces.

Figure 4.12 - Water, $P_r = 0.0002$, $q = 39\ \text{kW/m}^2$, $\Delta t = 0.06$ s

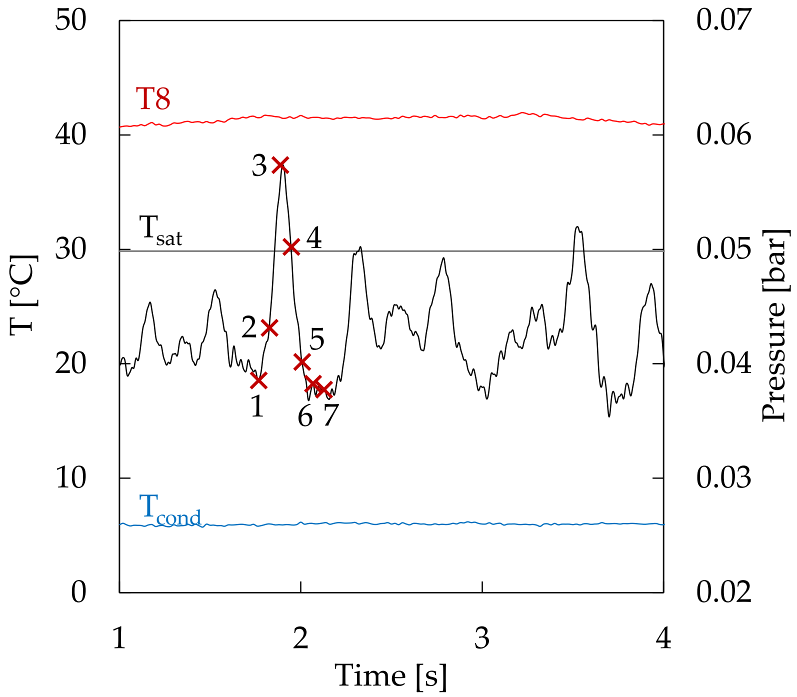

Figure 4.13 - Temperature and pressure trace, water, P_r = 0.0002, q = 39 kW/m^2

Only a very thin liquid film remains on the wall of the evaporator once the boiling event has occurred and high-speed vapour rises to the condenser. Due to the continuously imposed high heat flux, this liquid film is quick to evaporate until the walls are dry. At this point there is less vapour flowing to the condenser, and the plug is no longer forced upwards. The liquid plug descends to the evaporator in Figure 4.12 (4 – 6). Also evident in Figure 4.12 (4 – 6) is the flow of some liquid film to the evaporator section, as seen by ripples on the evaporator wall Figure 4.12 (5). This thin film is evaporating before accumulating to form a pool, due to the high level of heat flux. It is clear in Figure 4.12 (7) that the liquid plug is prevented from fully returning to the evaporator section due to the rising vapour generated by the evaporation of this returning liquid film in the heated section. This behaviour continues with evaporation of the remaining small liquid pool and further film evaporation, with the high vapour production rates forcing the liquid column upwards again to the condenser. In this way, the majority of the working fluid at this experimental condition is seen to oscillate as a liquid plug, mainly in the adiabatic and condenser section.

The temperature of the evaporator section during these explosive boiling events does not change significantly, due to high vapour generation rates, as shown in the plot of Figure 4.13. The thermosyphon enters a pseudo-steady, albeit oscillatory, state with regard to the wall temperatures, as the oscillations become more frequent, as shown in Figure 4.9. In terms of the pressure in Figure 4.13, it is clear that the oscillations have increased frequency from that of the lower level of heat flux, shown in Figure 4.7. Higher vapour production rates force the liquid plugs higher in the condenser section with greater velocity resulting in a more oscillatory pressure measurement.

Entrainment of the liquid into the vapour core is expected given the higher rates of vapour production and a significant degree of confinement in this counter-current two-phase flow regime. An example of entrainment can be clearly seen at q = 58.7 kW/m^2, shown in Figure 4.14. In Figure 4.14 (1) there is a thickening of the liquid film on the left side of the tube adjacent to the black arrow. With increased vapour production at higher heat fluxes, there is increased shear forces imposed on the liquid film in this location and it is pulled out from the wall, Figure 4.14 (2 – 3). The sheared film stretches to form a liquid bridge across the entire tube diameter, Figure 4.14 (4 – 5). With a further increase in the vapour upflow due to the high rate of evaporation this bridge is broken through and the broken droplets are carried upwards in the vapour core flow, Figure 4.14 (6). The increase of liquid entrainment from the liquid film together with the hold-up of the liquid plugs results in there being less liquid returned to the evaporator.

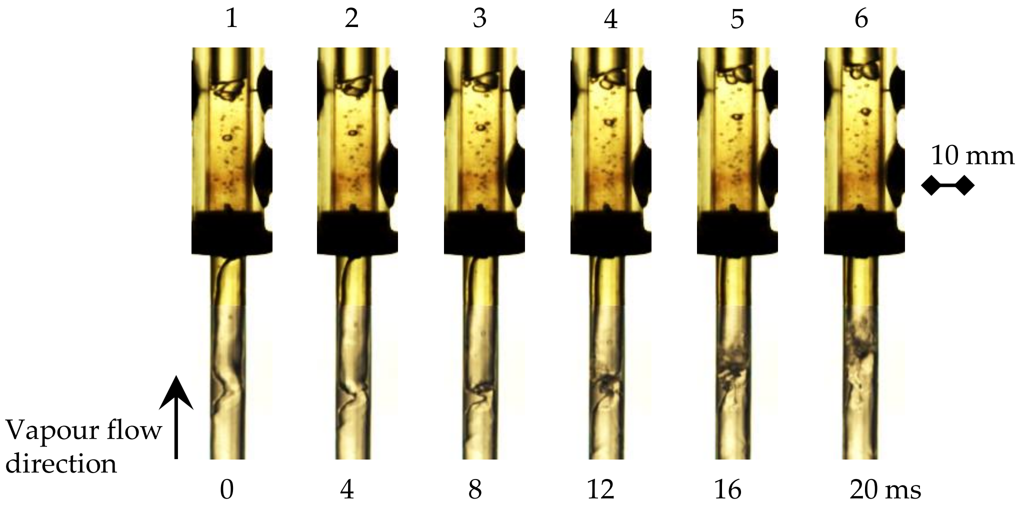

Figure 4.14 - Entrainment of liquid upwards by vapour flow (water, q = 58.7 kW/m^2)

The failure of the water thermosyphon was due to increased liquid entrainment with higher levels of heat flux levels $q > 60$ kW/m^2. When the vapour velocities are high enough, the entire liquid pool can be suspended in the condenser and the evaporator walls dry out. At the highest level of heat flux tested for water, dryout in the evaporator became extensive as most of the liquid was suspended and entrained into the vapour core before it was able to return to the evaporator. The liquid hold-up in the plug, combined with the continual entrainment at the exit of the evaporator, prevented sufficient liquid from returning to the evaporator. With little evaporation occurring, the evaporator wall temperature increased to a point where the boiling limit was reached and the superheat is such that re-wetting of the wall is prevented. At the highest level of heat flux, $q = 63$ kW/m^2, any liquid entering the evaporator boils instantly and a layer of vapour can become trapped, covering and insulating the wall. The thin layer of insulating vapour between the liquid condensate and the wall prevents any cooling of this section and no further evaporation takes place. This results in an excursion of the evaporator temperature and potentially dangerous conditions.

The two-phase flow dynamics and associated heat transfer mechanisms of this thermosyphon are very much different to that of the existing literature. This is mainly due to the effects of confinement, which was relatively high for all water tests at low pressure, $Co = 0.34$. The majority of previous research has considered thermosyphons with film evaporation and pool boiling in the evaporator and Nusselt-type falling film condensation in the condenser. Here the flow, heat transfer and thermodynamic state are highly transient and the heat transport mechanism from the evaporator to the condenser is a mix of sensible heat in the liquid plug, and latent heat in the vapour column. The flow dynamics in the condenser are imposed by the boiling behaviour in the evaporator, and for the majority of the tests this section is flooded with liquid.

4.4.1.3. *Water at high pressure and low heat flux*

The effect of higher pressure on the bubble size was investigated as a means to avoid the geyser boiling regime in the experimental set-up. Continuing with water as the working fluid, tests were conducted at a higher pressure of $P_r = 0.06$. For a 100 % evaporator fill volume, varying heat fluxes were imposed on the evaporator section, in the same way as Section 4.4.1.1. At higher pressures, the vapour density is increased tenfold, resulting in a much lower vapour production rate for a given rate of heat input. The level of confinement is still such that the flow can be regarded as confined. These conditions place the flow within the slug/plug regime, as shown in Figure 4.15.

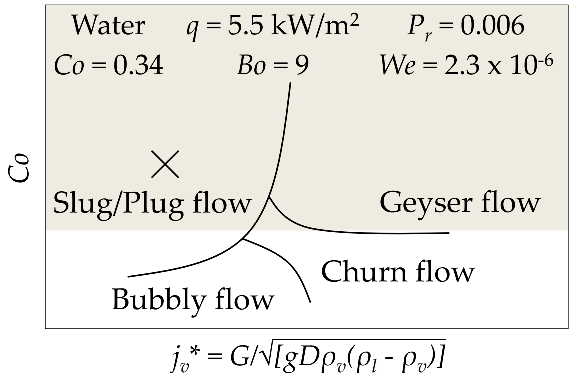

Figure 4.15 - Water at high pressure and low heat flux

Figure 4.16 shows the flow behaviour of water at higher pressure conditions, $P_r = 0.06$, and low heat flux setting, $q = 5.5$ kW/m^2. The time between each successive image is $\Delta t = 60$ ms and the corresponding temperature and pressure measurements are shown in Figure 4.17. In contrast to Figure 4.6 no liquid columns are forced into the condenser section due to the lower rate of vapour production associated with the higher vapour density at higher pressure. Bubble nucleation is higher in the evaporator pool and so there is less liquid trapped above the expanding vapour bubbles. The bubble nucleation is continuous, rather than a single event as seen with low pressure conditions, Figure 4.6. With lower vapour production rates, and thus lower vapour momentum, there is no churn evident in the flow. The fluid behaviour resembles that of slug flow, as described for flow boiling. This type of flow is characterised by smaller bubbles leaving the wall in a low mass flux flow boiling condition. The bubbles grow in the superheated pool and can coalesce to form larger Taylor bubbles, seen here in Figure 4.16 (6).

Figure 4.16 - Water at high pressure, P_r = 0.06, q = 5.5 kW/m², Δt = 0.06 s

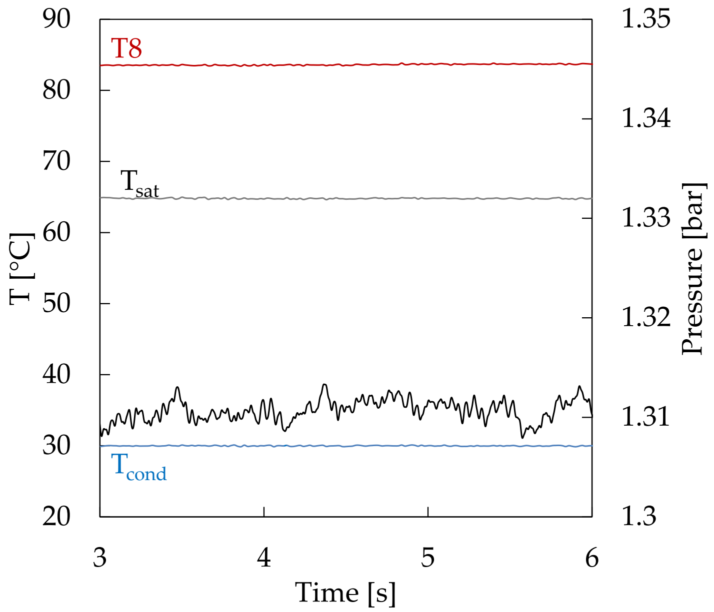

Figure 4.17 - Temperature and pressure trace, water at high pressure, $P_r = 0.06$, $q = 5.5$ kW/m^2

As the Taylor bubbles grow they can push a small bridge of liquid upwards towards the condenser. This is only sustained for a short period however, as it is fuelled by the evaporation of the film surrounding the bubble. Once this film has been evaporated the liquid bridge becomes thin, before breaking and flowing back to the evaporator as a film.

In terms of the condenser for this test, it can be seen that dropwise condensation is visible in the lower condenser section with a very thin film above, Figure 4.16. Further investigation, however, indicated that non-condensable gases could be present in the condenser during these tests. The presence of non-condensable gases in the condenser can limit the performance of this section, acting as a barrier to the vapour entering this region to condense.

Considering the temperature trace shown in Figure 4.17 (and Table 4.5) it is clear that the high pressure conditions present much steadier operation compared to lower pressures. There are also no significant oscillations in the pressure observed, indicating that there are no liquid columns forced to the condenser region, consistent with the visual observations of Figure 4.16.

4.4.1.4. *Water at high pressure and high heat flux*

For the high pressure experimental conditions, as the heat flux was elevated the rate of vapour production rate also increased. Water at the higher pressure and high heat flux is still positioned in the slug/plug regime as shown in Figure 4.18. However, the high-speed images of this experimental condition show trends of both churn and geyser flow, therefore, these experimental conditions may be in a transitional region between these regimes.

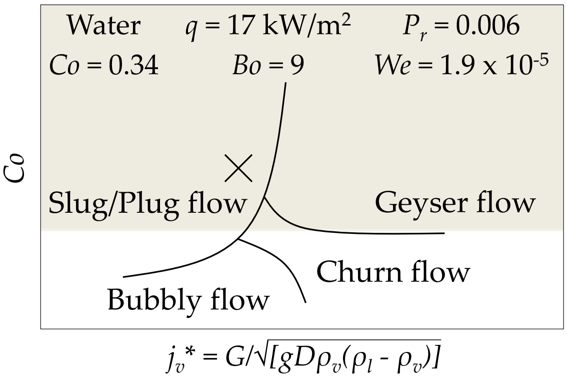

Figure 4.18 - Water at high pressure and high heat flux

An example of the flow structure for water at high pressure, $P_r = 0.06$, and high heat flux, $q = 17$ kW/m^2 is show in Figure 4.19, with corresponding temperature and pressure measurements. In this image, it is evident that there is increased vapour production in the evaporator section, but it has not reached the magnitude of that necessary for geyser boiling. It is likely that the pressure fluctuations evident in Figure 4.19 are exaggerated due to the presence of compressed gases in the condenser region. More bubbles are present in the lower evaporator section, while there is some churn and entrainment in the upper evaporator section, as indicated in Figure 4.19. In some cases, the bubbles coalesce and rise to the condenser, trapping a small amount of liquid in this region, and compressing the gases present in this region, resulting in the pressure spikes shown in Figure 4.19. However, unlike geyser boiling described in Section 4.4.1.1, these liquid plugs are small and do not travel far into the condenser region before being breached by the vapour. The peak liquid rise height is shown in Figure 4.19, and the liquid plug length in this case is less than 10 mm.

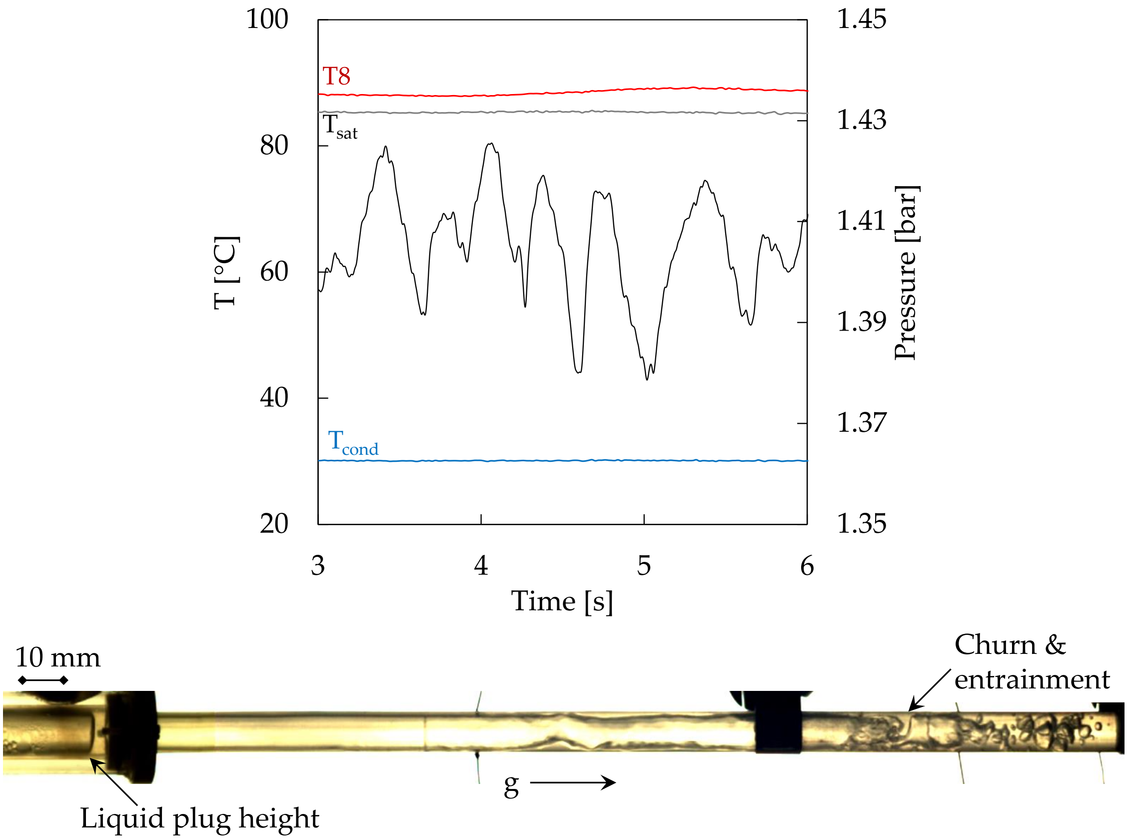

Figure 4.19 - Temperature and pressure trace, and high-speed image, water, $P_r = 0.06$, $q = 17$ kW/m²

From this pressure study it is clear that changing the pressure has considerable effects on the flow. This is mainly due to the fact that the vapour density is significantly affected by changes in the saturation pressure, since there is little appreciable change in the confinement with pressure. Higher vapour densities, at higher pressure conditions result in a lower vapour production rate for a given heat input. This creates a more relaxed, steady flow behaviour, shown here as a slug/plug flow regime. The higher pressure condition mitigates the explosive boiling conditions seen at the low pressure conditions where low vapour densities led to significantly higher vapour production rates.

4.4.1.5. HFE-7000 at low pressure and low heat flux

A comparison study using HFE-7000 was conducted to investigate the effect of changing confinement of the working fluid. HFE-7000 has a much lower surface tension (~ 80 %) and higher liquid-vapour density ratio to that of water, as shown in Table 4.1. This results in a much lower level of confinement, $Co = 0.12$. The HFE-7000 working fluid case was tested over a heat flux range of $7.8 < q < 21.5$ kW/m². Due to the lower boiling point of HFE-7000 ($T_{sat} = 34$ °C) at atmospheric conditions and lower *FOM*, the range of heat fluxes tested was limited by the onset of dryout earlier than the other working fluids tested. Pool boiling and film evaporation were present in the evaporator section at low heat flux. The unconfined behaviour of HFE-7000 meant that the bubbles did not grow to the size of the tube and thus do not force plugs of liquid into the condenser. Minimal oscillatory behaviour is observed and the thermosyphon operates in a more predictable, steady manner. Similar to the case of water, the vapour production increased with increasing heat flux and the flow became more churn-like with increased entrainment of the liquid film

The flow regime of HFE-7000 at lower pressure and heat flux is shown in Figure 4.20. Due to the much lower confinement of the vapour bubbles, HFE-7000 presented the closest behaviour to that of pool-type boiling in the evaporator section. At low heat flux levels, the flow was bubbly in nature, as indicated by the position in Figure 4.20.

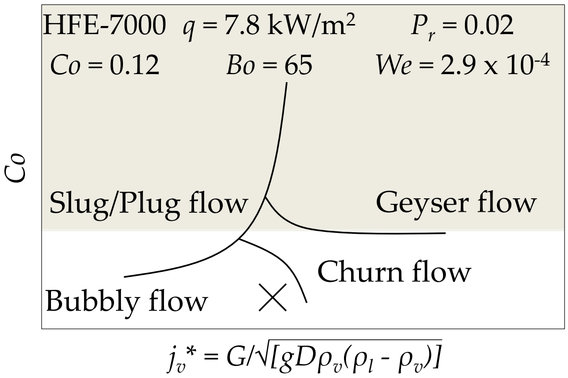

Figure 4.20 - HFE-7000 at low pressure and low heat flux

The temperature and pressure time trace plots are shown in Figure 4.21 for $q = 7.8$ kW/m². The corresponding steady two-phase flow behaviour is evident in the high-speed images, shown in Figure 4.22. It is clear in this image that, for the case of HFE-7000, the size of the bubbles produced is much smaller than that of the bubbles for the water case, and also small relative to the size of the thermosyphon diameter. Due to the smaller bubble size, and thus low confinement, the vapour is free to be released to the condenser section, with a small amount of liquid entrainment in the adiabatic section.

Liquid entrainment due to the upflow of vapour is evident in Figure 4.22 (3 – 4) which propels liquid to the top of the adiabatic section. Entrainment is a prominent behaviour with HFE-7000, a result of the lower surface tension of this fluid compared to water. Despite this behaviour, there is still sufficient liquid draining back to the evaporator section in this case so that dryout does not occur. For these HFE-7000 cases, due to lower confinement and high vapour production rates, the heat transfer mechanisms are more conventional and heat is transported from the evaporator to the condenser by latent heat, resulting in steadier thermal measurements, shown in Figure 4.21.

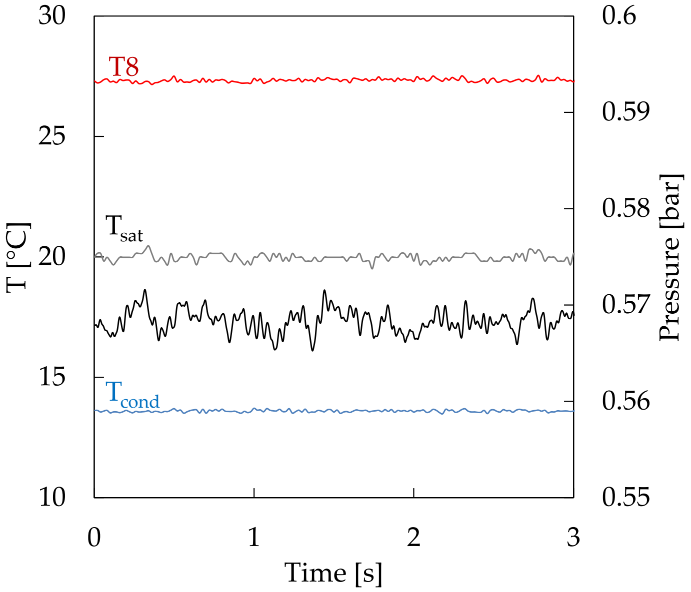

Figure 4.21 - Temperature and pressure trace, HFE-7000, P_r = 0.06, q = 7.8 kW/m²

Figure 4.22 - HFE-7000, $P_r = 0.06$, $q = 7.8$ kW/m², $\Delta t = 0.06$ s

4.4.1.6. HFE-7000 at low pressure and high heat flux

Further increase of the heat flux in the HFE-7000 fluid test changes the flow regime to that of film evaporation including nucleation events in the evaporator at $q = 21$ kW/m^2. The position of this regime is shown in Figure 4.23. Higher rates of vapour generation increase the liquid entrainment such that only a thin film returns to cover the wall of the evaporator. This leads to an annular-type flow in the evaporator, where higher heat fluxes result in nucleate boiling occurring in this thin film.

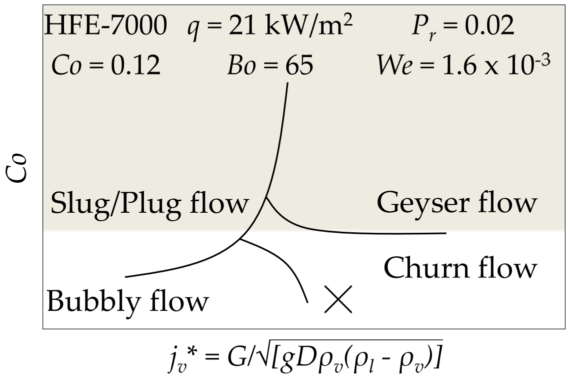

Figure 4.23 - HFE-7000 at low pressure and high heat flux

This regime is depicted in Figure 4.24. The majority of the working fluid is held in the condenser in this instance. The liquid hold-up is indicated by the increase in pressure fluctuations at this higher level of heat flux, shown in Figure 4.24. Interestingly, however, there is still enough condensate returning to the evaporator to wet the surface of this section, unlike the behaviour of water during tests involving large amounts of entrainment. This continuous film in the evaporator section results in a steadier behaviour of HFE-7000, even close to the point of failure which can be seen in the temperature time trace plot in Figure 4.24. As will be seen in Section 4.5.2, the heat transfer coefficient increases slightly at higher levels of heat flux tested, due to the thinning of the liquid film in the evaporator. This regime is thus characterised as an annular-type regime where only a thin liquid film is maintained on the evaporator walls.

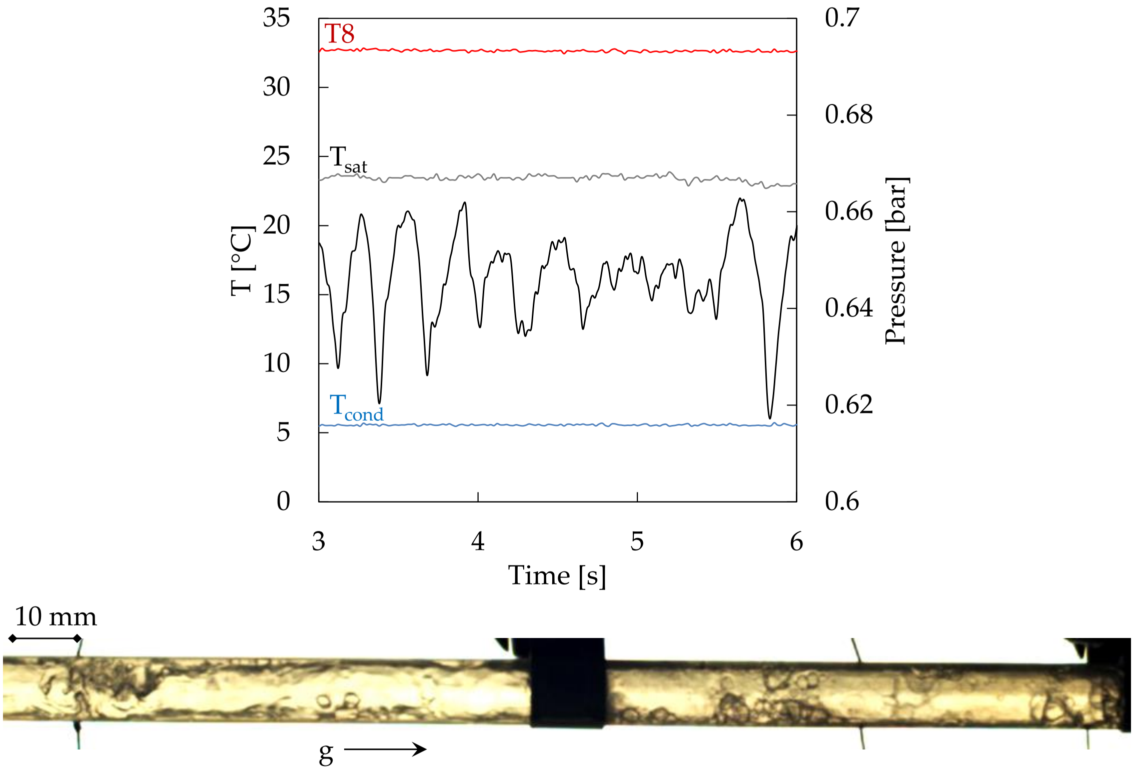

Figure 4.24 - Temperature and pressure trace, and high-speed image showing film evaporation with nucleation, HFE-7000, $P_r = 0.02$, $q = 21$ kW/m²

The failure of the thermosyphon for the case of HFE-7000 is due to further increasing the heat flux, generating higher rates of vapour production, such that the liquid film on the evaporator wall can no longer be sustained. Dryout of the evaporator wall occurs to an extent that rewetting is no longer possible and large temperature excursions occur.

The churn and bubbly flow regimes, typical of unconfined liquid with relatively high levels of vapour production, demonstrate that this thermosyphon set-up is capable of behaving closer to that traditionally described in the literature, with pool boiling and film evaporation occurring in the evaporator at higher pressures.

4.4.1.7. HFE-7000 at high pressure

In a similar manner to the tests carried out for the case of water, the HFE-7000 was tested at a higher pressure, $P_r = 0.04$. The higher pressure resulted in reduced vapour production rates, due to an increase in the vapour density (~ 50 %). Figure 4.25 shows the position of these test cases in terms of the flow regimes described previously.

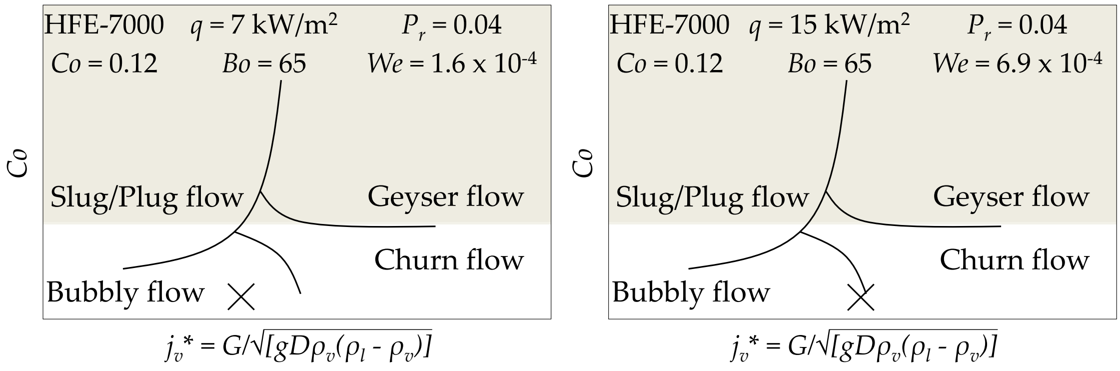

Figure 4.25 - HFE-7000 at high pressure, low heat flux (left) and high heat flux (right)

Due to the fact that the flow regimes of HFE-7000 were unconfined and steady at low pressure conditions, at this higher pressure, there is very little change in the flow regimes observed. The main difference being that these test conditions exist mainly in the bubbly flow regime, due to the lower vapour generation rates.

4.4.1.8. *Ethanol at low pressure and low heat flux*

To provide a contrast in behaviour between the HFE-7000 and water, ethanol was chosen as a third working fluid. Ethanol was chosen as it has $Co = 0.2$, between that of water and HFE-7000. The tests using ethanol as the working fluid were carried out in the same manner as the other fluids described and over a heat flux range of $7 < q < 46.5$ kW/m^2. The thermosyphon was tested at both half and full fluid loading, however, very little difference was observed between the tests. For the following discussion, only the full evaporator case will be considered.

The pressure was reduced to $P_r = 0.001$ for the initial, low pressure study and the heat flux initiated at $q = 7$ kW/m^2. According to the flow regime map shown in Figure 4.26, ethanol at low pressure and low heat flux are close to the edge of the confined regime, $Co = 0.2$, but with similar vapour production rates to that of water. The lower confinement level of ethanol results in flow regimes different to that of water.

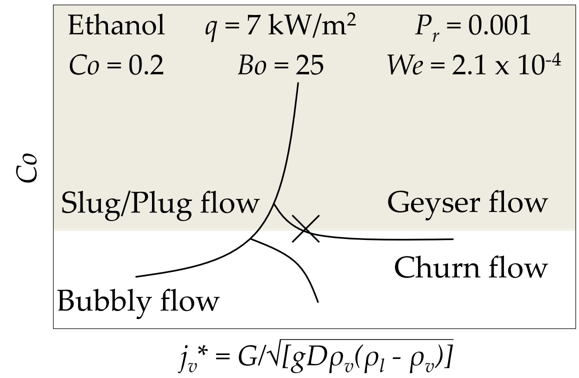

Figure 4.26 - Ethanol at low pressure and low heat flux

Figure 4.27 shows a high-speed image sequence of ethanol at $q = 7$ kW/m^2 and Figure 4.28 illustrates the associated temperature and pressure measurements for this event. This is an example of a typical boiling event for ethanol. The boiling behaviour at this experimental condition appears to be confined, in the sense that the bubble nucleates, grows quickly to the size of the tube and forces liquid into the condenser region, similar to the geysering behaviour described for water, Figure 4.27 (1). However, a noticeable difference here is that the liquid plug is not able to hold together in a column structure due to the combined effects of high vapour production rates and lower confinement of ethanol, compared to water, at this level of heat flux. Under these conditions the high superficial vapour velocity overcomes the lower surface tension forces of ethanol, and thus lower confinement, and shatters the liquid plugs, as shown in Figure 4.27 (2). Droplets from the plug are carried to the condenser region in a churn-type mass, Figure 4.27 (3). Once the liquid and vapour reach the condenser, the flow is cooled and slowed. The liquid droplets are deposited on the wall and begin to flow back toward the evaporator. There can be a period of time between the rise and fall of the liquid at this point as the liquid droplets collect in the condenser (note the high-speed images in Figure 4.27 (5 – 6) are separated by $\Delta t = 200$ ms). A quiet phase follows where the liquid is able to return to the evaporator in a continuous thick, wavy film refilling the evaporator section, as shown in Figure 4.27 (6 – 8). Once enough liquid has returned and the required superheat has been reached, another boiling event takes place.

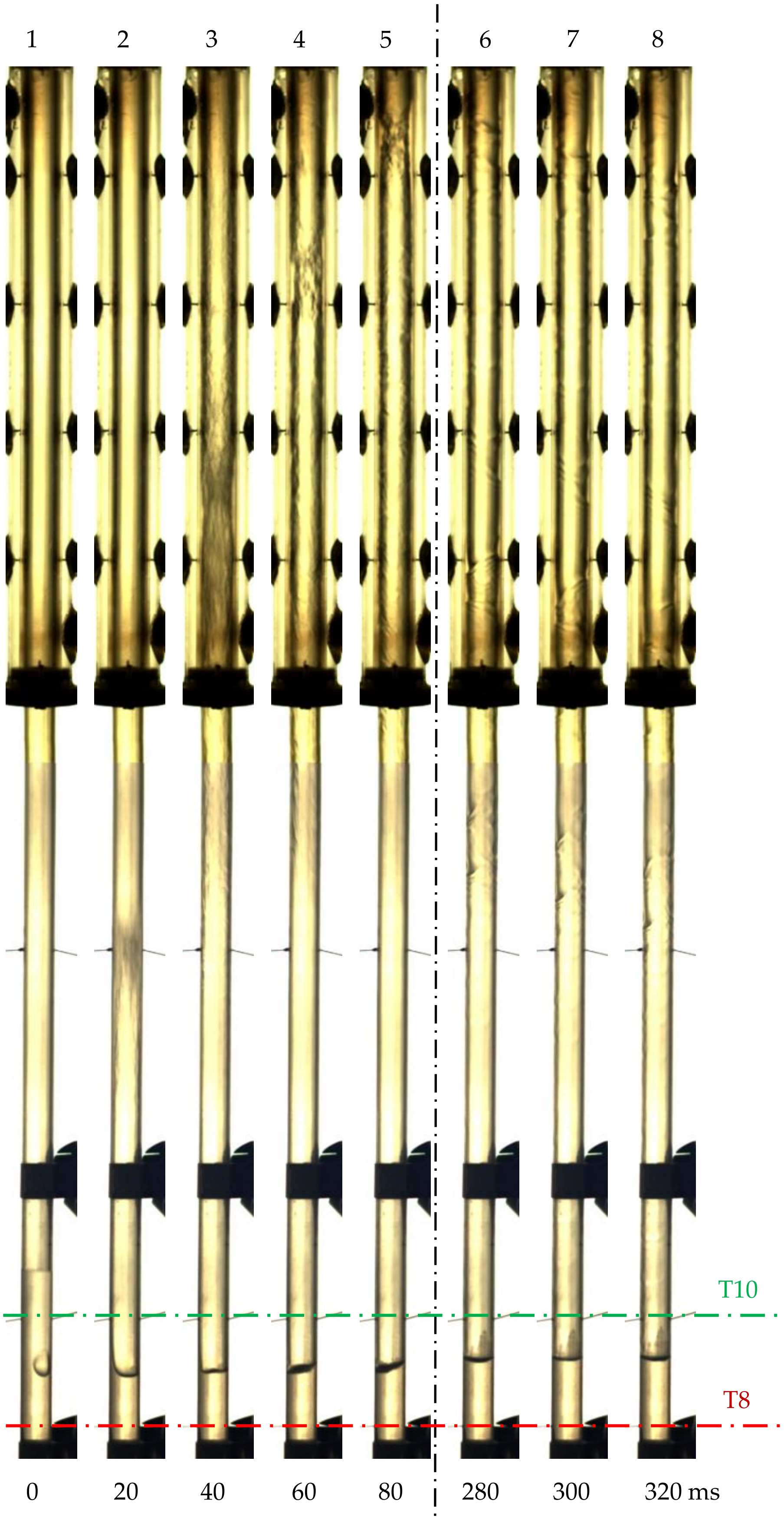

Figure 4.27 - Ethanol, P_r = 0.001, q = 7 kW/m²

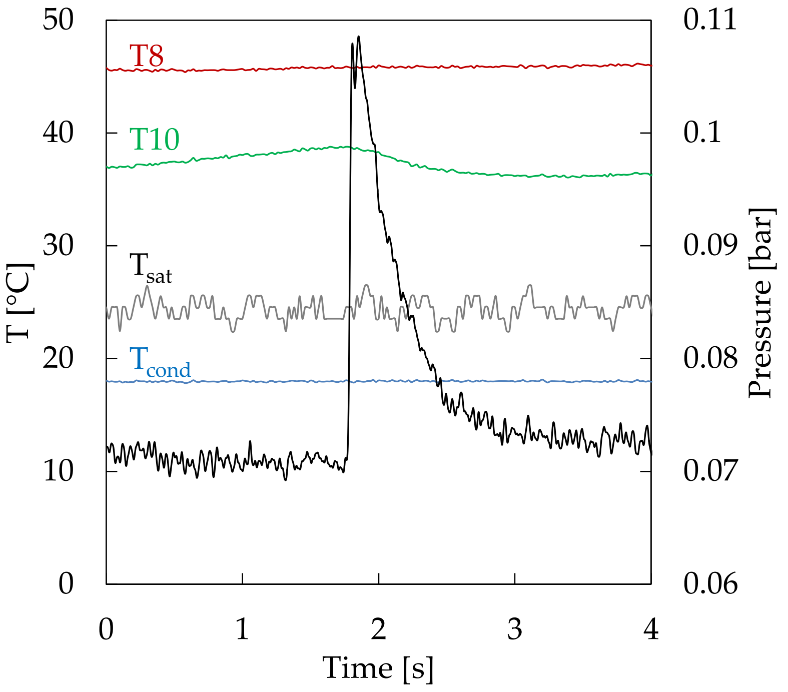

Figure 4.28 - Temperature and pressure trace, ethanol P_r = 0.001, q = 7 kW/m^2

Looking at the temperature and pressure plot in Figure 4.28 it is most obvious that there is a significant spike in the pressure reading with each boiling event. In the same way as with water, the peak of the pressure spike coincides with the liquid and vapour mass reaching the top of the condenser due to high vapour production rates and a relatively high level of confinement. In the case of ethanol, the increase in the pressure measurement has a much steeper gradient than that of water. The total increase in pressure is 0.04 bar during the boiling event, which represents a 60 % increase from the quiet phase pressure measurement. The temperature readings shown in Figure 4.28 are for T10 and T8 in the upper and lower evaporator section, respectively. Here it is evident that there is no major variation in the temperature of T8 in the lower evaporator during the boiling event. There is still a large amount of the liquid pool that remains in the evaporator section, so T8 is not cooled by the event and remains around 10 °C hotter than the upper evaporator section during the test. The upper section thermocouple, T10, shows a 2 °C change in temperature from the start to finish of the bubble nucleation event. There is an increase in the superheat in the upper evaporator from $t = 0 - 2$ s in Figure 4.28, as the upper liquid pool reaches the superheat necessary for bubble nucleation. Once evaporation has taken place in the upper evaporator the temperature measurement of T10 decreases.

The boiling events using ethanol occur with very regular frequency, as opposed to water which was more erratic, shown in the temperature traces of Table 4.5. Each boiling event for ethanol was separated by a quiet phase where the liquid was able to refill the evaporator section and the superheat increased to initiate another boiling event. Figure 4.29 shows the “steady” state for ethanol at low heat flux, $q = 7$ kW/m^2 and high heat flux, $q = 27$ kW/m^2. The lower graph in Figure 4.29 shows the frequency of pressure oscillation for each heat flux level, calculated using a Fast Fourier Transform (FFT).

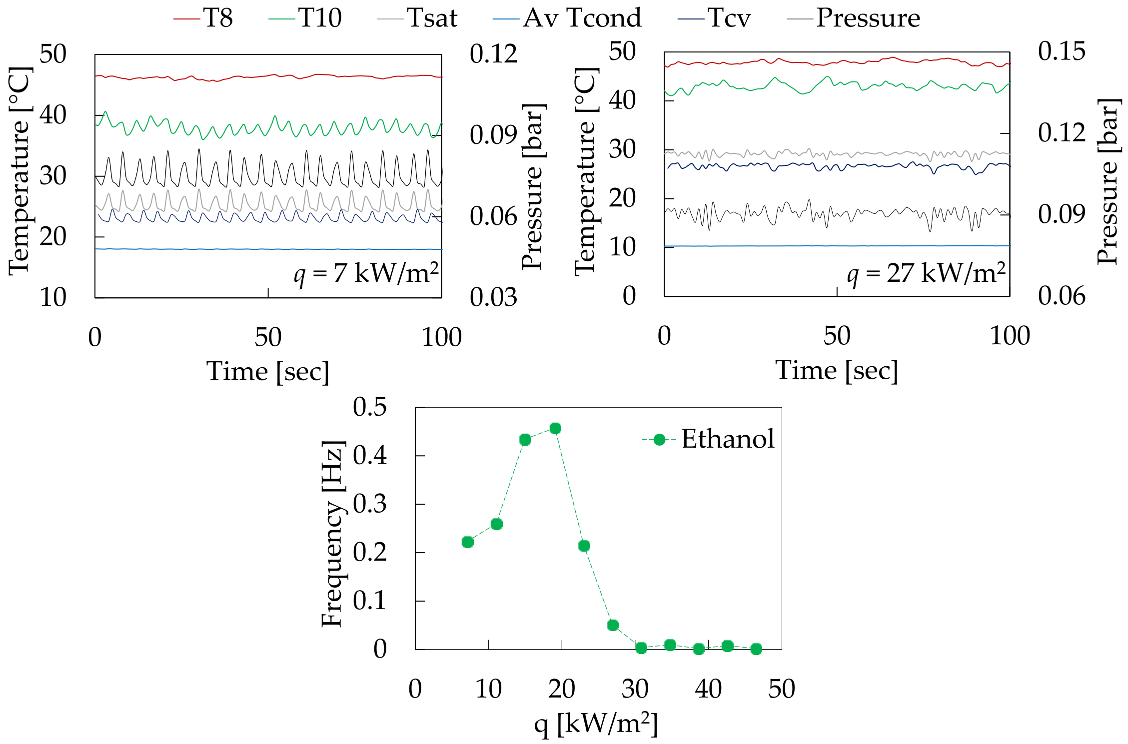

Figure 4.29 - Upper: Temperature and pressure measurements, $q = 7$ kW/m^2 and 27 kW/m^2; Lower: FFT derived frequency of pressure measurement, ethanol, $P_r = 0.001$

Considering first the temperature and pressure trace of $q = 7$ kW/m^2 in Figure 4.29, this graph shows the temperature and pressure time traces for the tests shown in Figure 4.27. Interestingly, shown in this graph is the temperature measurement of the internal condenser section, T_{cv}. This thermocouple shows a high degree of oscillation, due to the entrained liquid splashing the thermocouple in this region. The temperature of the upper evaporator (T10) oscillates by 2 °C, while the pressure fluctuates by 0.01 bar. This regular oscillatory behaviour was particular to ethanol as the working fluid up to a heat flux level of $q = 27$ kW/m^2.

As the heat flux was increased, the oscillations followed the same physical behaviour pattern, but the events increased in frequency and decreased in amplitude for higher imposed heat flux. This is illustrated in the lower graph of Figure 4.29. The period of oscillation increased to a maximum of $f = 0.46$ Hz, at $q = 19$ kW/m^2. This should be expected since an increase in the heat flux results in higher the vapour production but the level of confinement is unchanged. For ethanol the boiling events were distinguishable from one another with defined waiting periods. The oscillatory behaviour of ethanol could be sustained over very long periods of time, without the period of oscillation wavering for a given level of heat flux. The drop in frequency of the temperature beyond $q = 19$ kW/m^2, shown in the FFT plot of Figure 4.29, is a result of the boiling events of ethanol becoming so frequent that they occur continuously and in fast succession, with no distinguishable waiting time.

The measured temperature in the evaporator section for ethanol at high heat flux levels is shown in Figure 4.30, where the change in temperature behaviour between $q = 19$ kW/m^2 and $q = 27$ kW/m^2 is observed. The FFT analysis could not differentiate the individual boiling events as the heat flux increased beyond $q = 27$ kW/m^2, resulting in lower frequencies in Figure 4.29 for higher levels of heat flux. This behaviour is also shown in Figure 4.30 where the temperature of $q = 27$ kW/m^2 appears lower and less oscillatory than $q = 19$ kW/m^2. It is proposed that this loss of periodicity of the boiling events for ethanol signifies a change in boiling dynamics where the flow regime becomes more churn-like for $q > 27$ kW/m^2. The oscillations are continuous and the churn enhances the mixing of the two-phase flow, resulting in a steadier temperature measurement in the evaporator section. With a further increase in the heat flux, the boiling regime becomes more rigorous and thus high temperature oscillations are observed in Figure 4.30, for $q = 39$ kW/m^2.

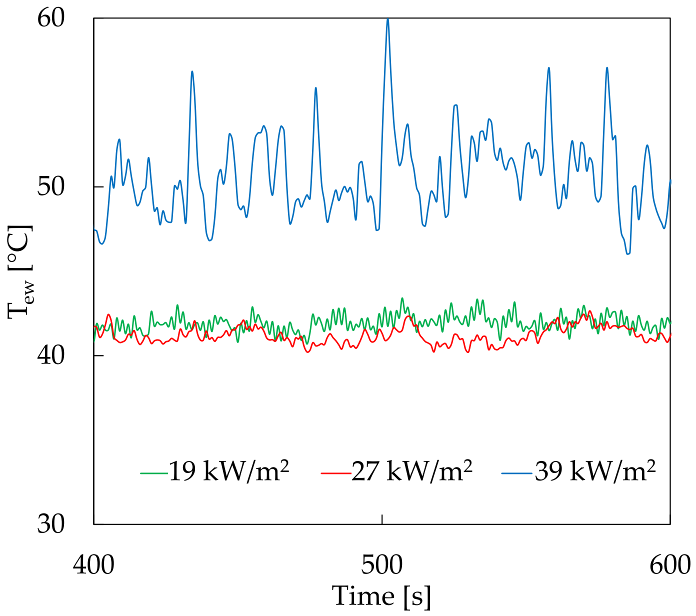

Figure 4.30 - Temperature traces for ethanol at high heat flux, $P_r = 0.001$

An example of the typical flow behaviour observed for ethanol over $19 < q < 46.5$ kW/m² is shown in Figure 4.31. From this figure it is clear that the liquid pool becomes progressively more depleted with increasing input heat. For a heat flux of $q = 39$ kW/m², there is sufficient superheat in the evaporator section for bubble nucleation to occur in the thin film present in this section. The temperature trace of Figure 4.30 for $q = 39$ kW/m² shows a high degree of oscillation and indicates the approach of thermosyphon failure. Once the heat flux is increased to $q = 46.5$ kW/m² the falling liquid film is no longer able to rewet the growing dry patches in the evaporator. This results in failure of the thermosyphon at this heat flux, where the evaporator temperatures rise sharply.

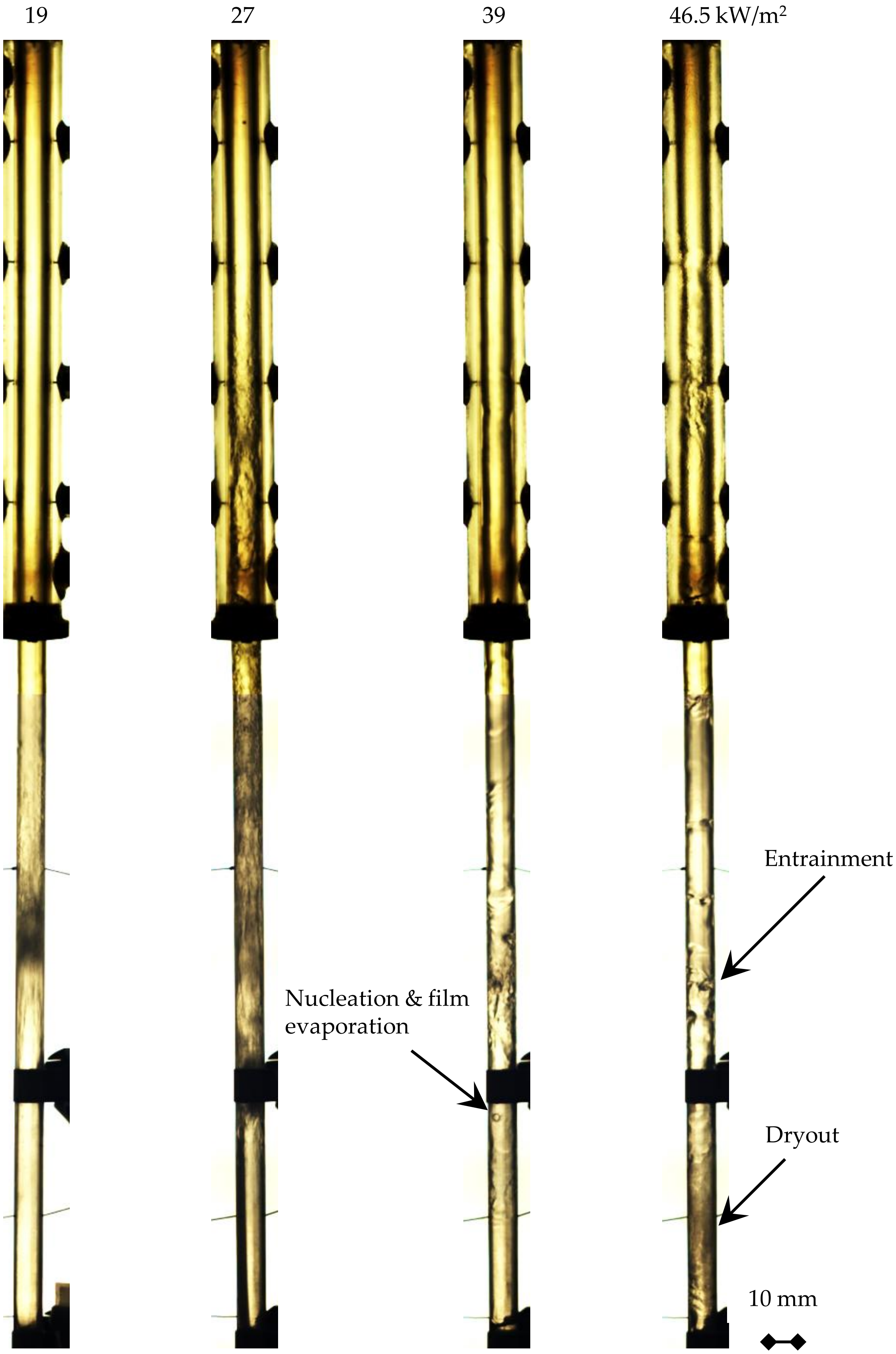

Figure 4.31 - Ethanol, $P_r = 0.001$, $19 < q < 46.5$ kW/m²

4.4.1.9. *Ethanol at low pressure and high heat flux*

For ethanol at high heat flux and low pressure, the flow regime is churn and the location is given on the flow map of Figure 4.32. As the heat flux of the ethanol is increased to $q = 27$ kW/m², there is no change in the level of confinement for $P_r = 0.001$. The vapour production rate increases with increasing heat input and the behaviour moves further along the border of geyser and churn-type flow.

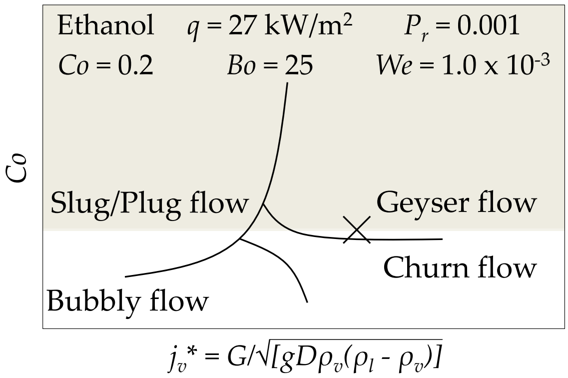

Figure 4.32 - Ethanol at low pressure and high heat flux

This confined, churn-type behaviour is evident for $q = 27$ kW/m² in high-speed images shown in Figure 4.33 and the corresponding temperature and pressure trace in Figure 4.34. It is clear from Figure 4.33 (1) that the liquid pool is smaller for the higher heat flux $q = 27$ kW/m². The higher input heat results in higher vapour production rates and thus more liquid transported away from the evaporator section. In Figure 4.33 (2) the effects of entrainment in the adiabatic section are evident. With higher vapour generation rates, more liquid is entrained and forced into the condenser section leaving a smaller liquid pool in the evaporator. As the liquid becomes subcooled on the wall of the condenser, a wavy film is formed.

It can be seen in Figure 4.33 (6) (this image is advanced 200 ms from the preceding image) that there are some dry spots formed on the surface of the evaporator wall. This is due to the high heat flux and continuous evaporation of the liquid film in this region. These dry spots are not detrimental to the thermosyphon performance, however, as the condensate film falls quickly to rewet the surface of the evaporator.

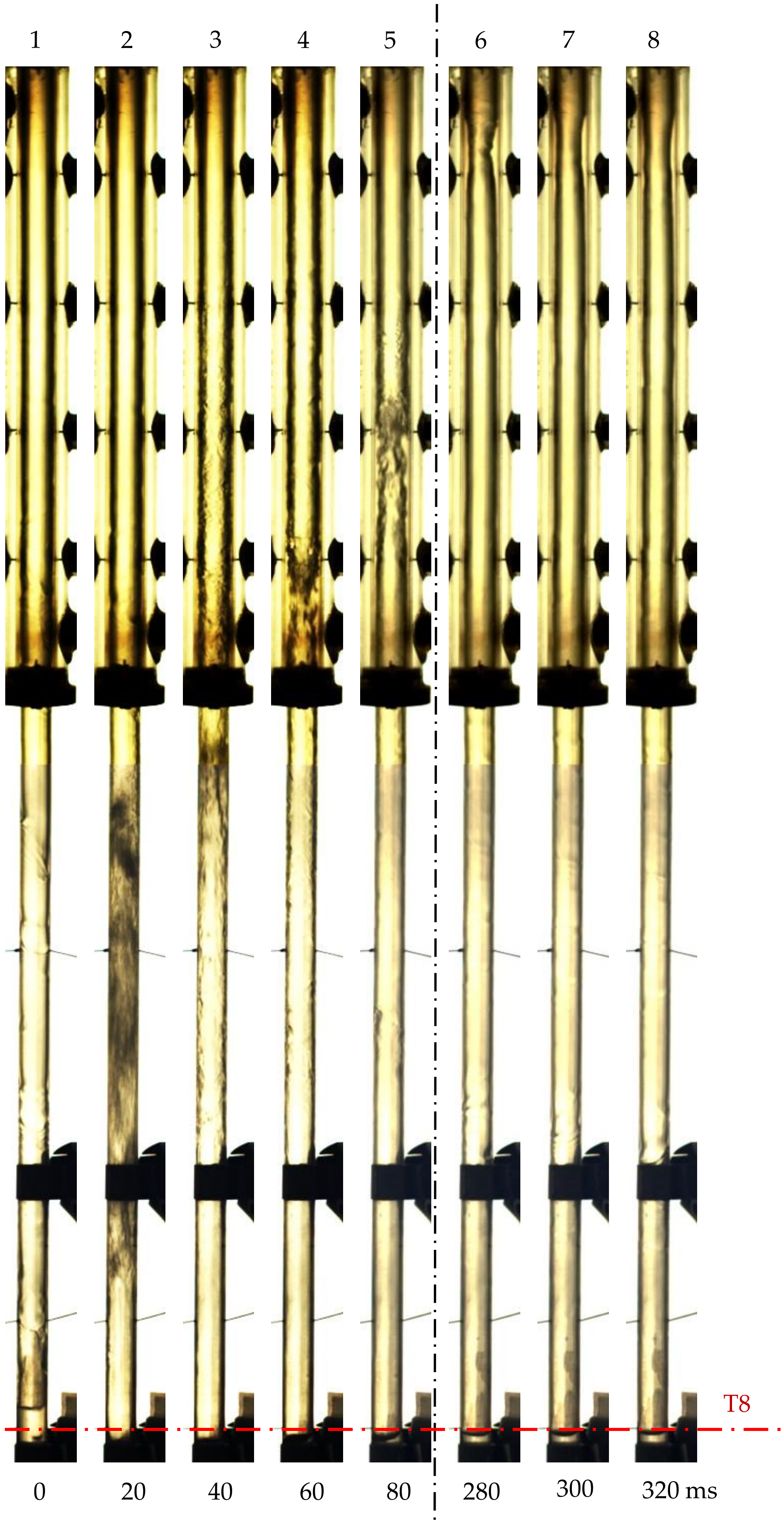

**Figure 4.33 - Ethanol, $P_r = 0.001$, $q = 27$ kW/m², **

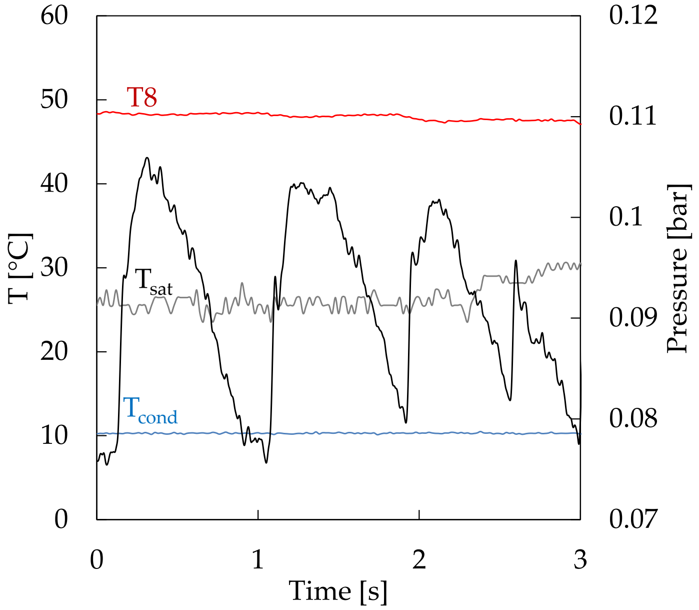

Figure 4.34 - Ethanol temperature and pressure trace, P_r = 0.001, q = 27 kW/m²

Figure 4.33 (6 – 8) shows the return of the wavy condensate film to the evaporator. The temperature and pressure plot in Figure 4.34, and previously Figure 4.30, show that the evaporator temperature is reasonably steady during this process, as the rapid boiling events maintain the wall temperature. However, large oscillations are observed in the pressure measurement, again attributed to the fast rising vapour and entrained liquid to the condenser region with each boiling event.

These results suggest that although geyser-type boiling and confinement are common when using water as the working fluid (Table 2.1), they are not exclusive to this working fluid. With a particular level of reduced pressure, heat flux, and high vapour production rates, geyser-type oscillatory behaviour can be achieved for confinement levels of $Co = 0.2$. This again highlights the importance of confinement and vapour production rates in the design of reflux thermosyphons.

4.4.1.10. Ethanol at high pressure and low heat flux

Similar to the previous two working fluid cases, the effect of changing pressure on ethanol was investigated. The pressure was increased for ethanol to $P_r = 0.02$. The higher pressure lowers the vapour production rate of ethanol, again due to a sharp increase in the vapour density. The regime of ethanol at high pressure and low heat flux is indicated in Figure 4.35. There is a significant flow pattern change for ethanol at this pressure condition where the flow regime transitions to slug/plug flow, as indicated in Figure 4.35.

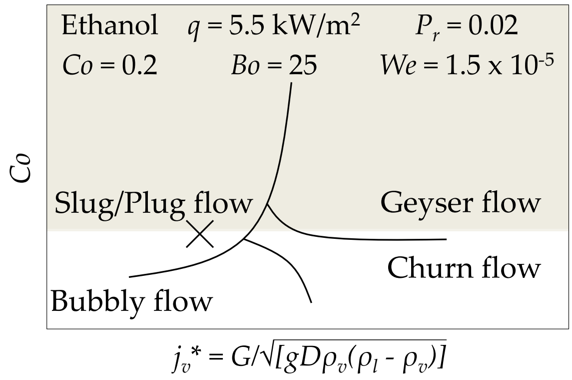

Figure 4.35 - Ethanol at high pressure and low heat flux

For the ethanol case at high pressure and low heat flux, Figure 4.36 presents an example of the flow regimes, with the corresponding temperature and pressure time traces shown in Figure 4.37. In Figure 4.36 it is seen that there is a continuous production of small vapour bubbles in the evaporator region. As these bubbles are further heated in the liquid pool they grow and coalesce, as shown in Figure 4.36 (1 – 2), due to the relatively high degree of confinement and low vapour production rates. Thin liquid bridges are sometimes trapped between the growing bubbles. The expanding bubbles are much less explosive than those of ethanol at lower pressures and so these liquid bridges are maintained for longer periods of time, again due to the low vapour production at the low level of heat flux. It is also evident from the temperature and pressure measurements shown in Figure 4.37 that these experimental conditions are conducive to steady, less oscillatory behaviour.

Figure 4.36 - Ethanol, $P_r = 0.02$, $q = 5.6$ kW/m^2, $\Delta t = 0.06$ s

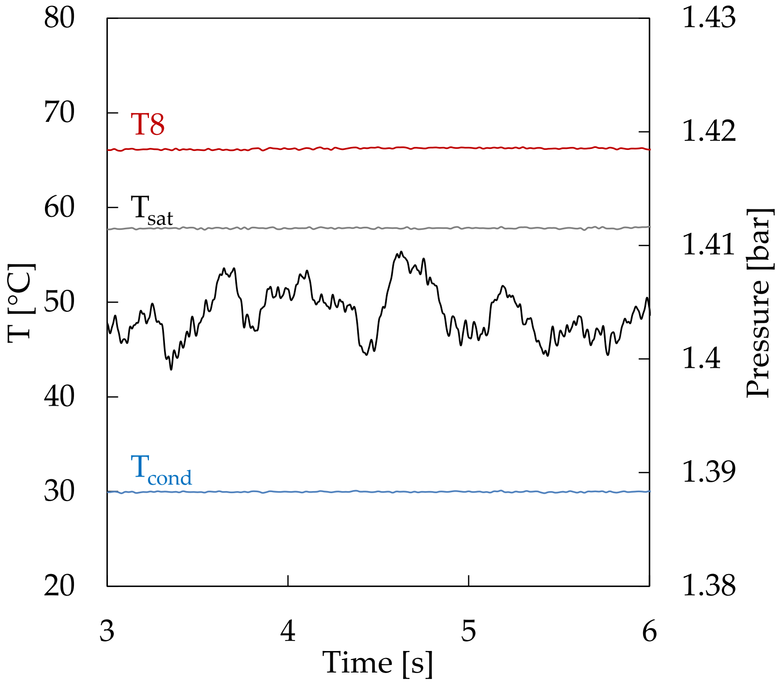

Figure 4.37 - Ethanol temperature and pressure trace, $P_r = 0.02$, $q = 5.6$ kW/m²

4.4.1.11. Ethanol at high pressure and high heat flux

Increasing the heat flux further for this pressure condition, $q = 17$ kW/m² at $P_r = 0.02$, has the effect of increasing the rate of vapour production without changing the level of confinement. The flow pattern in this case becomes much more churn-like with more small bubbles in the evaporator section as a result of the higher vapour generation rate, as shown in Figure 4.38.

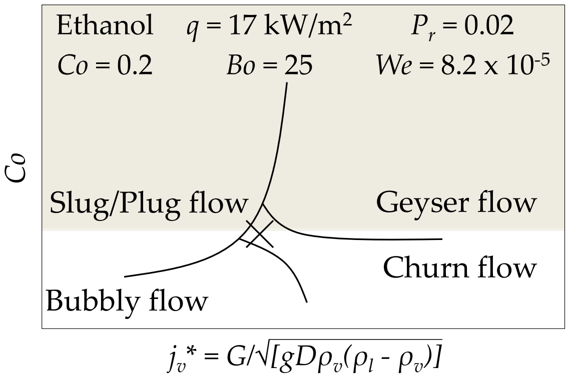

Figure 4.38 - Ethanol at high pressure and high heat flux

An example of the flow structure encountered for this test condition is shown in Figure 4.39, with associated temperature and pressure measurements. The higher heat flux generates more vapour in the evaporator, in turn causing more churning at the liquid-vapour interface, relative to the high pressure/low heat flux case discussed above.

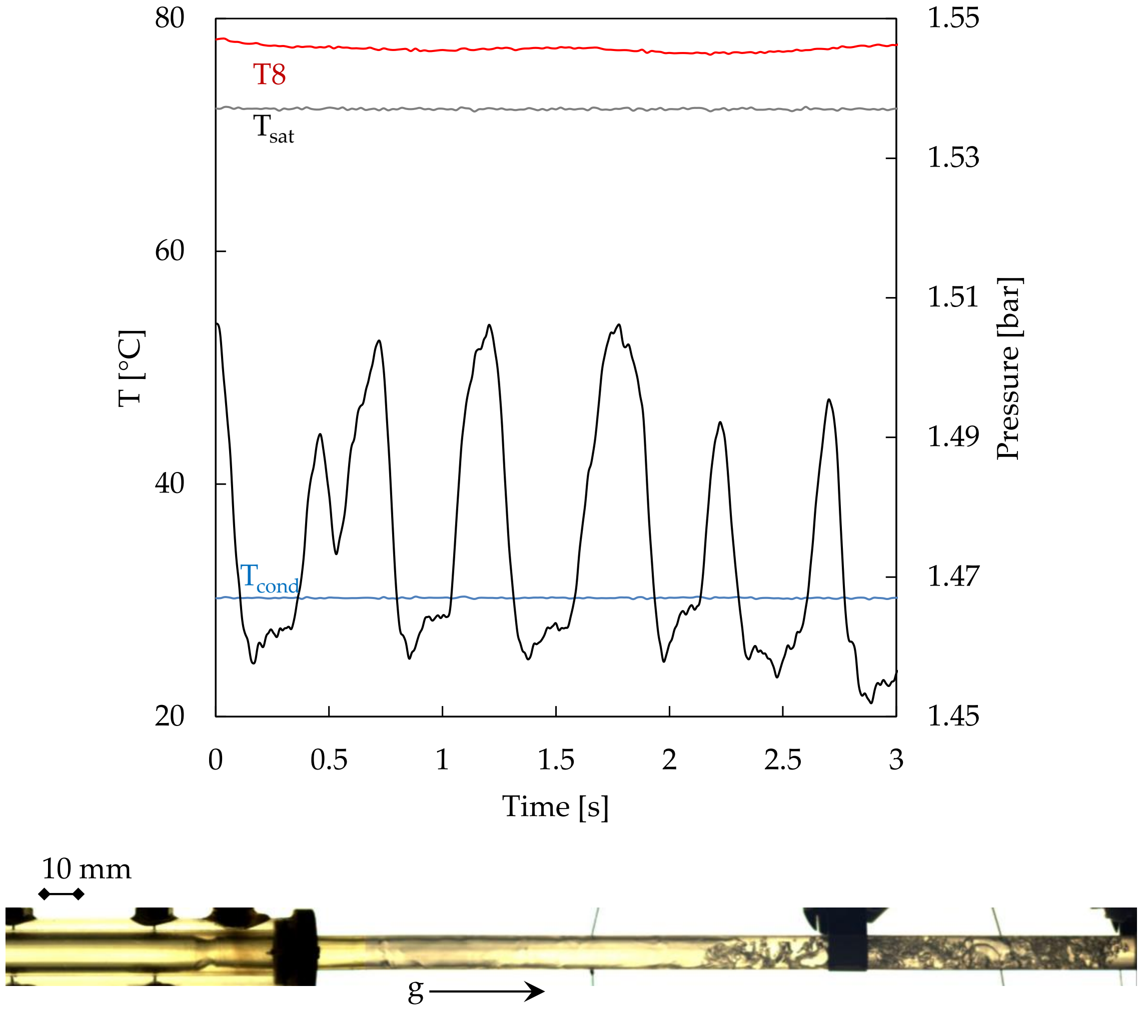

Figure 4.39 - Temperature and pressure trace and high-speed image, ethanol, $P_r = 0.02$, $q = 17$ kW/m²

The fast production of small bubbles helps to break up the bulk fluid of the evaporator pool, and so less liquid is forced to the condenser section. It will be seen in Section 4.4.3 that this churn flow regime results in higher heat transfer coefficients. This is due to the fact that, in this regime, the vapour is free to rise to the condenser without trapping liquid. The condenser section is not blocked to heat transfer by a large liquid mass, and the evaporator section is subject to increased mixing which is conducive to improved heat transfer. The large fluctuation in the pressure measurement of Figure 4.39 is due to the compression of gas in the condenser section as the vapour rises from the evaporator. The fluctuations are exaggerated here as a result of the high vapour velocities at this high heat flux condition, while the temperature remains relatively steady.

4.4.2. Flow maps

The high-speed imaging in this investigation made it possible to create flow pattern maps using the flow regimes observed in the thermosyphon for each of the working fluids over the range of pressures tested. The maps presented in this section are similar to that of Figure 4.4. However, these maps use the liquid and vapour momentum flux, *p*, as the coordinate system, similar to flow regime maps developed in previous studies [60]. This coordinate system was chosen as it will be more convenient in the context of the heat transfer analysis of Section 4.5.2. Figure 4.40 shows the flow patterns observed in the evaporator section. Figure 4.41 illustrates how the evaporator flow regimes impact that in the condenser. It should be noted that the transition lines in these maps are for demonstration purposes and should be taken purely as a guide.

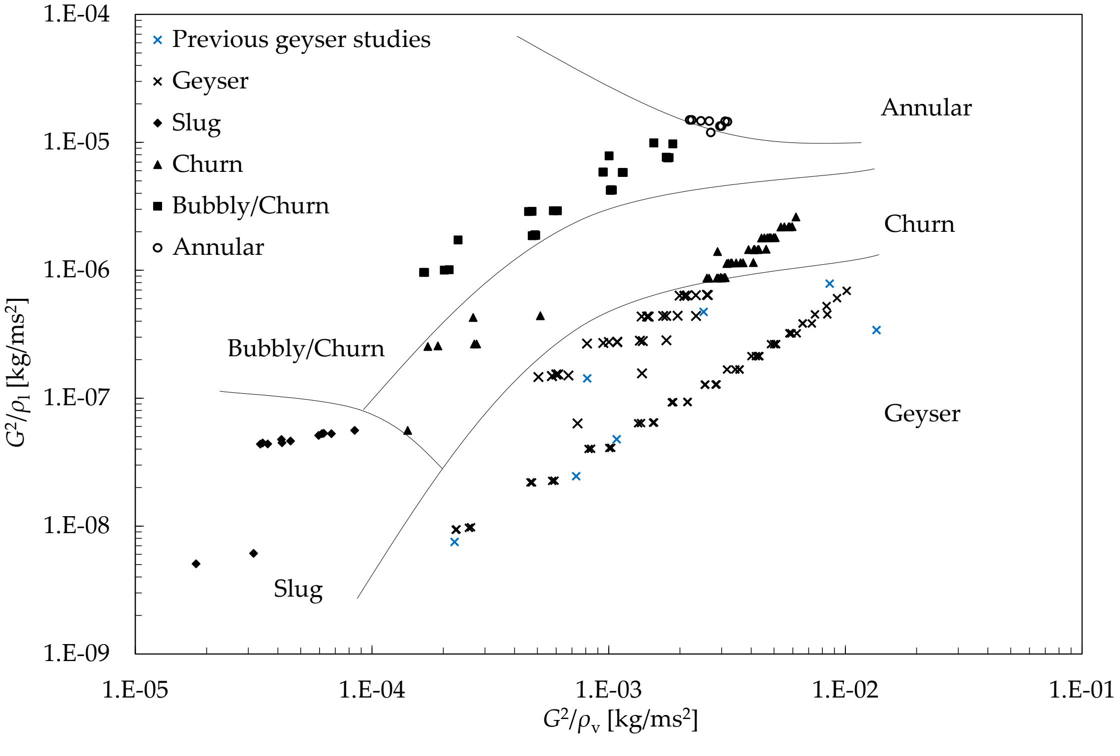

Figure 4.40 - Flow pattern map for evaporator section, momentum flux coordinates

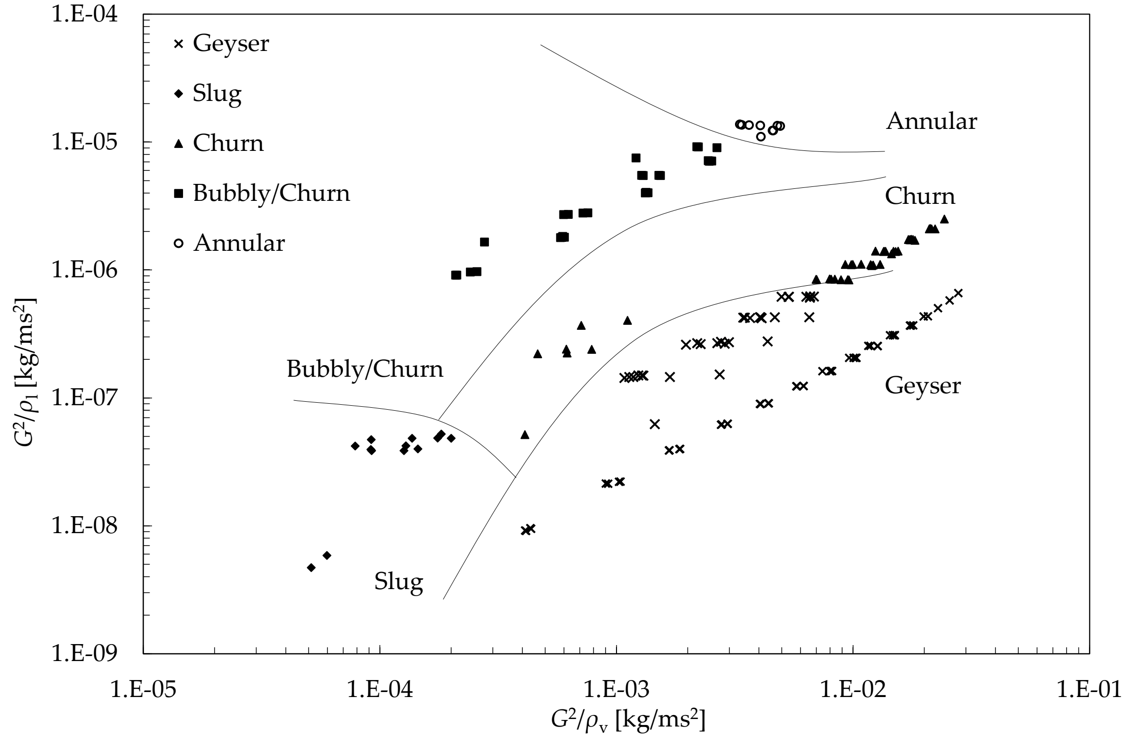

Figure 4.41 - Flow pattern map condenser section, momentum flux coordinates

Figure 4.40 contains five distinct regimes: geyser, slug, churn, bubbly/churn and annular. Each of these regimes were encountered and outlined in detail previously in Section 4.4.1. The physical transition from one regime to another is dominated by the vapour momentum flux, except for the case of bubbly/churn, where the liquid component plays a role. At low liquid and vapour momentum flux levels, slug flow is dominant where small bubbles rise relatively slowly in the evaporator, typically coalescing to form a larger vapour mass. At higher levels of liquid momentum flux, more churn takes place in the evaporator and the larger bubbles are disturbed, creating smaller bubble sizes and more mixing.

Geyser boiling dominates at low liquid momentum flux but high vapour momentum flux. The high vapour flow rates here act to force the liquid upwards towards the condenser section. The blue markers in Figure 4.40 represent existing geyser boiling data literature for both ethanol and water working fluids using references [18], [24], [45], [47], [50]. As the liquid momentum flux is increased the flow transitions from geyser to a churn regime where there is a high degree of phase mixing evident. Entrainment effects may also start to become apparent in the churn regime. Further increases in the liquid momentum flux result in annular-type flow where only a thin film remains in the evaporator. This regime was only observed for the case of HFE-7000 at high levels of heat flux, as shown in Section 4.4.1.5. Most of the working fluid from the evaporator was held up by the high liquid and vapour momentum. An increase in heat flux from this regime resulted in dryout of the evaporator section.

4.4.3. Summary

It is clear from these working fluid studies that the fluid properties can have an impact on the two-phase flow and associated heat transfer of the thermosyphon. This is mostly due to the interactions between the channel and the fluid at small dimensions and rate of vapour production. From an applications standpoint, avoidance of geyser-like oscillations that were observed both in Chapter 3 and for the case of water and ethanol at low pressures in this chapter would be most beneficial to ensure safe, reliable and consistent operation of the cooling device. The tests have shown that working fluid and channel dimension must be carefully considered for individual thermosyphon design and operating conditions, in order to avoid these oscillations.

4.5. Results and discussion – Heat transfer analysis

The analysis of the heat transfer performance of the thermosyphon is presented in terms of the measured heat transfer coefficient for each section. The heat transferred between the evaporator and condenser sections will vary for each of the fluids tested and at different imposed heat fluxes due to the nature of the flow and experimental conditions. As seen in Section 4.4, the flow regimes vary significantly between each of the liquids with heat flux, and this has a significant effect on the mechanisms of the heat transfer within the thermosyphon.

4.5.1. Temperature distribution

Figure 4.42 shows the average temperatures for each of the thermocouples along the length of the thermosyphon for the lowest level of pressure tested for each fluid. The spatial uniformity of the average temperature in the evaporator in the case of the HFE-7000 is noticeable from this figure, indicating a high degree of phase change and induced mixing in the evaporator and condenser section. As outlined in Section 4.4, this type of heat transfer is more prominent in cases where confinement is not significant. The following discussion will first focus on the low pressure experimental conditions, where confined, geyser-type boiling was dominant for both water and ethanol.

For the case of water and ethanol there is less uniformity in the temperature of the evaporator section. This is due to the transient behaviour, where the evaporator is subject to oscillations and possibly temporary dryout conditions, which is typical of confined boiling behaviour. It can also be noted from this graph that there is a difference in the average temperature between the upper (T10 & T11) and lower (T8 & T9) evaporator sections for water and ethanol test cases. This is a result of the continual presence of a liquid pool in the lower evaporator section, whereas the upper thermocouples were subject to change based on the height of the remaining liquid pool in the evaporator section.

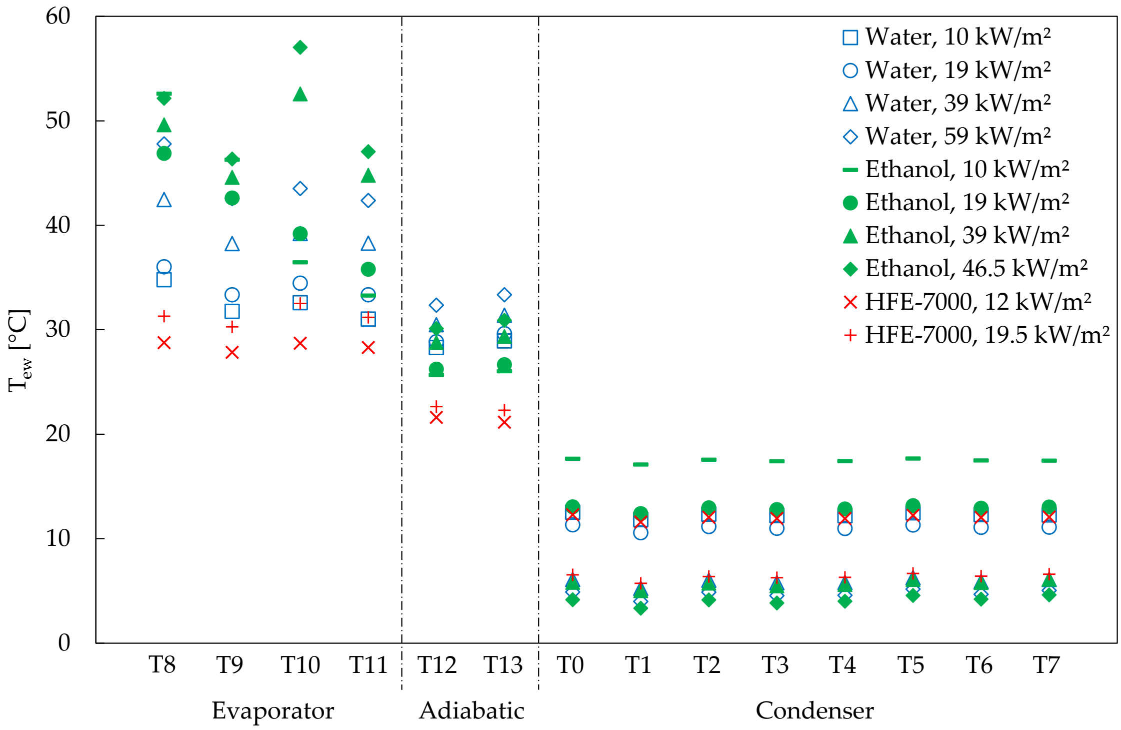

Figure 4.42 - Temperature per section along thermosyphon length, low pressure condition

In tests where the liquid pool height was sufficient to cover the lower thermocouples, a lower temperature was recorded in these regions. For cases where the liquid pool was depleted to below these thermocouples, an increase in temperature was recorded. Therefore, this temperature difference will change as the heat flux is increased due to the higher levels of vapour production leading to liquid hold-up and reduction of the liquid pool height.

There is a temperature increase across the left and right sides of the tube, shown in Figure 4.42. Thermocouples T8 and T10 tended to record higher temperatures than T9 and T11. It was observed there was an increase liquid tendency to flow down one side of the evaporator in rivulets, resulting in a lower temperature recorded in that side of the evaporator. The surface effect causing this behaviour is yet unknown, but it is possibly caused by surface roughness inhomogeneity between each side of the thermosyphon.

The results outlined are consistent with the oscillatory and confined flow behaviour visually observed in the evaporator section for the water and ethanol test cases. Further confirmation of this behaviour is evident in analysing the temperature fluctuations within the evaporator by calculating the difference between the maximum and minimum temperatures recorded in one of the upper (T10) and lower (T8) evaporator thermocouples. Figure 4.43 presents the difference between the maximum and minimum temperatures recorded in the upper and lower sections of the evaporator, and gives an indication of the amplitude of the temperature fluctuations. HFE-7000 showed only small oscillations in temperature in both the upper and lower thermocouples (except at the highest levels of heat flux where failure occurred). Water and ethanol showed varying degrees of oscillation in the upper and lower sections, changing with heat flux. Notably, there is a change in the magnitude of oscillations at around q = 25 kW/m². This is consistent with the FFT analysis of the temperatures for the case of ethanol, presented in Section 4.4.1.8, Figure 4.29.

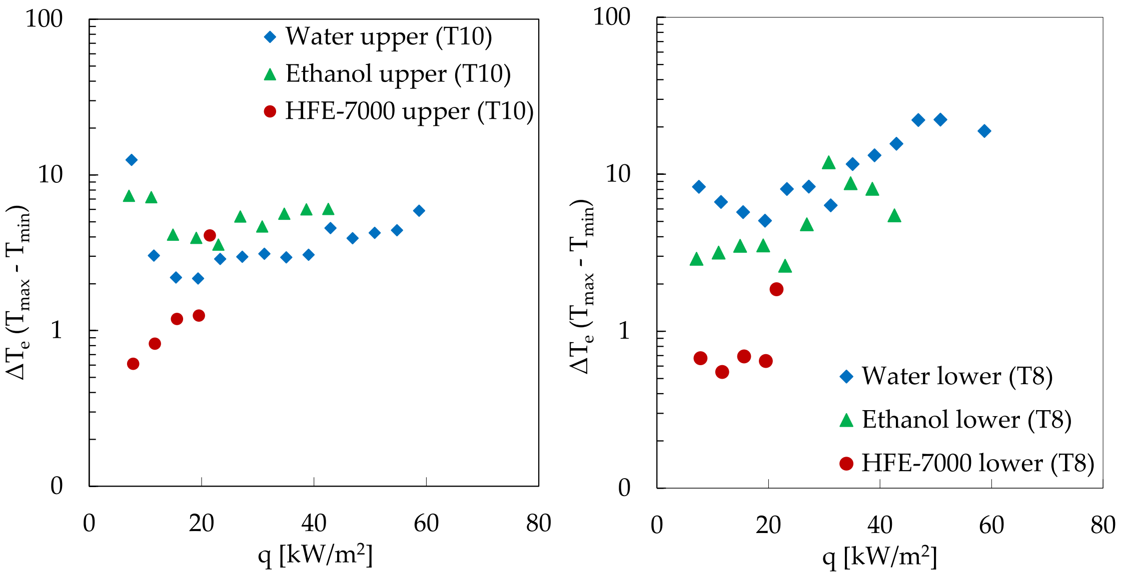

Figure 4.43 - Temperature flux for upper (T10) and lower (T8) thermocouple

For the case of the upper thermocouple, the temperature oscillations recorded for water and ethanol were larger than HFE-7000, and are most noticeable at lower heat fluxes. The oscillatory behaviour in this instance consisted mostly of quiet phases as the liquid pool refilled and reheated, followed by explosive boiling events where much of the working fluid was forced into the condenser section. This presented as a gradual rise in the upper evaporator temperature, followed by a sharp drop in temperature, accompanied by a spike in the pressure. As the heat flux in the evaporator section was increased, the duration of the quiet periods was shortened until it was no longer evident. This is noted by the steadying of the temperature difference in the upper thermocouple as the oscillations are so regular there is consistent rewetting in this section. The thermosyphon enters a transient regime, the temperature oscillations decrease in amplitude and increase in frequency above q = 25 kW/m^2.

The lower thermocouple, T8, shows differing behaviour for water and ethanol at low heat flux levels. However, both are significantly higher than the temperature difference of HFE-7000, which was consistent with the flow regimes observed for confined/unconfined flows. At low heat flux levels, for the case of water the temperature difference in the lower evaporator section is higher than that of ethanol. This result is due to a change in the location of bubble nucleation between the two fluids. As is evident in the water images presented in Section 4.4.1, it is generally the case that bubble nucleation in water took place deep in the liquid pool of the evaporator. This nucleation location resulted in less fluid in the region of the lower thermocouple and it experienced a higher superheat between boiling events. For ethanol, the temperature difference in the lower evaporator temperature is slightly lower than water due to the presence of a continuous liquid pool in this region. Bubble nucleation in the ethanol case was located higher in the evaporator pool.

For both water and ethanol, as the heat flux is increased to q = 25 kW/m^2, the temperature difference in the lower evaporator increased. This was due to the reducing size of the liquid pool. With increasing heat flux, more liquid hold-up was evident in the condenser section due to an increase in the rate of vapour production. This resulted in periodic drying of the lower evaporator thermocouple as the liquid was drained and refilled. Interestingly, for the lower evaporator temperature difference in Figure 4.43, there is a change in behaviour of ethanol at q = 27 kW/m^2. Here, a sharp increase in the temperature difference is apparent for the lower section thermocouple. As noted in the flow maps of Section 4.4.1.8, there was a change in the behaviour of ethanol from geyser to churn boiling as the heat flux was increased. The quiet periods between boiling events were no longer distinguishable and the boiling became more rigorous.

The analysis of the evaporator temperatures in this way confirms that the flow behaviour observed in the preceding section influences the heat transfer of the thermosyphon. Oscillatory behaviour is present using water and ethanol as the working fluid due to confined flow and high vapour production rates. The change in flow behaviour of ethanol at higher heat fluxes is also confirmed by a change in temperature measurements of ethanol. The steady boiling behaviour of HFE-7000 is noted in the temperature measurements and temperature differences between the thermocouples in the evaporator.

4.5.2. Heat transfer analysis

The heat transfer coefficient is used to quantify the effectiveness of the thermal transport within the thermosyphon. Here, it represents the ratio of the heat flux and the temperature difference between the thermosyphon wall surface (source) and working fluid (sink).

First, the heat transfer coefficient in the evaporator section for each fluid was compared to the pool boiling correlation proposed by Imura [31], Eqn. (4.13). The Imura correlation, as mentioned in Chapter 2, was developed for pool boiling in thermosyphons. This correlation has been well documented in previous literature to perform accurately and for this reason it will be used as the reference correlation in the following discussion. Figure 4.44 shows a comparison of the experimental heat transfer coefficients in the evaporator section over the range of experimental conditions, for each fluid.

$$h_e = 0.32\left(\frac{\rho_l^{0.65}k_l^{0.3}C_{pl}^{0.7}g^{0.2}}{\rho_v^{0.25}h_{fg}^{0.4}\mu_l^{0.1}}\right)\left(\frac{P_v}{P_{atm}}\right)^{0.3}q^{0.4} \qquad \textbf{Eqn. (4.13)}$$

Since it has clearly been established that the flow regimes and heat transfer coefficients are significantly linked in the performance of a thermosyphon, the flow regimes and heat transfer coefficients should be considered in conjunction with one another. With this in mind, the heat transfer trends of Figure 4.44 will be considered in conjunction with the flow maps of Section 4.4.2.

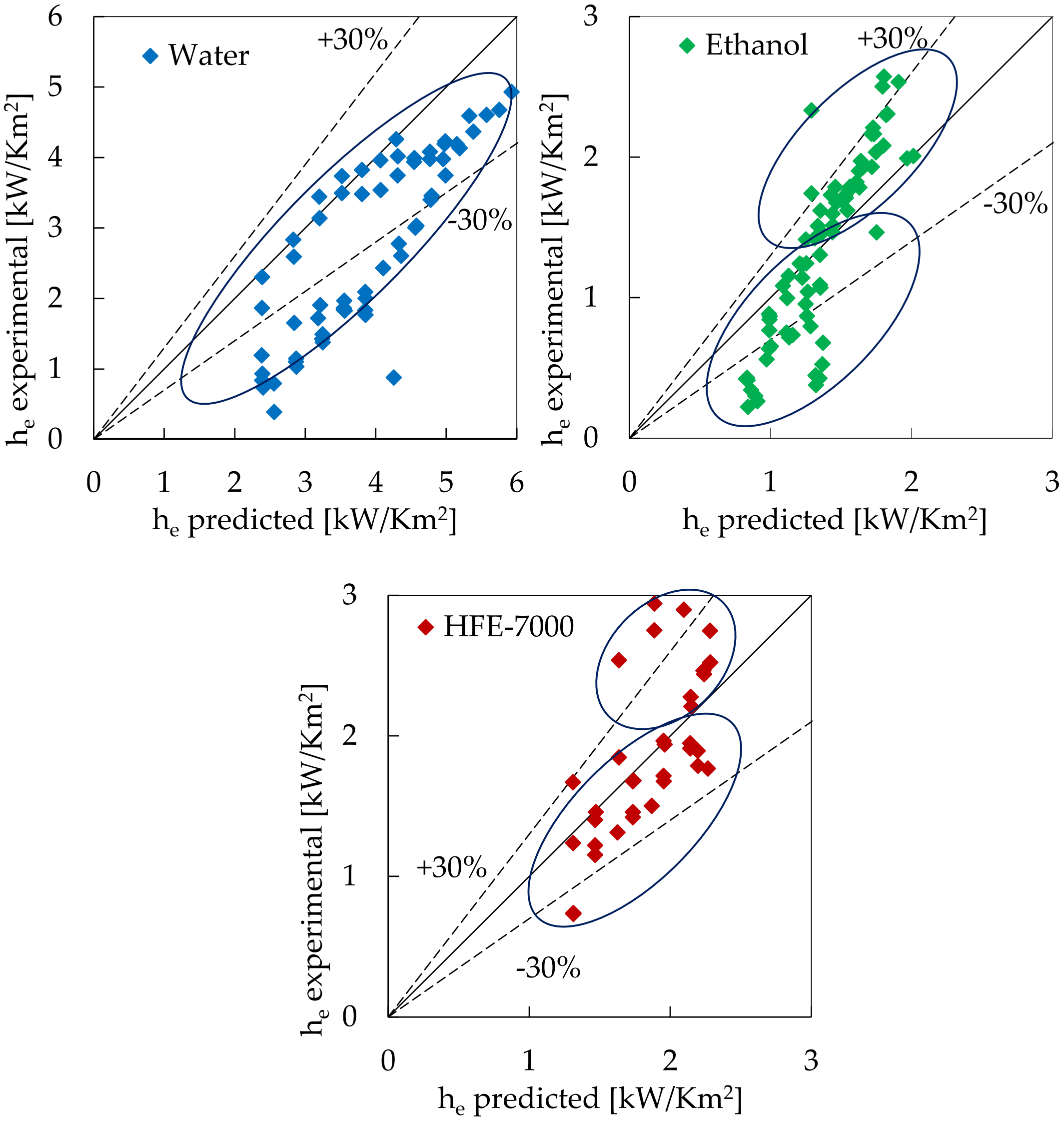

Figure 4.44 - Evaporator heat transfer coefficient for each liquid compared to Imura correlation [31]

For the case of water, Figure 4.44 shows that the Imura correlation over-predicts the measured heat transfer coefficient of the evaporator section. This is due to the dominant geyser boiling mechanism occurring, as highlighted in Figure 4.45. As observed in Section 4.4.1, the geyser boiling regime differs from nucleate pool boiling as heat is transferred as a mixture of latent and sensible heat. The heat transfer coefficient associated with geyser boiling is lower than that of nucleate pool boiling, as seen here in Figure 4.44. It is evident from Figure 4.45 that as the vapour momentum flux is increased the heat transfer coefficient of the evaporator improves due to the higher rates of vapour production.

The heat transfer coefficients for the other observed regimes are also presented in Figure 4.45 for water. The slug/churn regime observed for the case of water at high pressure and high heat flux presented the more favourable condition in terms of the heat transfer coefficient compared to flow regimes at lower momentum flux levels, such as slug flow. The increased mixing of this regime, combined with the steadier behaviour, resulted in an increase in latent heat transfer, and the heat transfer coefficients move closer to that of the pool boiling prediction. At high pressures and low heat flux, during the slug regime, the heat transfer is poor due to the low vapour production rate, low mass transfer rates and less aggressive mixing of the phases in the evaporator.

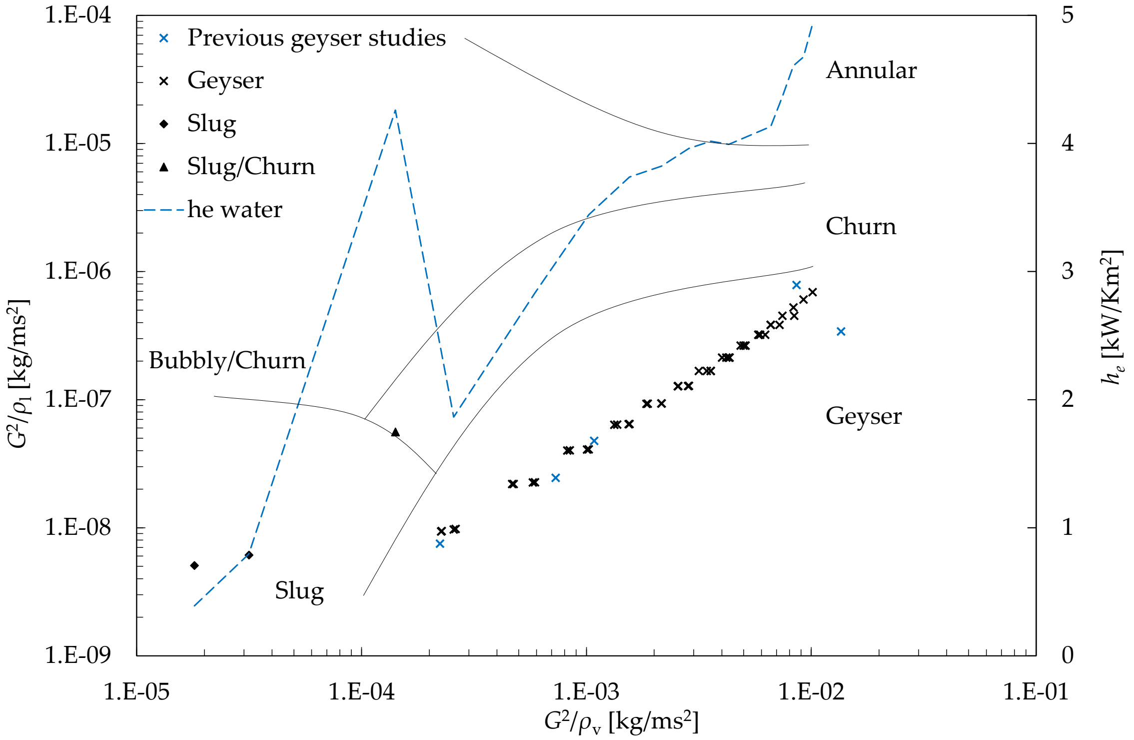

Figure 4.45 - Water evaporator flow map and measured heat transfer coefficient

For the case of ethanol, a number of different flow regimes were observed and discussed in Section 4.4.1. With this in mind, a split in the prediction results is highlighted in Figure 4.44. This split corresponds to regions where the pool boiling correlation over-predicts the measured heat transfer coefficient, but provides reasonable agreement/under-prediction for the upper data set. The measured heat transfer coefficient in the context of these different flow regimes is shown in Figure 4.46. Similar to water, the geyser regime is present for the case of ethanol at low pressure and low heat flux levels. Again, it is clear from Figure 4.46 that this regime deteriorates the heat transfer coefficient.

There is a transition in the flow regimes from geyser to churn at high levels of heat flux, as discussed in Section 4.4.1. This change in behaviour is also evident in Figure 4.43, Section 4.5.1, where the oscillations of the evaporator wall temperature reduce. The change in behaviour is noted in the flow regime transition and corresponding increase in the slope of the heat transfer coefficient for ethanol, shown in Figure 4.46.

During this churn regime, there is increased mixing due to higher vapour production rates and relatively high confinement levels. The boiling regime is not the same as that of nucleate pool boiling, and this explains the under-prediction of the Imura correlation of the upper data set highlighted in Figure 4.44.

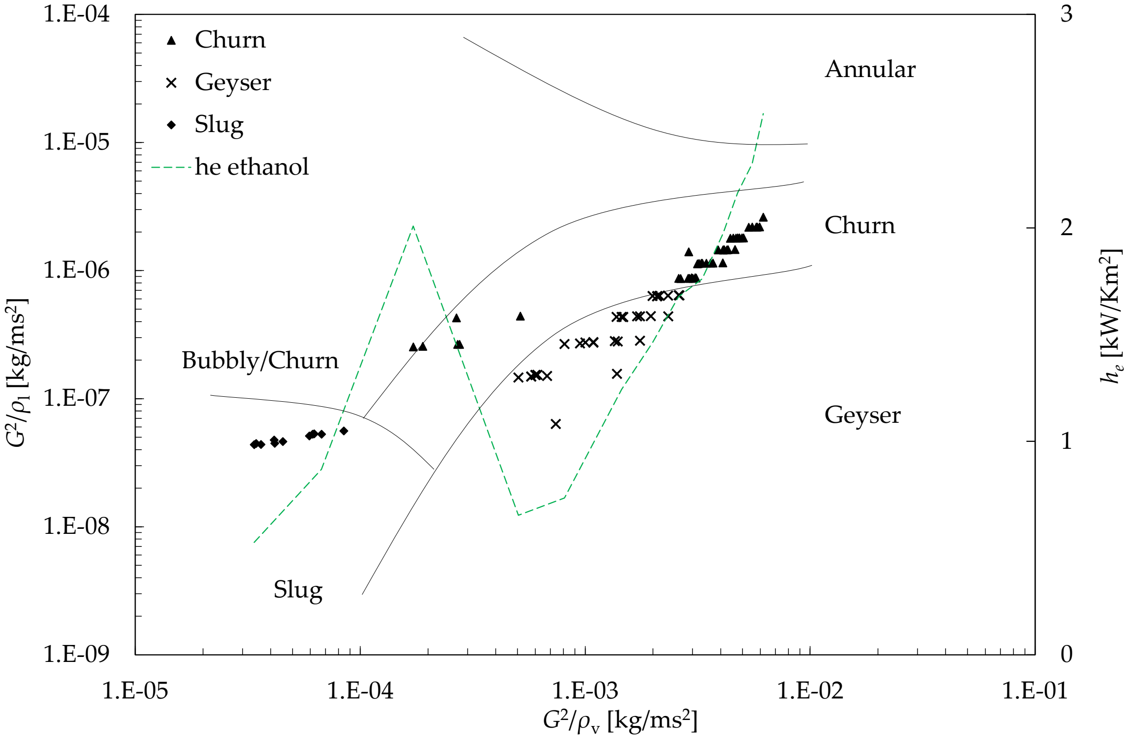

Figure 4.46 - Ethanol evaporator flow map and measured heat transfer coefficient

HFE-7000 shows the best agreement with the Imura pool boiling correlation in Figure 4.44. This is consistent with the observation that the HFE-7000 showed nucleate pool boiling behaviour, as discussed in Section 4.4.1. At higher levels of heat flux, HFE-7000 presented an annular-type regime with a thin film falling down the evaporator wall.

The heat transfer coefficients related to these flow regimes are shown in Figure 4.47. Here a change in the slope of the heat transfer coefficient curve is evident as the flow regime transitions from bubbly to a more annular flow regime. Higher heat transfer coefficients are expected in this regime as higher vapour production rates promote mixing and the thin liquid film in the evaporator section results in enhanced heat transfer. Within this regime, the heat transfer is better than that predicted by the Imura correlation, as shown in Figure 4.44.

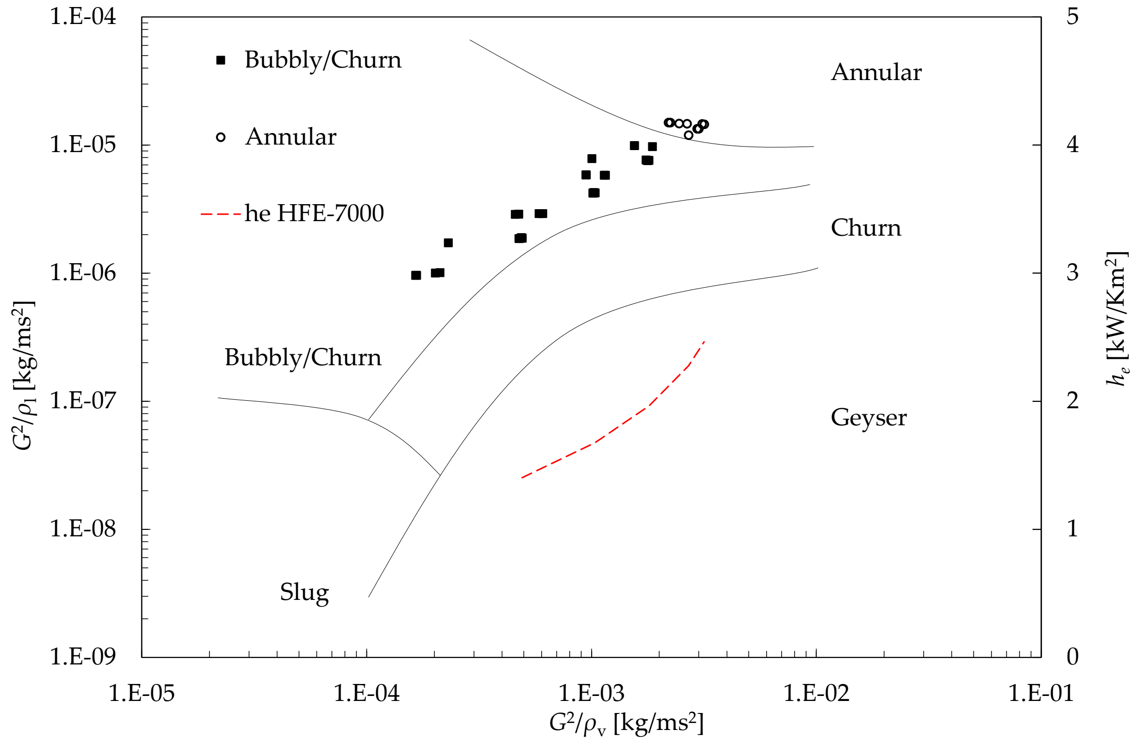

Figure 4.47 - HFE-7000 evaporator flow map and measured heat transfer coefficient

In terms of the heat transfer in the condenser section, there are also large discrepancies evident between the predicted and measured values, as shown in Figure 4.48. In this section the heat transfer is predicted using the Nusselt falling film condensation correlation, Eqn. (4.14), as a reference.

$$h_{Nusselt} = 0.943\left\{\frac{\rho_l(\rho_l-\rho_v)gk_l^3\left[h_{fg}+0.68C_{pl}(T_v-T_c)\right]}{\mu_l(T_v-T_c)L_c}\right\}^{0.25}$$ **Eqn. (4.14)**

For the case of water, the heat transfer coefficient in the condenser was significantly over-predicted by the Nusselt equation (up to tenfold). Nusselt's equation correlated better with the HFE-7000 and ethanol data (± 40 %); the measured values being under-predicted in both of these fluid cases. The discrepancies in the measured and predicted values are due to the flow regimes observed for each of the working fluids.

In the case of water, the heat transfer coefficient in the condenser measured during the tests is much lower than that predicted, as there was no thin film condensation observed in this section during these test conditions. A large amount of liquid in the condenser will result in stunted heat transfer in this section. As a result, the heat transfer coefficients are lower than those predicted using the Nusselt correlation. Despite the thermosyphon-specific modifications made to the condensation heat transfer coefficient by [23], this correlation showed no better agreement with the experimental data compared to the Nusselt equation.

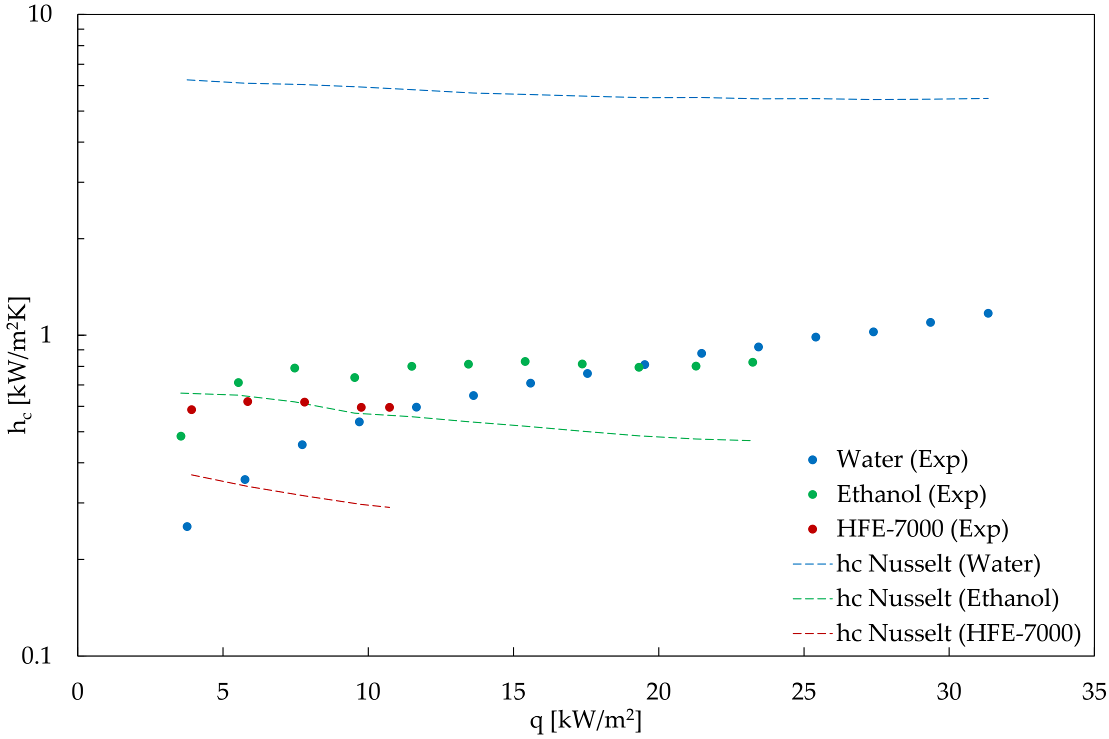

Figure 4.48 - Condenser heat transfer coefficient and Nusselt correlation

For the ethanol and HFE-7000 working fluids, the experimental data is under-predicted to the same extent, but within the same order of magnitude as the predictions. For these test cases there is evidence of a liquid falling film in the condenser section. For the case of ethanol, the bulk fluid motion caused by the geysering behaviour is interrupted in the condenser section, and the liquid plugs are broken, resulting is a smooth film flow of liquid returning to the evaporator in the condenser section. As observed in Section 4.4.1.5, images of the HFE-7000 operated thermosyphon show a continuous liquid film in the condenser section.

In terms of the flow regimes in the condenser region, the heat transfer coefficient of water and ethanol are presented with the flow regime map in Figure 4.49. Again this graph shows low values of heat transfer coefficient during slug flow regimes.

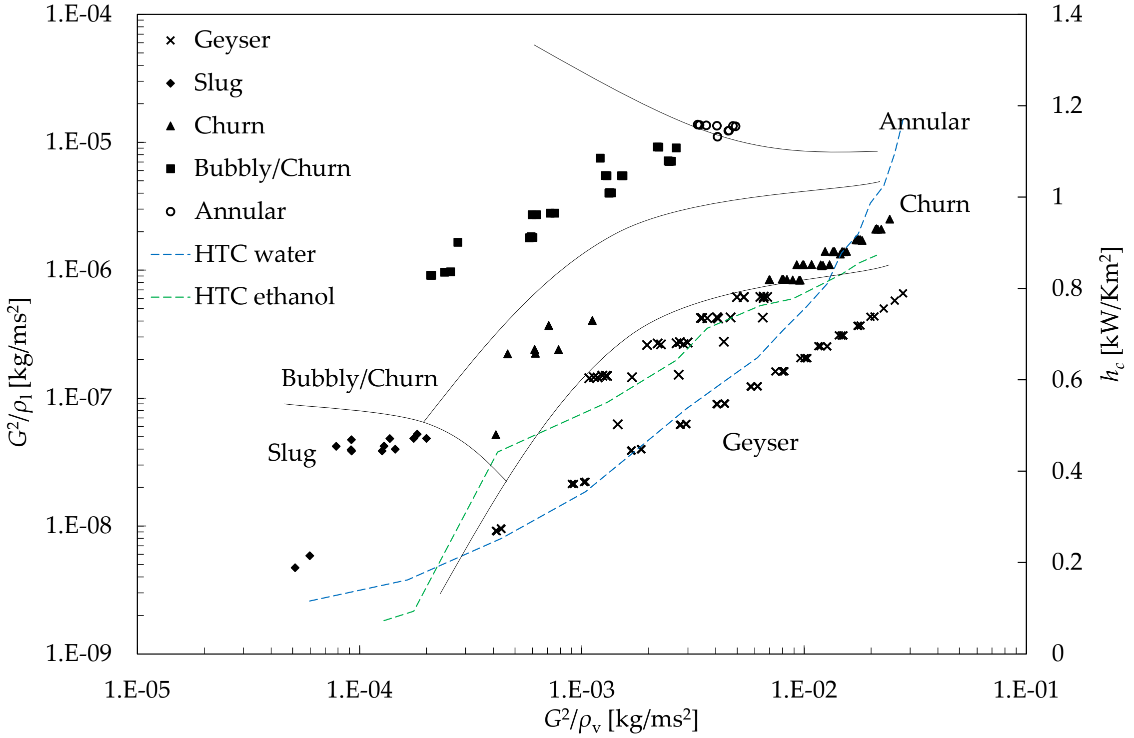

Figure 4.49 - Condenser flow map and heat transfer coefficients of ethanol and water

For ethanol, at lower pressures during the geyser boiling regime there is an increase in the heat transfer coefficient. This is followed by a steady increase in heat transfer coefficient with increasing heat flux. For water, the heat transfer coefficient increases in a different trend with heat flux during the geyser boiling regime. It is thought that this is due to the difference in liquid plugs between the water and ethanol geyser boiling regimes. The surface tension forces of water are high enough to maintain the liquid in a complete column suspended by the vapour in the condenser section, reducing the heat transfer in this region. Conversely, ethanol has lower surface tension forces which can be overcome by the expanding vapour during confined boiling. The liquid plugs cannot be sustained and a thick liquid film is formed in the condenser section, resulting in an increase in the heat transfer coefficient.

This study highlights the connection between the flow regimes observed and the measured heat transfer coefficients and their combined impact on the thermal performance of the thermosyphon. The changes observed in the flow regimes for each of the fluids provide an insight into the changes in measured heat transfer coefficient trends.

4.6. Conclusion

The aims of this investigation were to observe and characterise the flow regimes and associated heat transfer occurring within a thermosyphon of relatively small dimension. The investigation focussed on flow regimes particular to small dimension channels which were found to deviate from the conventional nucleate pool boiling behaviour expected in thermosyphon operation. The main results of this study are itemised as follows:

- The boiling mechanisms in the thermosyphon of this study are dominated by gravitational forces, as opposed to surface tension and inertia forces.
- Within the gravity-dominated thermosyphon, the two-phase flow regime is influenced by confinement and the rate of vapour production.
- The flow regimes can be classified in terms of the degree of confinement of the fluid and rate of the vapour superficial velocity. The resulting flow regimes dictate heat transfer performance of the thermosyphon.
- For high levels of confinement and low rates of vapour production, the flow is characterised as slug/plug flow. With relatively high confinement combined with high vapour production rates, a geyser boiling regime is encountered.
- For unconfined flows, a nucleate pool boiling regime is present in the evaporator at low vapour production rates. This regime becomes progressively more churn-like with increasing rates of vapour production.
- With very high rates of vapour production and unconfined flows, an annular flow regime can be encountered where most of the liquid is held above the evaporator and a thin film falls down the evaporator wall.
- HFE-7000 shows the most stable flow behaviour for all pressure and heat input levels under investigation, due to the fact that it is unconfined, even with relatively high rates of vapour production. Due to the steadiness of operation, and

favourable boiling regimes, HFE-7000 showed relatively high heat transfer coefficients at low pressures.

- The churn regimes observed for both HFE-7000 and ethanol presented the most favourable conditions in terms of effective heat transfer. The oscillatory geyser boiling regime showed a reduction in the heat transfer coefficient at low input heat flux, but this gradually improved with increasing heat flux as the rate of vapour production, and thus the frequency of oscillation, increased.
- Failure of the thermosyphon was, in most cases, due to the increasing rate of vapour production at high input heat flux. This led to increased liquid hold-up in the adiabatic and condenser regions and subsequent dryout of the evaporator section.
- Geyser boiling is a prominent behaviour for water and ethanol, especially at low operating pressures. This is mainly due to high surface tension and high vapour specific volume which led to high levels of confinement and high superficial vapour velocities.

For steady and predictable heat transfer performance, the geyser boiling regime should be avoided as the large pressure fluctuations could pose a threat to the thermosyphon equipment. However, this regime did not present a significant deficit in terms of the heat transfer capability of the thermosyphon. Maintaining the operation of the thermosyphon within the churn or bubbly regime will result in a more reliable performance. This result is beneficial in terms of electronic cooling applications. Further to this, the augmentation of the flow regimes using external forces could enable smart control of the thermal output of the thermosyphon, which will be investigated in the following chapter.

5. Flow augmentation using Electrohydrodynamics

5.1. Introduction

From the previous chapters of this thesis it is clear that there are strong links between the flow regimes and the mechanisms of heat transfer within the thermosyphon system. Identifying the most effective regimes of both heat and fluid transport are therefore vital in designing an optimal system. Opportunities to augment the flow within the thermosyphon could be utilised to enhance the transfer of heat between the source and the sink.

Electrohydrodynamics (EHD) involves the application of electric fields to fluids. EHD forces have been studied in two-phase systems, including convective flow boiling enhancement [63 – 65]. Charging the system with an electric field can dramatically augment the flow, and thus the heat transfer. This augmentation is due to the imposed body forces on the fluid in the presence of an electric field, shown in Eqn. (5.1). These electric body forces act to alter the bulk fluid behaviour and also the interaction of phases at the liquid-vapour interface.

$$f_e = \rho_{ei}\bar{E} - \frac{1}{2}E^2\nabla\varepsilon + \frac{1}{2}\nabla\left[\rho E^2\left(\frac{\delta\varepsilon}{\delta\rho}\right)_T\right] \qquad \textbf{Eqn. (5.1)}$$

The three components of this expression are the electrophoretic, dielectrophoretic and electrostrictive forces. Each of these components contributes to the flow augmentation in different ways.

The electrophoretic force, $\rho_e\bar{E}$, acts on the net free charge within the fluid promoting bulk mixing within the liquid and vapour phases. The second term, the dielectrophoretic force, can be most significant in two-phase flows. This force is due to the difference in permittivity between the liquid and vapour phases. At the liquid-vapour interface, this permittivity gradient can have significant effects on the heat transfer as a result of phase redistribution. Generally, the liquid phase has a higher permittivity than that of the vapour, and is pulled toward regions of high electric field strength. This behaviour is referred to as liquid extraction, while the vapour phase is repelled. In two-phase flow scenarios this can result in liquid being pulled from the channel wall, enhancing mixing of the phases, and consequently increasing the rate of heat transfer. The final term in the expression, the electrostrictive force, accounts for variation of the permittivity with changing density and temperature. Of these three terms it is thought that the second is the most dominant for two-phase flow conditions [66], though there exists some debate on this matter.

EHD has been shown to enhance convective boiling in a number of ways. The electric forces increase the number of nucleation sites, the frequency of bubble departure, and the bubble size [67]. In this way, EHD forces result in an improvement of the heat transfer by inducing a more vigorous nucleate boiling regime. As mentioned above, the redistribution of the flow due to liquid extraction augments the bulk fluid motion. The liquid is attracted to locations of high electric field, and vapour is repelled. This is particularly important for horizontal flow cases where liquid flow is agitated enough to wet both the top and bottom of the channel, increasing the heat transfer in these regions. It has also been found that the level of heat transfer enhancement is proportional to the applied high voltage, but inversely proportional to the working fluid flow rate and applied heat flux [66 – 68].

5.2. Literature review

5.2.1. Electrohydrodynamic augmentation of flow boiling

Two-phase flow augmentation due to EHD has been studied over a wide range of applications. Comprehensive review studies of EHD in two-phase applications has been compiled by Allen and Karayiannis [69] and more recently by Laohalertdecha *et al.* [70]. Much of the analysis to date has been focussed on two-phase flow boiling augmentation using both A.C. and D.C. electric fields, generally in the horizontal orientation. Varying levels of enhancement of the average heat transfer coefficient have been reported in the existing literature.

Cotton *et al.* [66] investigated the influence of applied D.C. electric fields in flow boiling using HFC-134a as the working fluid. A flow pattern map was developed for the regimes induced by an applied high voltage of 0 – 8 kV. A dimensionless analysis was also carried out using dimensionless numbers specific to EHD [71]. This study investigated the Masuda number, M_d, which characterises the body forces associated with EHD, (Eqn. (5.2)). It should be noted that the characteristic length, L, is the spacing gap between the concentric electrodes.

$$M_d = \frac{\varepsilon_0 E_0^2 L^2}{\rho_l \nu_l^2}$$ **Eqn. (5.2)**

It was found that the EHD body forces strongly influence the flow when they are large enough to overcome the inertial forces within the system. It was proposed that when $M_d \sim Re_l^2$ the EHD forces interfered significantly with the liquid phase, thus redistributing the flow. This phase redistribution affected both the observed flow regimes and rate of heat transfer. In addition to this, Cotton *et al.* [66] proposed a dimensionless number range over which the flow of liquid will be influenced by EHD forces, as $0.1 \leq M_d/Re_l^2 \leq 1$.

A recent study by McGranaghan and Robinson [65] investigated the effects of EHD on horizontal flow boiling with full visualisation of the test section. HFE-7000 was used as the working fluid and EHD effects were investigated for an applied 60 Hz A.C. sine waveform, up to of amplitude up to 8 kV. The results compared the heat transfer enhancement observed on the top and bottom surfaces of the channel. A maximum of 7-fold increase was observed in the top section due to improved mixing and disturbance of the liquid flow at low qualities due to EHD. It was also reported that the effects of applied voltage were small below 4 kV. This result corroborates with the dimensionless correlation found by Cotton *et al.* [66]. At voltages above this threshold, the EHD forces were of the same magnitude as the inertial forces and the effects of EHD on the fluid flow became more prominent, i.e. when $M_d/Re_l^2 \sim 1$.

In a separate study, McGranaghan and Robinson [72] investigated the control of heat transfer output in an EHD flow boiling system. This was achieved by implementing a PID controller in addition to a high voltage amplifier. A specified rate of heat transfer could be reached by varying the electric field strength using the PID controller. The results demonstrated accurate control of the heat transfer to a particular level within a short time ($t \sim 120$ s) with small overshoot of the high voltage level.

The use of EHD for smart control of convective flow boiling was investigated recently by Nangle-Smith and Cotton [73]. The results of this study show that EHD can provide a fast response control mechanism for the steady state load condition. A controller was developed which was capable of maintaining the output load within ± 25 % of the desired conditions.

5.2.2. Electrohydrodynamics in heat pipe applications

A summary of EHD in heat pipe applications has been described by Reay and Kew [3], though sources of this study are very limited. Jones [74] studied EHD in a heat pipe using a ribbon electrode positioned eccentrically, similar in position to a wick structure in a conventional heat pipe. It was found that EHD forces could improve the performance of a heat pipe, mainly due to the phenomenon of phase redistribution. Loehrke and Sebtis [75] extended the investigation of EHD in heat pipes to flat plate designs. Viewing ports were placed in the evaporator, adiabatic and condenser sections to determine the fluid behaviour. An investigation of the influence of the electrode-plate spacing on the rate of heat transfer was carried out. It was found that heat transfer enhancement was observed for the lower values of spacing, however as the distance between the electrode and plate was increased, dryout failure was encountered. Loehrke and Day [76] furthered this work by presenting several EHD heat pipe designs with smooth and grooved inner walls. It was found that heat transfer enhancement was achieved for both cases, and that the inner wall structure did not have a significant effect on this enhancement. Similarly to Loehrke and Sebtis, Kikuchi *et al.* [77] studied the effects of EHD on a flat plate heat pipe. Some flow visualisation was carried out via observation windows along the length of the heat pipe and steady state nucleate boiling was observed in the evaporator.

5.2.3. Summary

From assessing the existing literature, it appears that full visualisation of the influence of EHD forces on the internal fluid dynamics within a thermosyphon has yet to be performed.

The aim of the current work is to carry out a preliminary investigation on the effects of EHD on a fully transparent, closed, two-phase thermosyphon of small dimension in the vertical orientation, with a concentric annular electrode. The focus will be to investigate a range of imposed heat fluxes in the evaporator, fluid fill volume, applied high voltage and frequency. Importantly, the study aims to corroborate the claims made in a recent patent application [78] where EHD is proposed as an innovative solution to control the effective thermal resistance of reflux-type thermosyphons.

5.3. Methodology

5.3.1. Experimental design

The experimental set-up outlined in Chapter 4 was modified to enable testing with the addition of a high voltage electric field. This allowed the investigation of the effect of Electrohydrodynamic (EHD) forces on thermosyphon operation with synchronized visual observation and thermal measurement. The experimental set-up for the EHD study is shown in Figure 5.1. HFE-7000 was chosen as the working fluid for these tests as it is an electrical insulator (dielectric strength ~ 40 kV) and has a high dielectric permittivity ($\varepsilon_r = 7.4$).

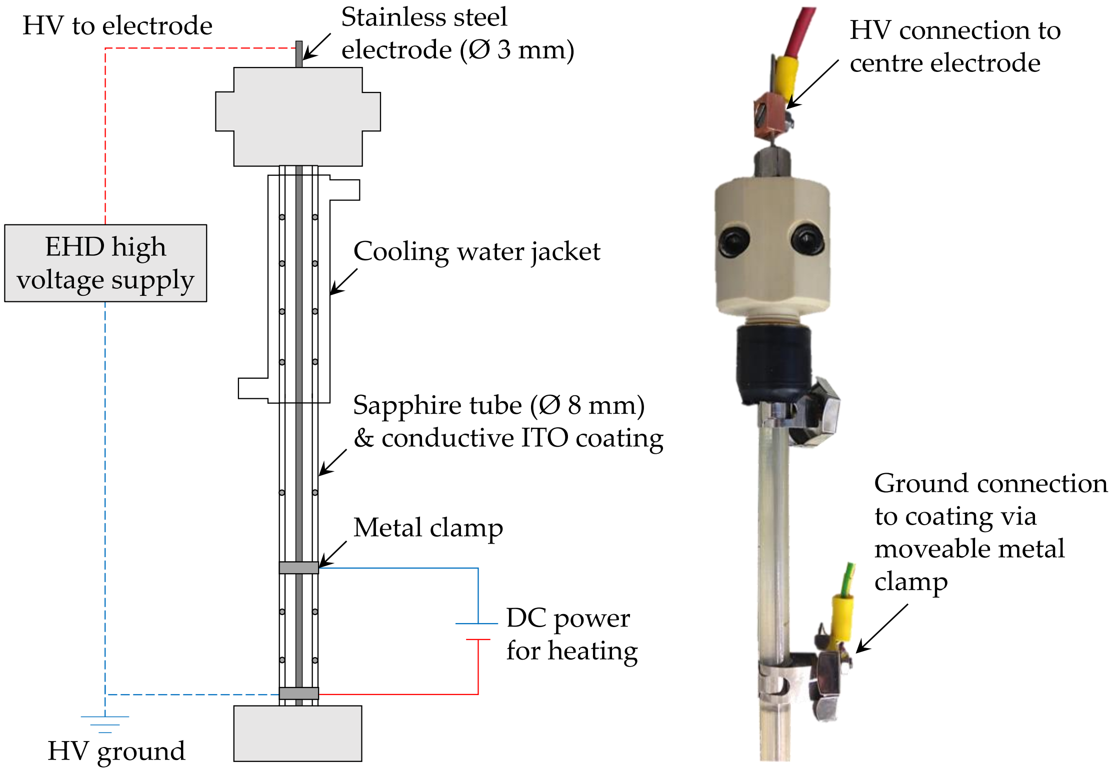

Figure 5.1 - Experimental set-up schematic, transparent thermosyphon showing representation of the high voltage connection

The PEEK support caps were modified so that they could support a 3 mm stainless steel electrode through the centre of the thermosyphon, as shown in Figure 5.1. Two stainless steel glands were used to secure the electrode into the support caps, ensuring the electrode was held taut and in place. In order to shield the exposed ends of the electrode, polycarbonate caps were manufactured which could be grounded for safety in order to prevent voltage arcing to other parts of the rig or equipment. Earth connections were also made to several points on the experimental set-up to prevent any charge build up. The ITO coating on the outer surface of the sapphire thermosyphon served as the other EHD electrode. The high voltage was connected to the apparatus that the electric field was through the entire length of the thermosyphon, as shown from the schematic in Figure 5.1. The high voltage connection to the electrode was made secure by copper fastenings manufactured specially to provide a secure connection between high voltage leads and the electrode.

5.3.2. Instrumentation

All thermocouples and pressure transducers used in the experimental apparatus detailed in Chapter 4 were left in place for this phase of testing. Additional equipment was used in order to generate and amplify the voltage supplied to the electrode in order to produce sufficient voltage to augment the liquid flow.

The EHD signals to the electrodes were applied using a TTi TG 1006 function generator which was used to generate sine waves between $V = 1 – 8$ V at $f = 20 – 100$ Hz. This signal was verified on an Iso-Tech IDS 8064 oscilloscope. This input signal was passed to a Matsusada AMT-10B10 high voltage amplifier, which outputs voltage signals at 1000 times amplification. An attenuator probe, Testec TT-HVP 40 (1000:1 signal attenuation) and multimeter was also used to verify the voltage transferred to the electrode at the output of the high voltage supply.

The output voltage from the high voltage amplifier (attenuated by 1000:1) was recorded in LabView along with the temperature and pressure of the system. High-speed imaging of the evaporator and condenser sections was carried out using two synchronised high-speed cameras, similar to the tests described in the previous chapter. The high-speed cameras recorded at a frame rate of 1000 frames per second and were triggered using LabView.

5.3.3. Testing methodology

Table 5.1 outlines the tests that were undertaken in this phase of investigation. HFE-7000 was used as the working fluid for all tests. For each case, the high voltage was applied across the entire length of the thermosyphon tube, and tests were carried out in 1 kV increments. All high voltage levels referred to in this study are peak-to-peak values.

Heat flux [kW/m^2]	**Waveform (Current)**	**Frequency [Hz]**			**Fill Volume [%]**		P_r	**Voltage [kV]**
8	Sine (AC)	20	60	100	50	100	0.5	0 – 8
15	Sine (AC)	20	60	100	50	100	0.5	0 – 8

Table 5.1 - Test parameter matrix for transparent thermosyphon with EHD

5.4. Results and discussion

This section will highlight the effects of EHD on thermosyphon performance in terms of the heat transfer coefficient in the evaporator section, evaporator superheats, and visual observations of the two-phase flow behaviour.

The presence of the concentric electrode within the thermosyphon will inevitably have an effect on the flow regimes and heat transfer observed. Appendix C. includes a comparison of the electrode and no-electrode case for HFE-7000.

As discussed in Chapter 4, the most dominant force acting on the thermosyphon is gravity. In order for the electric field to influence the flow behaviour within the thermosyphon it must first overcome this gravitational force. The electrogravitational number, N_{lg} (Eqn. (5.3)), expresses the ratio of electric forces and the gravitational forces [71]. As this number approaches unity, the electric forces will begin to augment the two-phase flow behaviour.

$$N_{lg} = \frac{\varepsilon_0 E_0^2}{\rho_l g L} \qquad \textbf{Eqn. (5.3)}$$

Table 5.2 lists the important dimensionless numbers for this investigation, along with the electric field strength, E. Here, it is evident that as the magnitude of the electric field is increased, the effect of EHD will become stronger as N_{lg} increases. The calculation of the electrogravitational force suggests that EHD forces will become significant at a voltage level greater than 4 kV, corresponding to $N_{lg} \geq 0.1$, and within the dimensionless number range described by Cotton *et al.* [66].

Voltage [kV]	**0**	**2**	**4**	**6**	**8**
Electric field strength [kV/m]	0	571.4	1142.9	1714.3	2285.5
Masuda Number, M_d	0	2.6×10^5	1×10^6	2.3×10^6	4.2×10^6
Electrogravitational number, N_{lg}	0	0.06	0.24	0.54	0.95

Table 5.2 - Dimensionless relationships for increasing applied high voltage

Figure 5.2 shows the superheat observed in the evaporator section for (a) low and (b) high heat flux levels. It is evident that different behaviour was occurring for each heat flux level. The rate of heat transfer was enhanced for low heat flux, $q = 8$ kW/m^2 for all levels of high voltage. At a heat flux of $q = 15$ kW/m^2 the heat transfer coefficient deteriorated with EHD. The presented results describe the heat transfer augmentation due to EHD forces on the thermosyphon in relation to both visual observation and heat transfer analysis.

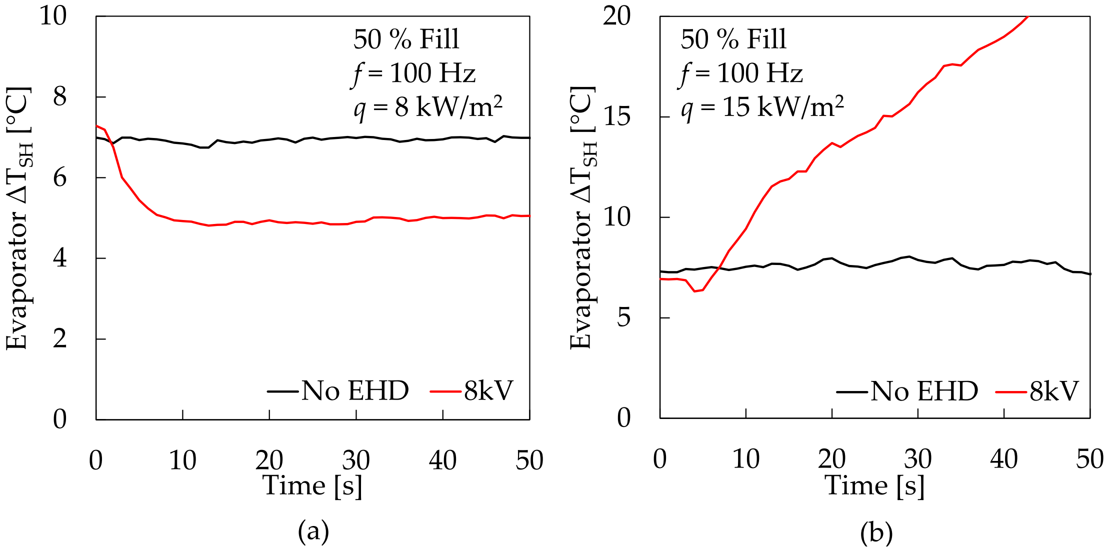

Figure 5.2 - Evaporator superheat with and without EHD (a) $q = 8$ kW/m^2 and (b) $q = 15$ kW/m^2

The difference in behaviour observed was related to the initial free-field flow regime occurring in the evaporator section. At the lower level of heat flux and $V = 0$ kV, there is a reduction in the rate of vapour production in the evaporator. Entrainment effects are evident, caused by the presence of the electrode in the vapour core. However, due to the relatively low vapour inertia the liquid does not reach the condenser section, as shown in Figure 5.3.

At higher levels of heat flux, and $V = 0$ kV, the vapour production rate has increased so that more of the liquid phase is held out of the evaporator section, as shown in Figure 5.4. A thin liquid film is present on the evaporator wall, and film evaporation is dominant in this region with nucleation events occurring in the liquid film.

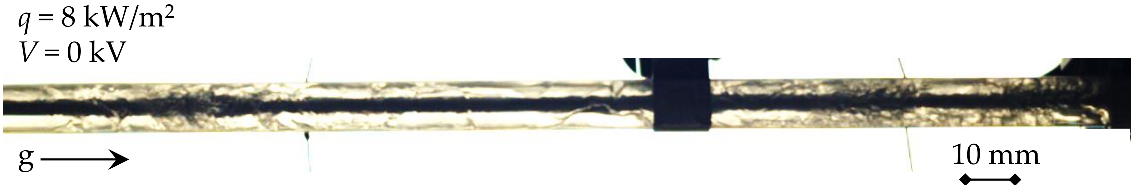

Figure 5.3 - Thermosyphon operation with no EHD forces, $q = 8$ kW/m^2

Figure 5.4 - Thermosyphon operation with no EHD forces, $q = 15$ kW/m^2

Figure 5.5 shows the measured heat transfer coefficient in the evaporator section for both the 50 % fill volume ((a) & (c)) and 100 % fill volume ((b) & (d)). It is evident that the frequency of the high voltage sine wave was not a significant influence on the heat transfer coefficient over the investigated range (20 Hz $< f <$ 100 Hz).

Figure 5.5 (a) and (b) show the heat transfer coefficient changes with input electric field strength for an imposed heat flux in the evaporator section of $q = 8$ kW/m^2. It is clear that at a lower level of heat flux there is an increase in the heat transfer coefficient most notably at voltages above the threshold of 4 kV. The highest heat transfer coefficient enhancement of 40 % was seen for the 50 % fluid loading at $V = 8$ kV. For $V \geq 4$ kV, the EHD forces act to redistribute the phases within the evaporator section. Phase mixing is enhanced as the high voltage through the electrode attracts the liquid phase and repels the vapour phase.

There is a large volume of liquid in the evaporator section which appears to pulse when acted upon by the applied EHD voltage. This behaviour is similar to that described in previous EHD studies for flow boiling at low qualities [65]. For an applied A.C. waveform, the redistribution of the phases occurs at a frequency double that of the applied voltage signal. This is due EHD forces responding to the switching charge of the A.C. signal, and the polarisation forces which are proportional to the square of the electric field strength.

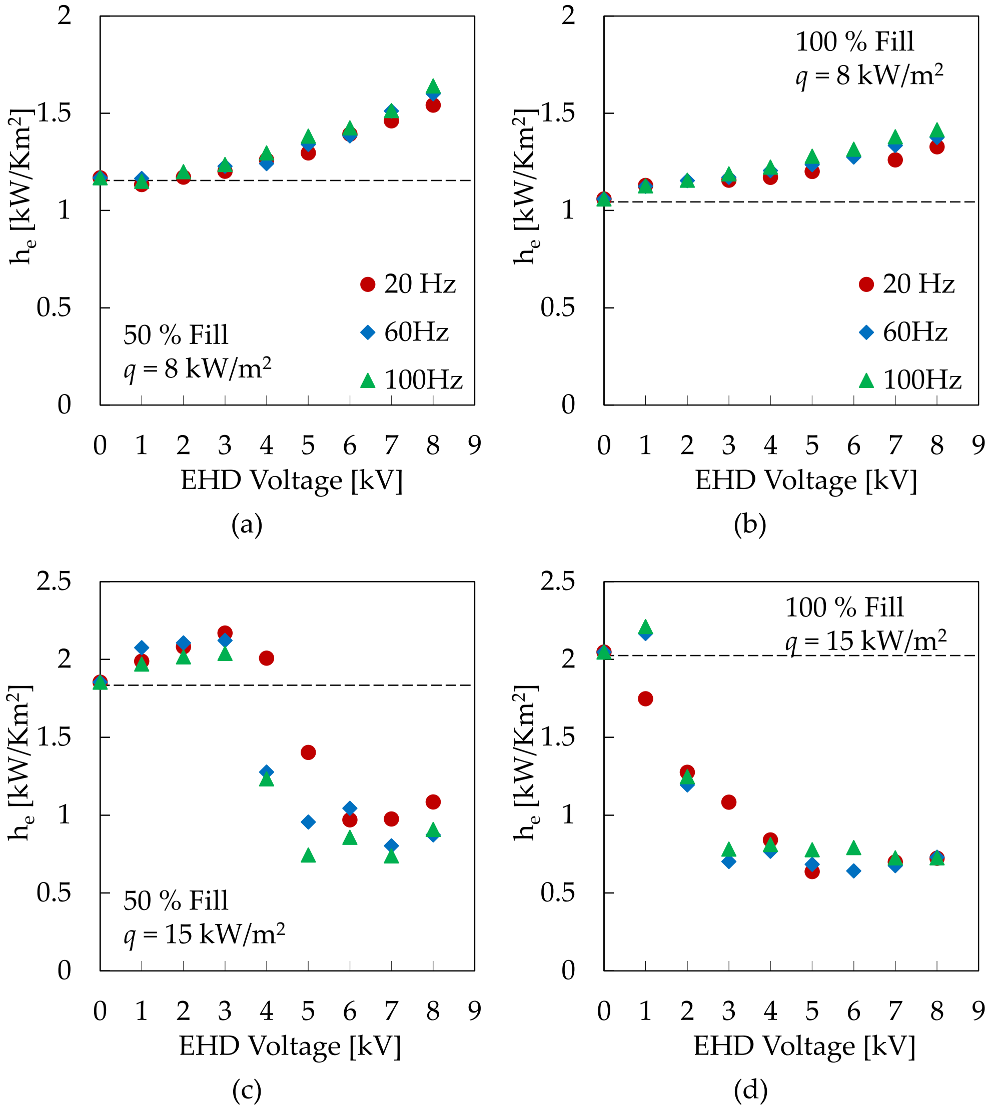

(a) (b) (c) (d)

Figure 5.5 - Heat transfer coefficient trends for: (a) 50 % fill, low heat flux; (b) 100 % fill, low heat flux; (c) 50 % fill, high heat flux; (d) 100 % fill, high heat flux

Conversely, for a higher imposed heat flux of $q = 15$ kW/m², shown in the bottom half of Figure 5.5 (b) and (c), the heat transfer coefficient rapidly deteriorated when the applied high voltage was above the EHD threshold of 4 kV. Once the applied voltage reaches the threshold for dominant EHD forces, liquid extraction rapidly pulls this film from the evaporator wall. There is no longer any liquid reaching the evaporator wall and the temperatures in this region rise sharply as dryout occurs. As a result, a reduction of up to 70 % is observed in the evaporator heat transfer coefficient.

This behaviour is further highlighted by the time trace results of the evaporator wall superheat, as shown in Figure 5.6. This figure illustrates evaporator superheat [$\Delta T_{SH} = T_{ew} - T_{sat}$] over time with increasing applied high voltage to the electrode. The first seconds ($t < 10$ s) of these plots are without any applied voltage and the consequent changes in superheat are due to the influence of EHD. It can be seen from Figure 5.6 that there is a stark difference in behaviour from low to high input heat flux in relation to the measured evaporator temperatures. Again, it is clear that EHD forces do not influence the heat transfer in a significant way below a threshold of $V \sim 4$ kV.

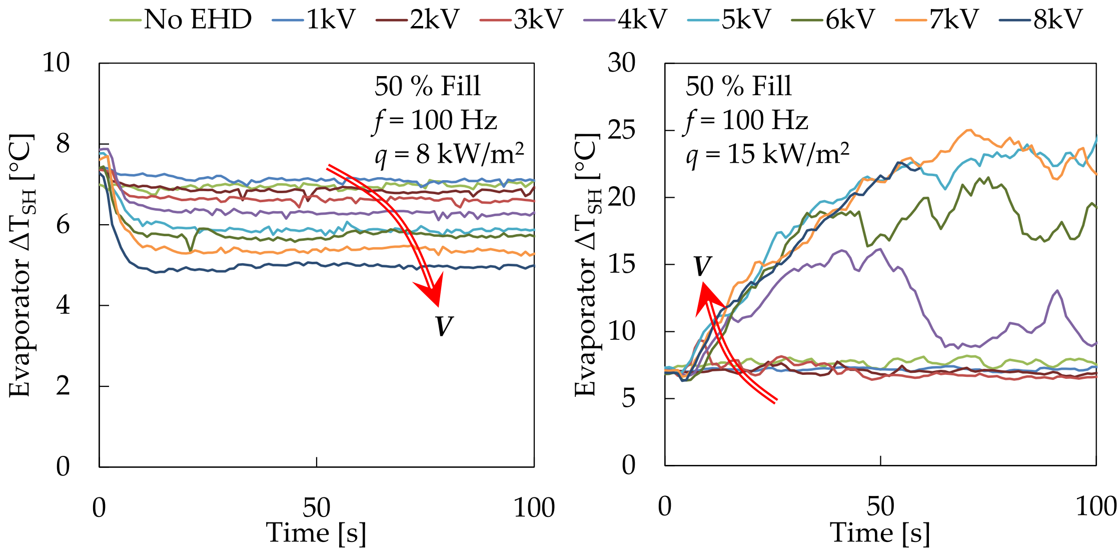

Figure 5.6 - Evaporator superheat temperature time traces for low (left) and high (right) heat flux at $f = 100$ Hz

The changes in heat transfer coefficient are a result of the changes in the liquid-vapour interaction in the presence of an electric field. The change in flow behaviour with applied EHD forces is evident from observing the high-speed images. Figure 5.7 shows an example of the changing flow regime from 0 kV to 8 kV for the lower heat flux, $q = 8$ kW/m^2, 50 % fill volume. At an applied EHD voltage of 8 kV (bottom image) the liquid extraction is evident in the evaporator section by cones of liquid clinging to the electrode as it is attracted to the EHD force. Vapour bubbles are also seen to move toward the evaporator wall as they are repelled by the high voltage through the electrode. This phase redistribution clearly enhances the mixing within the evaporator as liquid is seen to cover a larger surface area of this region, thus enhancing the heat transfer coefficient.

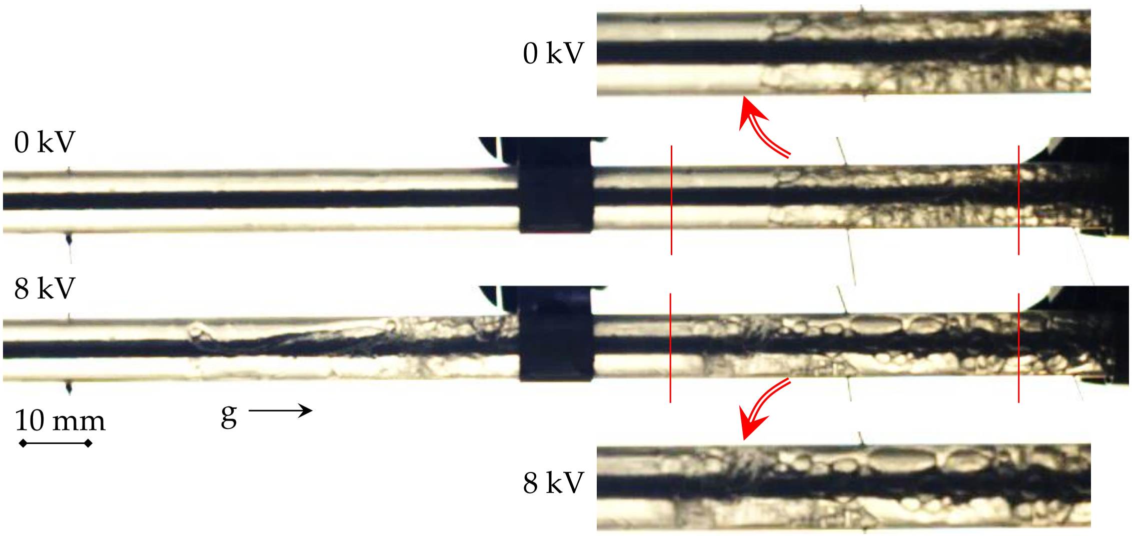

Figure 5.7 - EHD influence on flow. Top: $V = 0$ kV, $q = 8$ kW/m^2; Bottom: $V = 8$ kV, $q = 8$ kW/m^2

Figure 5.8 compares the thermosyphon performance at the higher heat flux, $q = 15$ kW/m^2. At this higher heat flux, nucleate boiling in the film is evident in the upper evaporator section in the case where no high voltage is applied (top image).

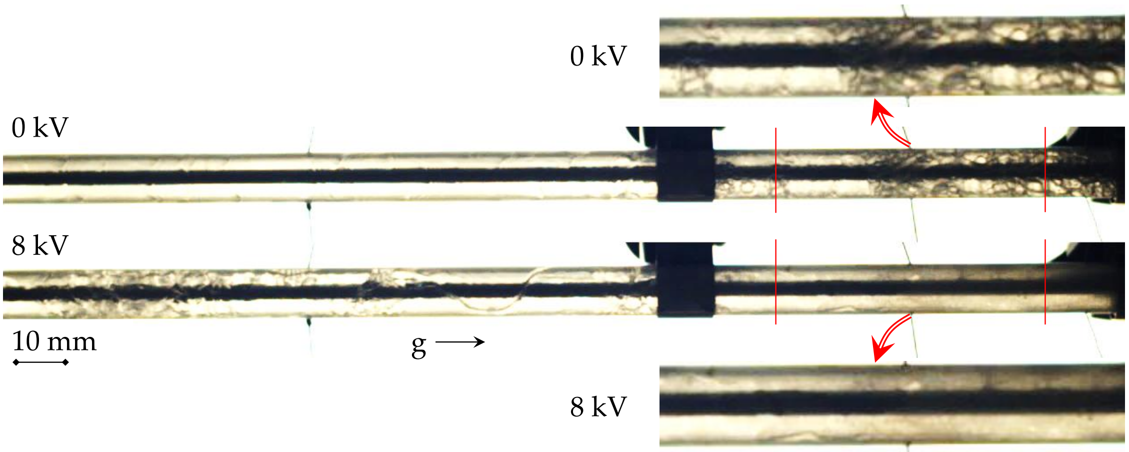

Figure 5.8 - EHD influence on flow. Top: $V = 0$ kV, $q = 15$ kW/m^2; Bottom: $V = 8$ kV, $q = 15$ kW/m^2

In Figure 5.8 (bottom image), at an applied high voltage of 8 kV, the lower evaporator section has completely dried out, giving rise to the large superheat temperatures shown in Figure 5.6. Liquid hold-up is evident in the adiabatic section as the vapour generation rates are higher for this increased heat flux. Liquid extraction from the wall is evident in the adiabatic section in Figure 5.8. Spikes are seen to bridge the gap between electrode and wall in the upper adiabatic section.

This analysis indicates that substantial flow and heat transfer improvements (up to 40 %) can be achieved in thermosyphon performance with EHD. However, care must be taken to avoid the deterioration of the heat transfer coefficient and excursion of the wall temperature evident in the case of the higher heat flux, $q = 15$ kW/m^2. The influence of the applied EHD forces on the flow is significant, though the effects are reversible once the high voltage is removed.

Figure 5.9 shows a time trace of the lower evaporator temperature (T8), pressure and condenser temperature for $q = 15$ kW/m^2. This graph highlights the reaction of the system to EHD forces. During this test, the high voltage supply was switched from $V = 0$ kV to 7.5 kV at a frequency $f = 20$ Hz. The test begins with no applied voltage, $V = 0$ kV, and the dashed green line indicates the point at which the high voltage is switched on, $V = 7.5$ kV. At the red dashed line, the high voltage is removed.

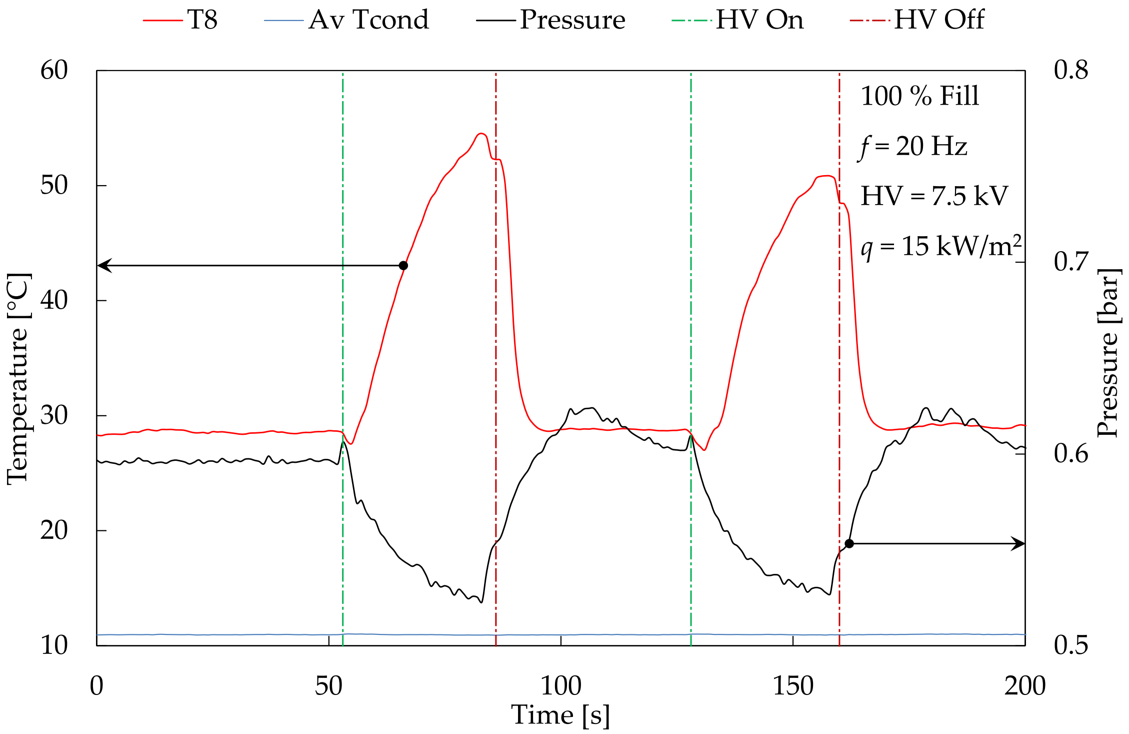

Figure 5.9 - Time trace for temperature and pressure with application and removal of EHD voltage ($q = 15$ kW/m^2, $V = 7.5$ kV, 100 % fill volume)

Once the EHD forces act on the thermosyphon, the temperature in the evaporator is increased as the last of the liquid film in this section is evaporated. With the removal of EHD forces, the system rapidly restores to the original state as the liquid quickly refills the evaporator section and cools the wall. Very little change is evident in the condenser section with the application of EHD on the system.

Figure 5.9 confirms that the system will restore even if the heat transfer coefficient is deteriorated. The same system restoration is also true for heat transfer enhancement at the lower heat flux tested. This result is important as it indicates that it would be possible to have a high level of control over the heat transfer (increase/decrease) within a thermosyphon using EHD forces.

It should also be noted that for the same equipment arrangement, McGranaghan and Robinson [72], calculated the electrical penalty associated with the generation of the electric field for EHD. This was found to be a maximum of 4.5 W for a high voltage of $V = 10$ kV.

Further testing is necessary in order to develop this technology into a reliable flow and heat transfer control system. The focus of further study should be to widen the experimental parameter set and pinpoint the combination of heat flux and applied voltage and frequencies that result in maximum heat transfer enhancement. Also of practical importance is the identification of the point at which the heat transfer coefficient is deteriorated with applied EHD forces.

5.5. Conclusion

The results of this chapter determined that the performance of a thermosyphon in the presence of an electric field is sensitive to the electric field strength and the heat load applied to the evaporator. As evidenced by the flow regime maps in Section 4.4, the rate of heat transfer to the evaporator will determine the boiling regime. It was found that during the nucleate pool boiling regime, EHD forces act to enhance the heat transfer coefficient. However, during annular flow regimes at high heat fluxes, EHD deteriorated the heat transfer performance of the thermosyphon. The main conclusions from this chapter are listed as follows:

- Different flow regimes and associated heat transfer performance was observed for the thermosyphon with and without the influence of electric fields.
- Increasing the electric field strength increased the effects of the electric field on the thermosyphon heat transfer and flow regimes.
- The effects of EHD on the flow regimes, and consequently the heat transfer, became apparent as the electrogravitational force approaches unity. For the current investigation, this threshold corresponds to $V \sim 4$ kV.
- Flow regime augmentation in the thermosyphon with applied electric field is due to the phase redistribution as liquid is attracted to the electrode, while vapour is repelled toward the walls.
- Heat transfer enhancement in the evaporator of up to 40 % is observed for lower heat fluxes ($q = 8$ kW/m^2). The enhancement is due to increased mixing of the liquid and vapour phases as a result of the forced motion due to the applied electric field.
- As the heat flux in the evaporator is increased to a level of $q = 15$ kW/m^2, the EHD forces deteriorate the heat transfer by causing dryout of the evaporator wall.

These preliminary results suggest that smart control of thermosyphon performance is possible using electric fields. Development of this technology could lead to advanced thermal management solutions.

6. Conclusion

The objectives of this research stemmed from an investigation of implementing a thermosyphon as a cooling solution for RFPAs in telecommunications hardware. Further to this, the two-phase flow and heat transfer in small diameter thermosyphons was characterised and an understanding of the fundamental forces influencing the performance was gained.

The proposed application for this cooling solution imposed limits on the thermosyphon design in terms of size and weight, but also reliability concerns dictated that natural convection cooling must be employed for the air-side heat sink. Due to the size and orientation of the telecommunications hardware, the proposed thermosyphon design incorporated bend angles and small channel dimension into the geometry to help integrate the cooling solution into the application. It was found that the small dimension of the thermosyphon resulted in some unfavourable oscillatory behaviour due to the restrictions imposed by confinement on the two-phase counter-current flow. The addition of bends in the adiabatic section of the thermosyphon mitigated these flow oscillations and resulted in a steadier operation, while also allowing for more complex geometries to be employed in the context of the cooling application. Ultimately, the thermosyphon was shown to be a feasible technology for telecommunications cooling, however, the issue of unsteady boiling behaviour in small dimensions was highlighted.

In order to further understand the mechanisms behind the observed flow oscillations, a transparent thermosyphon test section was designed and constructed that allowed for complete visualisation of the mechanisms influencing the two-phase behaviour. It was determined that for these small dimensions, Earth-based thermosyphons are dominated by gravitational forces while surface tension and inertial forces are comparatively insignificant. Within the gravity dominated system, the confinement level of the small channel diameter and rate of vapour production determine the two-phase flow regimes within the thermosyphon. The heat transfer performance of the thermosyphon was strongly linked to the observed flow regimes, whereby the particular flow regimes defined the effective heat transfer for a given experimental condition. This led to the recognition of the most favourable operating conditions in terms of both stable thermosyphon performance and high rates of heat transfer.

Based on the level of confinement and rate of vapour production the observed flow regimes were categorised in a flow regime map. It is proposed that this map could aid in the design and manufacture of small dimension thermosyphons for a particular two-phase flow behaviour. Importantly, this map points to unfavourable transient operating conditions encountered at high levels of confinement and high vapour production rates. For the current study, the bubbly and churn flow regimes resulted in the best performance, representing relatively high heat transfer coefficients and steady two-phase flow behaviour.

Additionally, the smart control of the non-oscillatory flow regimes was investigated by imposing electric fields on the two-phase flow within the thermosyphon. Electrohydrodynamic (EHD) forces acted to attract the liquid phase and repel the vapour phase within the evaporator section, therefore disturbing the two-phase flow by redistributing the phases. Differing and encouraging behaviour was observed across the range of parameters tested, depending on the initial flow regime observed within the evaporator section. For bubbly-type flow regimes, at low levels of heat flux, the heat transfer was enhanced by the application of an electric field. This is due to enhanced mixing of the liquid and vapour phases in the region of the heated surface. For annular-type flow regimes at higher heat fluxes, the heat transfer was deteriorated with imposed EHD voltage due to liquid extraction from the heated walls leading to dryout. The response of the thermosyphon behaviour to the applied electric field occurred quickly. It was also noted that that the system returned rapidly to the initial free-field operation with removal of the electric field. It is hoped that these results will contribute towards areas of further study, ultimately allowing for the development of novel and smart EHD-controlled thermosyphons for advanced thermal management and temperature control.

Considering the above, the most significant contributions to knowledge of this research are as follows:

- A prototype thermosyphon was developed with a natural convection heat sink for RRH cooling. The thermosyphon showed substantially lower thermal resistance compared to the existing air cooled heat sink and high failure power, presenting it as a viable cooling solution for the telecommunications hardware requirements.
- A novel design with bends in the adiabatic section was investigated, which has not previously been studied in simple reflux thermosyphons. The results were promising for future thermosyphon designs, with performance enhancement evident over a range of bend angles tested.
- The current work considered two-phase flow patterns and rates of heat transfer concurrently. While this approach is commonplace in convective two-phase flow analysis, to the best of the author's knowledge there is no existing application to reflux thermosyphons.
- New flow regime maps were developed which define the thermosyphon behaviour in terms of the degree of confinement and rate of vapour production. The results highlight the importance of fluid selection and geometry in the design of thermosyphons of this scale.
- Using synchronised flow visualisation and thermal measurements, the relationship between the observed flow regimes and associated rates of heat transfer in two-phase closed thermosyphons was determined, which, to the author's knowledge, has not been studied previously.
- The investigation of EHD on the two-phase thermosyphon behaviour confirms that the flow regimes and associated heat transfer of the thermosyphon can be controlled using electric fields.

7. Further Work

There are a number of future opportunities stemming from the investigations of this work. The experimental equipment can be further modified and parameter ranges expanded. The main suggested developments for this project are listed as follows:

- To fully understand the flow regime behaviour of thermosyphons operating with bend angles and flow restrictions encountered in Chapter 3, a wider range of angles and evaporator lengths could be investigated. In this way, the threshold for heat transfer enhancement could be recognised and applied to future thermosyphon design.
- In relation to the stainless steel thermosyphon detailed in Chapter 3, more complex structures could be employed to improve the two-phase flow behaviour. In particular, coils or vanes in the adiabatic section to increase the amount of liquid return to the evaporator may prolong the device operation at higher powers.
- Further study of the transparent test section should broaden the parameter range investigated. Variation of system pressures, input heat fluxes and additional fluid fill volumes could provide further insight into the two-phase flow regimes in small diameter thermosyphons.
- Further investigation of the flow regimes in two-phase reflux thermosyphons is necessary to fully map the flow regimes, and pinpoint the transitions between the observed flow patterns. This study would involve modification of the existing transparent test section to study a range of tube diameters, and evaporator and condenser lengths, with various working fluids.

- The effects of inclination on the transparent thermosyphon test section could pinpoint the mechanisms leading to heat transfer enhancement or deterioration as the flow regimes change with tilt angle.
- The results of the EHD flow augmentation study provided proof-of-concept for control and thermal management of the thermosyphon output. Further testing should aim to refine the results of this study and further understand the mechanisms involved.
- For the case of the EHD in thermosyphons, the range of parameters can be expanded in a number of ways. This would involve a wider range of frequencies, waveforms, input heat flux levels and electrode size and orientation for both AC and DC voltage. The EHD voltage could also be isolated to certain sections of the thermosyphon, for an analysis of the effects of EHD on specific thermosyphon regions.

The opportunities for further work in this area of research are substantial and not limited to the above list. Further applications of the test apparatus may also become apparent in the future with further advances of the state of the art.

Bibliography

[1] A. Faghri, "Review and Advances in Heat Pipe Science and Technology," *J. Heat Transfer*, vol. 134, no. 12, p. 123001, 2012.

[2] S. H. Noie, "Heat transfer characteristics of a two-phase closed thermosyphon," *Appl. Therm. Eng.*, vol. 25, no. 4, pp. 495–506, Mar. 2005.

[3] D. A. Reay and P. A. Kew, *Heat pipes: Theory, design and applications*. 2006.

[4] E.S.D.U, "Heat Pipes 81038 - Performance of two phase closed thermosyphons," Engineering Sciences Data Unit, 2005.

[5] A. Faghri, *Heat pipe science and technology*. London: Taylor & Francis, 1995.

[6] I. L. Pioro, W. M. Rohsenow, and S. S. Doerffer, "Nucleate pool-boiling heat transfer. I: review of parametric effects of boiling surface," *Int. J. Heat Mass Transf.*, vol. 47, no. 23, pp. 5033–5044, 2004.

[7] F. Agostini and B. Agostini, "Flexible two-phase thermosyphon for power electronic cooling," in *Telecommunications Energy Conference (INTELEC), 2011 IEEE 33rd International*, 2011, pp. 1–6.

[8] B. Palm and R. Khodabandeh, "Choosing Working Fluid for Two-Phase Thermosyphon Systems for Cooling of Electronics," *J. Electron. Packag.*, vol. 125, no. 2, pp. 276–281, 2003.

[9] A. Pal, Y. K. Joshi, M. H. Beitelmal, C. D. Patel, and T. M. Wenger, "Design and Performance Evaluation of a Compact Thermosyphon," *IEEE Trans. Components Packag. Technol.*, vol. 25, no. 4, pp. 601–607, 2002.

[10] M. S. El-Genk and H. H. Saber, "Heat transfer correlations for small, uniformly heated liquid pools," *Int. J. Heat Mass Transf.*, vol. 41, no. 2, pp. 261–274, Jan. 1998.

[11] C. L. Ong and J. R. Thome, "Macro-to-microchannel transition in two-phase flow: Part 1 – Two-phase flow patterns and film thickness measurements," *Exp. Therm. Fluid Sci.*, vol. 35, no. 1, pp. 37–47, Jan. 2011.

[12] A. Franco and S. Filippeschi, "Closed loop two-phase thermosyphon of small dimensions: A review of the experimental results," *Microgravity Sci. Technol.*, vol. 24, no. 3, pp. 165–179, 2012.

[13] M. Shiraishi, P. Terdtoon, and M. Murakami, "Visual study on flow behavior in an inclined two-phase closed thermosyphon," *Heat Transf. Eng.*, vol. 16, no. 1, pp. 53–59, 1995.

[14] P. Terdtoon, N. Waowaew, and P. Tantakom, "Internal Flow Patterns of an Inclined, Closed Two-Phase Thermosyphon at Critical State: Case Study I, Effect of Aspect Ratio," *Exp. heat Transf.*, vol. 12, no. 4, pp. 347–358, 1999.

[15] P. Terdtoon, N. Waowaew, and P. Tantakom, “Internal Flow Patterns of an Inclined Closed Two-Phase Thermosyphon at Critical State: Case Study II, Effect of Bond Number,” *Exp. heat Transf.*, vol. 12, no. 4, pp. 359–373, 1999.

[16] R. T. Dobson, “Simulation of the two-phase flow in a thermosyphon using an inclined transparent tube with the lower-end closed and the upper-end open,” *Rev. Générale Therm.*, vol. 37, no. 11, pp. 968–972, 1998.

[17] H. Farsi, J. L. Joly, M. Miscevic, V. Platel, and N. Mazet, “An experimental and theoretical investigation of the transient behavior of a two-phase closed thermosyphon,” *Appl. Therm. Eng.*, vol. 23, no. 15, pp. 1895–1912, Oct. 2003.

[18] C. Casarosa, E. Latrofa, and A. Shelginski, “The geyser effect in a two-phase thermosyphon,” *Int. J. Heat Mass Transf.*, vol. 26, no. 6, pp. 933–941, 1983.

[19] S. G. Kandlikar, “Heat Transfer Mechanisms During Flow Boiling in Microchannels,” *J. Heat Transfer*, vol. 126, no. 1, p. 8, 2004.

[20] J. G. Collier and J. R. Thome, *Convective boiling and condensation*. Oxford University Press, 1994.

[21] S. J. Chen, J. G. Reed, and C. L. Tien, “Reflux condensation in a two-phase closed thermosyphon,” *Int. J. Heat Mass Transf.*, vol. 27, no. 9, pp. 1587–1594, Sep. 1984.

[22] U. Gross, “Reflux Condensation Heat Transfer Inside a Closed Thermosyphon,” *Int. J. Heat Mass Transf.*, vol. 35, no. 2, pp. 279–294, 1992.

[23] H. Hashimoto and F. Kaminaga, “Heat transfer characteristics in a condenser of closed two-phase thermosyphon: Effect of entrainment on heat transfer deterioration,” *Heat Transf. Res.*, vol. 31, no. 3, pp. 212–225, May 2002.

[24] H. Jouhara and A. J. Robinson, “Experimental investigation of small diameter two-phase closed thermosyphons charged with water, FC-84, FC-77 and FC-3283,” *Appl. Therm. Eng.*, vol. 30, no. 2–3, pp. 201–211, 2010.

[25] S. Baba, N. Ohtani, O. Kawanami, K. Inoue, and H. Ohta, “Experiments on dominant force regimes in flow boiling using mini-tubes,” *Front. Heat Mass Transf.*, vol. 3, no. 4, Jan. 2013.

[26] W. C. Reynolds and H. M. Satterlee, “Liquid propellant behaviour at low and zero g,” *NASA Spec. Publ.*, pp. 387–440, 1966.

[27] P. Di Marco, “Influence of Force Fields and Flow Patterns on Boiling Heat Transfer Performance: A Review,” *J. Heat Transfer*, vol. 134, no. 3, pp. 030801 – 1–10, 2012.

[28] W. M. Rohsenow, “A method of correlating heat transfer data for surface boiling of liquids,” *J. Heat Transfer*, vol. 74, pp. 969–976, 1951.

[29] Y. J. Park, H. K. Kang, and C. J. Kim, “Heat transfer characteristics of a two-phase closed thermosyphon to the fill charge ratio,” *Int. J. Heat Mass Transf.*, vol. 45, no. 23, pp. 4655–4661, Nov. 2002.

[30] I. L. Pioro, W. M. Rohsenow, and S. S. Doerffer, “Nucleate pool-boiling heat transfer. II: assessment of prediction methods,” *Int. J. Heat Mass Transf.*, vol. 47, no. 23, pp. 5045–5057, Nov. 2004.

[31] H. Imura, H. Kusuda, J. I. Ogata, T. Miyazaki, and N. Sakamoto, "Heat transfer in two-phase closed-type thermosyphons," *JSME Trans.*, vol. 45, pp. 712–722, 1979.

[32] M. Shiraishi, K. Kikuchi, and T. Yamanishi, "Investigation of Heat Transfer Characteristics of a Two-Phase Closed Thermosyphon," *J. Heat Recover. Syst.*, vol. 1, no. 4, pp. 287–297, 1981.

[33] F. M. Chowdhury, F. Kaminaga, K. Goto, and K. Matsumura, "Boiling heat transfer in a small diameter tube below atmospheric pressure on a natural circulation condition," *J. Japan Assoc. Heat Pipe*, vol. 16, pp. 14–16, 1997.

[34] G. B. Wallis, *One-dimensional two-phase flow*, vol. 1. McGraw-Hill New York, 1969.

[35] S. S. Kutateladze, "Elements of the hydrodynamics of gas-liquid systems," *Fluid Mech. Res.*, vol. 1, p. 4, 1972.

[36] C. L. Tien and K. S. Chung, "Entrainment Limits in Heat Pipes," *AIAA J.*, vol. 17, no. 6, pp. 643–646, 1979.

[37] A. Faghri, M. M. Chen, and M. Morgan, "Heat transfer characteristics in two-phase closed conventional and concentric annular thermosyphons," *J. Heat Transfer*, vol. 111, no. 3, pp. 611–618, 1989.

[38] M. S. El-Genk and H. H. Saber, "Determination of operation envelopes for closed, two-phase thermosyphons," *Int. J. Heat Mass Transf.*, vol. 42, no. 5, pp. 889–903, 1999.

[39] B. Jiao, L. M. Qiu, Z. H. Gan, and X. B. Zhang, "Determination of the operation range of a vertical two-phase closed thermosyphon," *Heat Mass Transf.*, vol. 48, no. 6, pp. 1043–1055, 2012.

[40] G. Ribatski, "A Critical Overview on the Recent Literature Concerning Flow Boiling and Two-Phase Flows Inside Micro-Scale Channels," *Exp. Heat Transf.*, vol. 26, no. 2–3, pp. 198–246, 2013.

[41] R. Cole, "Bubble frequencies and departure volumes at subatmospheric pressures," *AIChE J.*, vol. 13, no. 4, pp. 779–783, 1967.

[42] I. Khazaee, R. Hosseini, and S. H. Noie, "Experimental investigation of effective parameters and correlation of geyser boiling in a two-phase closed thermosyphon," *Appl. Therm. Eng.*, vol. 30, no. 5, pp. 406–412, 2010.

[43] S. Filippeschi, "Comparison between miniature periodic two-phase thermosyphons and miniature LHP applied to electronic cooling equipment," *Appl. Therm. Eng.*, vol. 31, no. 5, pp. 795–802, Apr. 2011.

[44] H. Jouhara, Z. Ajji, Y. Koudsi, H. Ezzuddin, and N. Mousa, "Experimental investigation of an inclined-condenser wickless heat pipe charged with water and an ethanol–water azeotropic mixture," *Energy*, vol. 61, pp. 139–147, Nov. 2013.

[45] K. Negishi and T. Sawada, "Heat transfer performance of an inclined two-phase closed thermosyphon," *Int. J. Heat Mass Transf.*, vol. 26, no. 8, pp. 1207–1213, 1983.

[46] K. Negishi, "A blowup phenomenon of the working fluid in a two-phase closed thermosyphon," in *Institute of Space and Astronautical Science Proc. of the Symp. on Mech. for Space Flight*, 1984, vol. 1, pp. 69–74.

[47] T. F. Lin, W. T. Lin, Y. L. Tsay, J. C. Wu, and R. J. Shyu, “Experimental investigation of geyser boiling in an annular two-phase closed thermosyphon,” *Int. J. Heat Mass Transf.*, vol. 38, no. 2, pp. 295–307, 1995.

[48] H. Kuncoro, Y. F. Rao, and K. Fukuda, “An experimental study on the mechanism of geysering in a closed two-phase thermosyphon,” *Int. J. Multiph. Flow*, vol. 21, no. 6, pp. 1243–1252, 1995.

[49] S. L. Abreu, J. A. Skiavine, and S. Colle, “Working characteriscs of a compact solar hot water system with heat pipes during startup and geyser boiling periods,” *Proc. ISES Sol. World Congr.*, 2003.

[50] M. R. Sarmasti Emami, S. H. Noie, M. Khoshnoodi, M. T. Hamed Mosavian, and A. Kianifar, “Investigation of Geyser Boiling Phenomenon in a Two-Phase Closed Thermosyphon,” *Heat Transf. Eng.*, vol. 30, no. 5, pp. 408–415, 2009.

[51] H. Nguyen-Chi and M. Groll, “Entrainment or Flooding Limit in a Closed Two-Phase Thermosyphon,” *J. Heat Recover. Syst.*, vol. 1, no. 4, pp. 275–286, 1981.

[52] T. Payakaruk, P. Terdtoon, and S. Ritthidech, “Correlations to predict heat transfer characteristics of an inclined closed two-phase thermosyphon at normal operating conditions,” *Appl. Therm. Eng.*, vol. 20, no. 9, pp. 781–790, 2000.

[53] G. S. H. Lock and J. Fu, “Observations on an evaporative, elbow thermosyphon,” *J. Heat Transfer*, vol. 115, no. 2, pp. 501–503, 1993.

[54] R. S. McKee and F. D. Hobbs, “Development of a flexible thermosyphon for cooling a concentrated heat source,” *9th International Heat Pipe Conference*. Albuquerque, NM (United States), 1995.

[55] B. Jiao, L. M. Qiu, X. B. Zhang, and Y. Zhang, “Investigation on the effect of filling ratio on the steady-state heat transfer performance of a vertical two-phase closed thermosyphon,” *Appl. Therm. Eng.*, vol. 28, no. 11–12, pp. 1417–1426, 2008.

[56] S. J. Kline and F. A. McClintock, “Describing uncertainties in single-sample experiments,” *Mech. Eng.*, vol. 75, no. 1, pp. 3–8, 1953.

[57] G. S. H. Lock, “On the flooding limit in the evaporative, tubular thermosyphon,” *Int. Commun. Heat Mass Transf.*, vol. 20, no. 1, pp. 63–68, Jan. 1993.

[58] V. P. Carey, *Liquid-vapor phase-change phenomena*. 1992.

[59] L. Cheng, G. Ribatski, and J. R. Thome, “Two-Phase Flow Patterns and Flow-Pattern Maps: Fundamentals and Applications,” *Appl. Mech. Rev.*, vol. 61, no. 5, pp. 1–28, 2008.

[60] G. F. Hewitt and D. N. Roberts, “Studies of two-phase flow patterns by simultaneous X-ray and flash photography; Report AERE-M 2159,” 1969.

[61] Y. Taitel, D. Barnea, and A. E. Dukler, “Modeling Flow Pattern Transitions for Steady Upward Gas-Liquid Flow in Vertical Tubes,” *Aiche J.*, vol. 26, no. 3, pp. 345–354, 1980.

[62] N. Kattan, J. R. Thome, and D. Favrat, “Flow Boiling in Horizontal Tubes: Part 1—Development of a Diabatic Two-Phase Flow Pattern Map,” *J. Heat Transfer*, vol. 120, no. 1, p. 140, Feb. 1998.

[63] J. E. Bryan and J. Seyed-Yagoobi, "Electrohydrodynamically Enhanced Convective Boiling: Relationship Between Electrohydrodynamic Pressure and Momentum Flux Rate," *J. Heat Transfer*, vol. 122, no. May, pp. 266–277, 2000.

[64] J. S. Cotton, A. J. Robinson, M. Shoukri, and J. S. Chang, "AC voltage induced electrohydrodynamic two-phase convective boiling heat transfer in horizontal annular channels," *Exp. Therm. Fluid Sci.*, vol. 41, pp. 31–42, Sep. 2012.

[65] G. J. McGranaghan and A. J. Robinson, "The mechanisms of heat transfer during convective boiling under the influence of AC electric fields," *Int. J. Heat Mass Transf.*, vol. 73, pp. 376–388, Jun. 2014.

[66] J. S. Cotton, A. J. Robinson, M. Shoukri, and J. S. Chang, "A two-phase flow pattern map for annular channels under a DC applied voltage and the application to electrohydrodynamic convective boiling analysis," *Int. J. Heat Mass Transf.*, vol. 48, no. 25–26, pp. 5563–5579, Dec. 2005.

[67] Y. C. Kweon and M. H. Kim, "Experimental study on nucleate boiling enhancement and bubble dynamic behavior in saturated pool boiling using a nonuniform DC electric field," *Int. J. Multiph. Flow*, vol. 26, no. 8, pp. 1351–1368, Aug. 2000.

[68] J. E. Bryan and J. Seyed-Yagoobi, "Influence of Flow Regime, Heat Flux, and Mass Flux on Electrohydrodynamically Enhanced Convective Boiling," *J. Heat Transfer*, vol. 123, no. 2, pp. 355–367, 2001.

[69] P. H. G. Allen and T. G. Karayiannis, "Electrohydrodynamic Enhancement of Heat Transfer and Fluid Flow," *J. Heat Recover. Syst. CHP*, vol. 15, no. 5, pp. 389–423, 1995.

[70] S. Laohalertdecha, P. Naphon, and S. Wongwises, "A review of electrohydrodynamic enhancement of heat transfer," *Renew. Sustain. Energy Rev.*, vol. 11, no. 5, pp. 858–876, Jun. 2007.

[71] IEEE-DEIS-EHD Technical Committee, "Recommended international standard for dimensionless parameters used in electrohydrodynamics," *IEEE Trans. Dielectr. Electr. Insul.*, vol. 10, no. 1, pp. 3–6, 2003.

[72] G. McGranaghan and A. J. Robinson, "EHD Augmented Convective Boiling: Flow Regimes and Enhanced Heat Transfer," *Heat Transf. Eng.*, vol. 35, no. 5, pp. 517–527, 2014.

[73] S. Nangle-Smith and J. S. Cotton, "EHD-based load controllers for R134a convective boiling heat exchangers," *Appl. Energy*, vol. 134, pp. 125–132, Dec. 2014.

[74] T. B. Jones, "Electrohydrodynamic heat pipes," *Int. J. Heat Mass Transf.*, vol. 16, no. 5, pp. 1045–1048, May 1973.

[75] R. I. Loehrke and D. R. Sebits, "Flat plate electrohydrodynamic heat pipe experiments (No. N-75-28370; NASA-CR-137707)," Colorado State Univ., Fort Collins (USA). Dept. of Mechanical Engineering, 1975.

[76] R. I. Loehrke and W. J. Day, "Performance characteristics of several EHD heat pipe designs," *J. Electrostat.*, vol. 5, pp. 285–296, Sep. 1978.

[77] K. Kikuchi, T. Taketani, M. Shiraishi, and T. Yamanishi, “Large scale EHD heat pipe experiments,” in *Advances in Heat Pipe Technology*, 1981, vol. 1, pp. 643–650.

[78] A. J. Robinson and R. Kempers, “A heat transfer apparatus.,” European Patent Application. EP2896926A1. 2015.

[79] F. P. Incropera and D. P. Dewitt, *Introduction to Heat Transfer*, 2nd Edition. New York: John Wiley & Sons, 1985.

Appendix A. Biot number analysis

In Chapter 3, the heat flux in the thermosyphon evaporator section was quantified by using the inner surface area of the evaporator. Since the heaters were placed only on one side of the evaporator, a Biot number analysis was carried out to validate the assumption of uniform heat flux distribution across the copper block evaporator. For a Biot number, $Bi \ll 1$, the assumption of a uniform temperature distribution across a solid body is valid [79].

The Biot number, Eqn. (A.1), corresponding to the lowest heat flux case was calculated, which shows the worst-case heat flux distribution in the evaporator. For this power level case, Q = 40 W, the experimental parameters used in the Biot number calculation are shown in Table A.1.

Calculation of the Biot number for these experimental conditions resulted in Bi = 0.03, which validates the assumption of uniform heat flux distribution across the copper block evaporator.

$$Bi = \frac{h_e L}{k} \qquad \textbf{Eqn. (A.1)}$$

Where

$$h_e = \frac{Q}{A_i \Delta T} \qquad \textbf{Eqn. (A.2)}$$

and

$$L = \frac{Copper\ block\ volume}{Copper\ block\ surface\ area} \qquad \textbf{Eqn. (A.3)}$$

	Q [W]	A [m²]	q [W/m²]	ΔT [K]	h_e [W/m²K]	L [m]	k [W/mK]
Copper	40	3.7×10^{-3}	11×10^{3}	2	5.4×10^{3}	2.3×10^{-3}	385

Table A.1 - Experimental parameters used in Biot number analysis

Appendix B. Heat loss analysis

For the stainless steel thermosyphon investigated in Chapter 3, the heat losses from the evaporator section were evaluated using the thermal resistance network shown in Figure B.1.

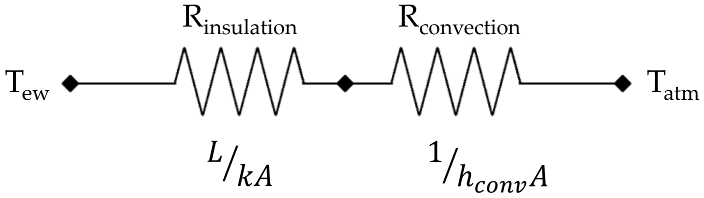

Figure B.1 - Thermal resistance network, evaporator to atmosphere

The total thermal resistance, R_{tot}, was calculated using Eqn. (B.1), which corresponds to the sum of thermal resistance across the high temperature insulation, $R_{insulation}$, and convective resistance to the atmosphere, $R_{convection}$. The highest power level tested, $Q = 300$ W, represents the worst case scenario for ambient heat losses. The experimental parameters used for this condition are detailed below in Table B.1.

$$R_{tot} = \frac{L}{kA} + \frac{1}{h_{conv}A}$$ **Eqn. (B.1)**

The power losses, Q_{losses}, associated with this case are given by Eqn. (B.2), and calculated as $Q_{losses} = 3.2$ W. This represents a loss of 1 % of the total power input and heat loss from the evaporator is therefore assumed negligible.

$$Q_{losses} = \frac{T_{ew} - T_{atm}}{R_{tot}}$$ **Eqn. (B.2)**

Q [W]	T_{ew} [°C]	T_{atm} [°C]	h_{conv} [W/m²K]	k [W/mK]	L [m]	A [m²]
300	140	20	5	0.05	0.015	13.6×10^{-3}

Table B.1 - Experimental parameters for thermal resistance calculation

Appendix C. Influence of electrode on confinement

The HFE-7000 filled thermosyphon was tested over a heat flux range of $7.8 < q < 21.5$ kW/m^2 for the case where there was no electrode, as described in Chapter 4. These tests were performed in order to gain an understanding of the baseline two-phase flow dynamics to which other scenarios can be compared. In this section, these tests will be compared to tests performed with the electrode inserted in the thermosyphon though without the application of the electric field.

Figure C.1 compares the heat transfer coefficient, with and without the electrode for both the 50 % and 100 % fill volume case. Using this comparison, the presence of the electrode has a fairly minor influence on the heat transfer when there is no voltage applied.

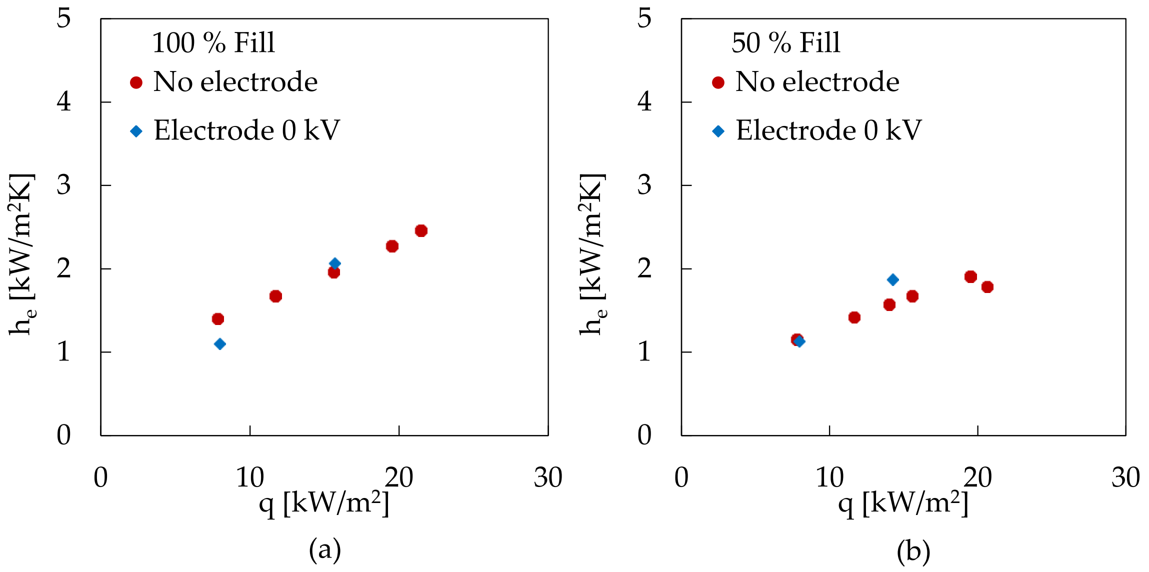

Figure C.1 - Evaporator heat transfer coefficients for low and high heat flux, 100 % and 50 % loading both with and without electrode

Figure C.2 shows an example of the boiling in the evaporator for both the 100 % and 50 % fluid loading for both the high and low heat flux cases. Also presented are images at the same operating conditions with the electrode inserted, but without the application of an electric field, $V = 0$ kV. Again, the electrode does not present a major disturbance to the boiling dynamics within the thermosyphon. This is likely due to the low Confinement number associated with HFE-7000.

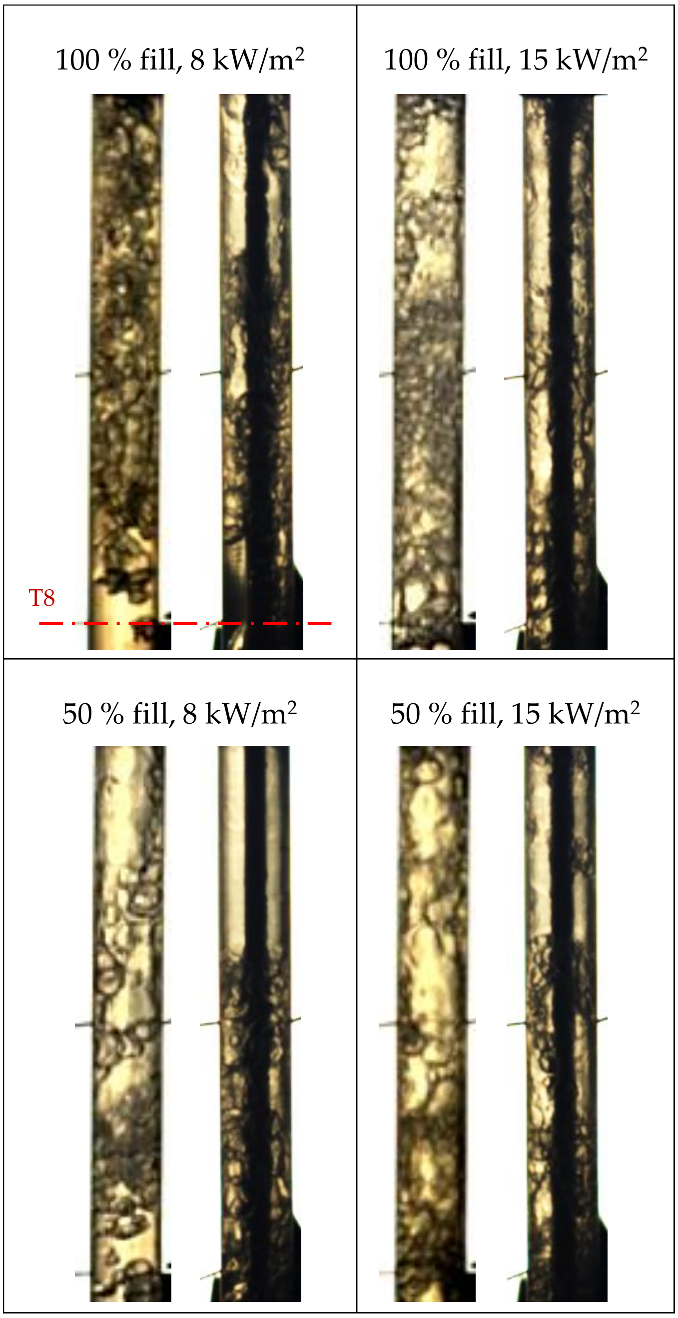

Figure C.2 - Representative images of the evaporator section for low and high heat flux, 50 % and 100 % loading both with and without electrode